MICROCOPY RESOLUTION TEST CHART
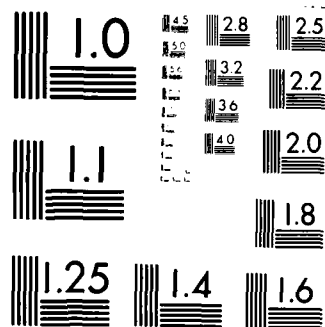
NATIONAL BUREAU OF STANDARDS 1963 A

AD-A155 986

# INTERACTION OF FINITE-AMPLITUDE
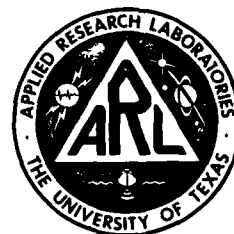
# SOUND WITH AIR-FILLED POROUS MATERIALS

by

DAVID A. NELSON

DEPARTMENT OF MECHANICAL ENGINEERING

THE UNIVERSITY OF TEXAS AT AUSTIN
AUSTIN, TEXAS 78712

APPLIED RESEARCH LABORATORIES

THE UNIVERSITY OF TEXAS AT AUSTIN
AUSTIN, TEXAS 78713-8029

DTIC FILE COPY

MARCH 1985

NATIONAL AERONAUTICS AND SPACE ADMINISTRATION
OFFICE OF NAVAL RESEARCH

DTIC
ELECTE
JUL 0  1985
S        E

85 06 18 106

| 1. Report No. | 2. Government Accession No. $A156\ 986$ | 3. Recipient's Catalog No. CR 174885 |
|---|---|---|

| 4. Title and Subtitle Interaction of Finite-Amplitude Sound with Air-Filled Porous Materials | 5. Report Date March 1985 |
|---|---|
| | 6. Performing Organization Code |

| 7. Author(s) D. A. Nelson | 8. Performing Organization Report No ARL-TR-85-15 |
|---|---|
| | 10. Work Unit No. |

| 9. Performing Organization Name and Address Department of Mechanical Engineering The University of Texas at Austin, Austin, TX 78712 and Applied Research Laboratories, The University of Texas at Austin Austin, TX 78713-8029 | 11. Contract or Grant No. NSG 3198 |
|---|---|
| | 13. Type of Report and Period Covered Final Report 1 Sept. 1981-28 Feb. 1985 |

| 12. Sponsoring Agency Name and Address Fluid Mechanics and Acoustics Division NASA Lewis Research Center 21000 Brookpark Road Cleveland, OH 44135 | 14. Sponsoring Agency Code |
|---|---|

15. Supplementary Notes

16. Abstract

The subject of this investigation is the propagation of high intensity sound waves through an air-filled porous material. The material is assumed (1) to be rigid, incompressible, and homogeneous; and (2) to be adequately described by two properties: resistivity r and porosity $\Omega$. The resistivity was measured as a function of velocity for static flows and found to follow the empirical relation $r = r_1 + r_2 u \, \mathrm{sgn}(u)$. This relation is assumed to apply for acoustic signals as well. Ordinary hydrodynamic nonlinearity (which leads to shock formation) is neglected, because of the very high attenuation in the porous material. The resulting wave equation is still nonlinear, however, because of the $u \, \mathrm{sgn}(u)$ term in the resistivity. The equation is solved in the frequency domain as an infinite set of coupled inhomogeneous Helmholtz equations, one for each harmonic. An approximate first integral formulation of these equations gives relations for progressive waves. The source wave considered is a slightly distorted intense tone, that is, a finite-amplitude fundamental accompanied by weak higher harmonics. An approximate but analytical solution leads to predictions of excess attenuation, saturation, and phase speed reduction for the fundamental component. A more general numerical solution is used to calculate the propagation curves for the higher harmonics. The $u \, \mathrm{sgn}(u)$ nonlinearity produces a cubic distortion pattern; when the input signal is a pure tone, only odd harmonic distortion products are generated. Quantitative experiments were performed on batted Kevlar® 29 having porosities in the range $\Omega = 0.94$ to 0.98. Measurements were taken in the 400 to 6200 Hz frequency range for small-signal waves, 500-1500 Hz for finite-amplitude waves. Source levels for the finite-amplitude waves extended to 160 dB. Qualitative confirmation of predictions has been obtained in all cases, and quantitative confirmation in most cases. The theory is then applied to the problem of propagation and attenuation in lined ducts. A vector version of the wave equation is derived along with the corresponding inhomogeneous Helmholtz equations. These are used as the basis of a perturbation solution for reflection from a porous half-space and propagation in lined ducts. The solution becomes extremely complicated, however, when used for high intensity waves in lined ducts. An ad hoc model is therefore presented for the purpose of illustrating the gross nonlinear effects on absorption.

| 17. Key Words (Suggested by Author(s)) intense sound, bulk porous materials, excess attenuation, saturation, nonlinear acoustics, acoustic impedance, nonlinear propagation, sound attenuation, absorption, lined ducts, reflection, harmonic generation, numerical solution | 18. Distribution Statement unlimited |
|---|---|

| 19. Security Classif. (of this report) unclassified | 20. Security Classif. (of this page) unclassified | 21. No. of Pages 185 | 22. Price* |
|---|---|---|---|

FOREWORD

This report is based on David A. Nelson's master's thesis, "Propagation of Finite-Amplitude Sound in Air-Filled Porous Materials." The report is substantively different, however, in that it includes material on lined ducts (Chapter 6). Because of the additional content, the title of the report is different from that of the thesis.

Mr. Nelson was enrolled in the Department of Mechanical Engineering from September 1981 until December 1984 at which time he received his M.S. degree. Dr. N. D. Perreira served as co-supervisor of the research until he left the University in July 1984. Dr. Ilene Busch-Vishniac served as second reader of the thesis.

The research was carried out at Applied Research Laboratories. Assisting in the experimental phase of the work were James S. McLean (Electrical Engineering undergraduate) and Edward A. Tschoepe (Physics undergraduate). Mr. Nelson also wishes to express his appreciation to Dr. Herbert L. Kuntz II, from whose earlier research the present work follows.

Primary support for the work came from NASA Lewis Research Center under Grant NSG 3198. Additional support came from the Office of Naval Resarch (ONR) under Contracts N00014-75-C-0867 and N00014-84-K-0574. Technical monitors were E. J. Rice for NASA and L. E. Hargrove for ONR.

David T. Blackstock
Supervisor

# TABLE OF CONTENTS

PREVIOUS PAGE
IS BLANK

# LIST OF FIGURES

ix

# LIST OF IMPORTANT SYMBOLS

| | |
|---|---|
| A | cross-sectional area |
| $A_n$ | dimensionless magnitude of nth harmonic component of signal |
| $a_{mn}$, $b_{mn}$, $c_{mn}$, $d_{mn}$ | modal wave numbers of waveguide |
| $c_i = c_o/\sqrt{\gamma}$ | isothermal sound speed |
| $c_n$ | phase speed of nth harmonic component of signal |
| $c_o = \sqrt{\gamma R T_o}$ | adiabatic sound speed |
| $C_{pn}$, $C_{vn}$ | dimensionless phase speed of pressure, particle velocity signal |
| f | frequency |
| $f_o$ | characteristic frequency, such as that of signal fundamental |
| $f_{th}$ | criterion frequency for thermal effects |
| f(u) | generalized amplitude dependence function for static flow resistivity |
| F, $\langle F \rangle$ | thermal boundary layer function, indicator of mean thermodynamic state within pores |
| $F_r$ | static flow rate |
| g | empirical fit constant for resistivity data |
| $I_o$, $K_o$ | modified Bessel functions of the first and second kinds, of order zero |
| j | $\sqrt{-1}$ |
| $K = 4 R_2/3\pi \sqrt{1 + R_1^2}$ | coefficient of resistive nonlinearity, sgn(u) resistivity model |
| $K_3 = 3 R_3/8 \sqrt{1 + R_1^2}$ | coefficient of resistive nonlinearity, quadratic resistivity model |
| k | acoustic wave number |
| L, L(u) | sample length (as a function of flow velocity) |

| | |
|---|---|
| $L_A, L_M$ | thickness of air and material in guide, respectively |
| $m$ | mass of porous sample |
| $n$ | harmonic number |
| $\hat{p}, p_o, \underline{p}$ | pressure (acoustic, ambient, total) |
| $\hat{p} = (\underline{p} - p_o)/c_i^2$ | dimensionless pressure |
| $\hat{P}_n$ | complex dimensionless amplitude of nth harmonic component of pressure signal |
| $\Delta p$ | pressure drop across sample |
| $q_n = q_{nr} - jq_{ni}$ | complex dimensionless wave number |
| $q_{nr}$ | dimensionless small-signal propagation wave number |
| $q_{ni}$ | dimensionless small-signal attenuation constant |
| $q_{n\chi}, q_{n\xi}$ | directional wave numbers |
| $Q_n = q_{ni}/q_{nr}$ | diffusion index |
| $r = \Delta p/L\, F_r$ | resistivity |
| $r_1, r_2, r_3$ | resistivity coefficients for empirical fitted curves |
| $R_1 = r_1/\Omega\,\rho_o\omega_o$ | dimensionless "linear" resistivity |
| $R_2 = r_2 c_i/\Omega\,\rho_o\omega_o$ | dimensionless "nonlinear" resistivity, sgn(u) resistivity model |
| $R_3 = r_3 c_i^2/\Omega\,\rho_o\omega_o$ | dimensionless "nonlinear" resistivity, quadratic resistivity model |
| $\langle R \rangle$ | mean resistivity over one cycle of wave |
| $\mathrm{sgn}(\zeta) = \mathrm{abs}(\zeta)/\zeta$ | 1 for $\zeta > 0$, -1 for $\zeta < 0$ |
| SPL | sound pressure level |
| $t$ | time |
| $t_n(\theta_n)$ | pressure transmission coefficient |
| $u$ | 1-D particle velocity |
| $v$ | 1-D dimensionless particle velocity |

| | |
|---|---|
| $\vec{u}, \vec{v}$ | velocity vectors |
| $V_n$ | complex dimensionless amplitude of nth harmonic component of particle velocity signal |
| $w = u\ \text{sgn}(u)$ | 1-D dimensionless particle speed |
| $W_n$ | complex dimensionless amplitude of nth harmonic component of particle speed |
| $x, y, z$ | spatial coordinates |
| $\bar{x}$ | shock formation distance in air |
| $x_a$ | characteristic length for absorption |
| $Z_n$ | dimensionless characteristic acoustic impedance of porous material |
| $\alpha$ | attenuation constant |
| $\beta$ | coefficient of "hydrodynamic" nonlinearity |
| $\gamma$ | ratio of specific heats |
| $\delta, \delta_f$ | boundary layer thickness for air and fiber |
| $\epsilon$ | perturbation scaling factor |
| $\varphi_n$ | angle of incidence |
| $\pi_n$ | complex dimensionless amplitude of nth harmonic component of pressure signal |
| $\zeta$ | thermal distance scale factor |
| $\rho, \rho_o, \underline{\rho}$ | density (acoustic, ambient, total) |
| $\rho_{Kev}$ | density of Kevlar®29, 1450 kg/m$^3$ |
| $\rho_n(\theta_n)$ | pressure reflection coefficient |
| $\tau$ | dimensionless time |
| $\Delta\varphi = \varphi(x) - \varphi(0)$ | relative phase |
| $\varphi_{vn}, \varphi_{pn}, \varphi_{zn}$ | phase of nth harmonic component of particle velocity, pressure, impedance |
| $\varphi$ | potential function |

| | |
|---|---|
| $\chi$ | dimensionless distance |
| $\omega_o = 2\pi f_o$ | charactistic angular frequency |
| $\psi_n$ | angle of transmission |
| $\Omega$ | porosity |
| $<\Omega_a>$ | mean open area fraction of porous materials |
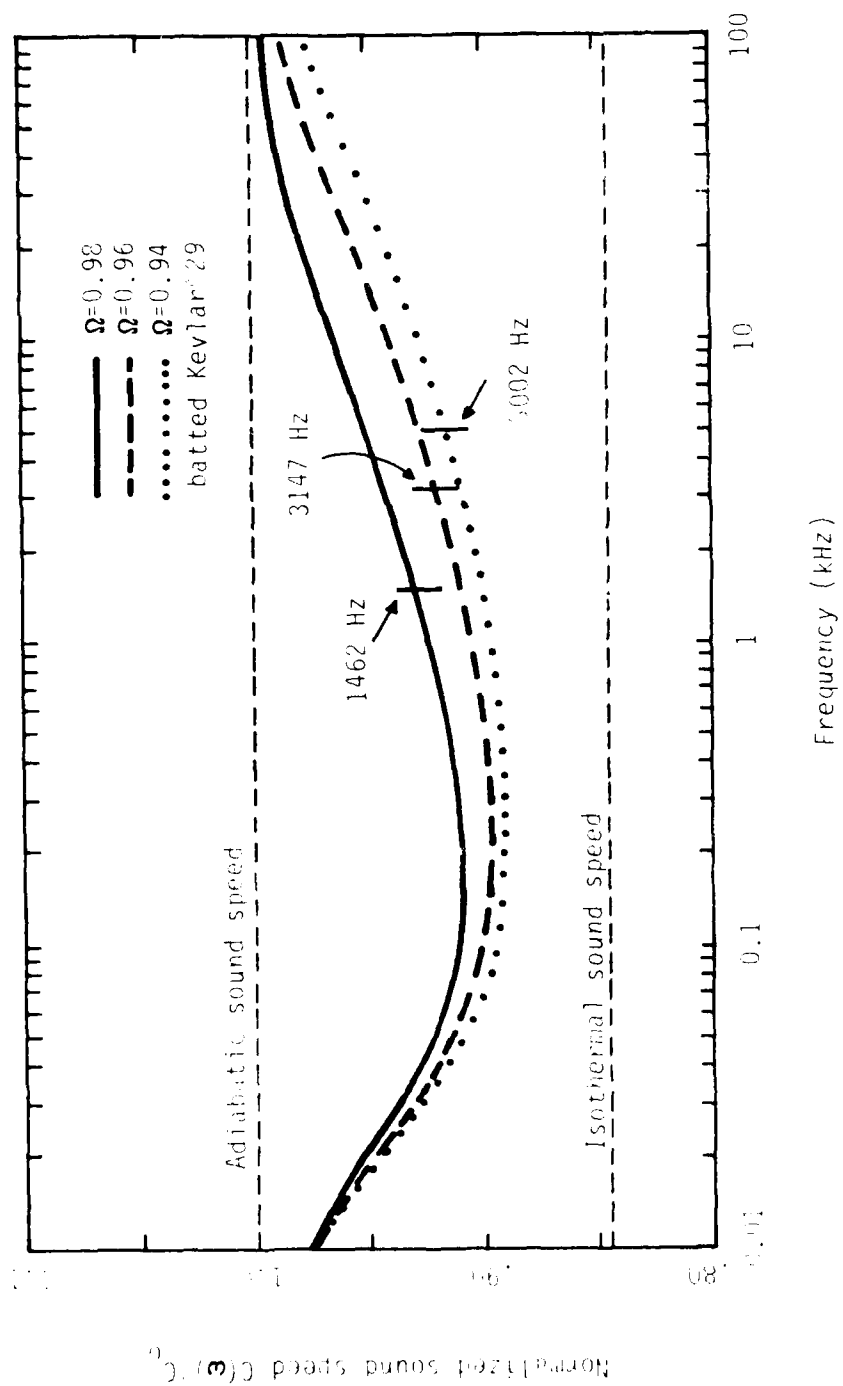
Figure 2-2
Frequency-dependent sound speed

15

AS-85-560

the extensive surface area of the pores, may embrace significant fractions of the fluid. The mean temperature fluctuation in the pores determines the sound speed

$$c = \sqrt{dp/d\underline{\rho}} \quad .$$

Although the phase velocity of a wave in a porous material is actually substantially less than the sound speed, the following discussion is couched in terms of the sound speed because it is the most familiar name for the quantity. Appendix A gives a detailed discussion of the effect on sound speed of heat conduction between the fibers and a laminar flow. For the present it is sufficient to summarize the results of Appendix A.

The sound speed takes a frequency dependent value somewhere between the extremes of the adiabatic value $c_o = \sqrt{\gamma P_o / \rho_o} = \sqrt{\gamma R T_o}$ and the isothermal value $c_i = \sqrt{P_o / \rho_o} = \sqrt{R T_o}$. At high frequency, because the boundary layers around the fibers are relatively thin, most of the air is in an isentropic state. The isentropic value of the sound speed is therefore appropriate. At low frequencies the thermal boundary layers fill the pores almost completely so that the air temperature is constrained to the ambient value $T_o$. In this range the sound speed value is roughly that for an isothermal gas. At sub-audio frequencies, however, the quasi-static temperature variation induced by the acoustic flow overcomes the heat capacity of the frame and drives the temperature of the material as a whole. Since the air and the frame are in thermal equilibrium, the adiabatic sound speed is once more appropriate. Figure 2-2 shows the approximate variation of sound speed with frequency for Kevlar[R]29 of porosity 0.94, 0.96, and 0.98.

The sound speed calculation is based on knowledge of the temperature distribution around an individual fiber. This distribution in turn depends on the assumption that adjacent fibers do not interact thermally; that is, the boundary

where $\omega_1$ is the decoupling frequency and $\rho_{es}$ is the effective structural density defined by Lambert. Interpretation of Eq. (2.11) is straightforward. The resistivity factor represents viscous coupling which drags the frame with the flow while the factor $\rho_{es}$ represents inertia which inhibits frame motion. For frequencies above $\omega_1$ the inertia dominates and the frame tends to remain motionless.

Kevlar®29 was used extensively in the experimental phase of this investigation. In the porosity range 0.94-0.98 the decoupling frequency is between 60 and 85 Hz. The lowest fundamental frequency used in our experiments was considerably higher, namely 500 Hz. Thus, we have assumed the frame to be rigid.

### 4. Constitutive Relation

Heat transfer between the air and the frame causes the thermodynamic state of the entrapped air to depart from being adiabatic. We are primarily interested in the proper relationship of the pressure and density which, as the ideal gas law

$$\underline{p} = \underline{\rho} R \underline{T} \tag{2.12}$$

shows, is determined by the temperature fluctuations in the gas. The acoustic pressure p and acoustic density $\rho$ are related to the total pressure $\underline{p}$ and total density $\underline{\rho}$ as $\underline{p}=p_0+p$ and $\underline{\rho}=\rho_0+\rho$ where $p_0$ and $\rho_0$ are ambient values. The total temperature is similarly expressed as $\underline{T}=T_0+T$ and R is the gas constant. The frame, by virtue of its considerable heat capacity, tends to remain at the ambient temperature $T_0$ while the air temperature fluctuates with the acoustic signal. A thermal boundary layer forms around the frame. In the boundary layer the temperature fluctuations decay to near zero at the frame surfaces. The boundary layer thickness varies as the inverse square root of the frequency and, because of

13

dc flow resistivity data. Although the addition of the sgn(u) term seems redundant for dc flows, its omission led Kuntz[1] to inaccurate theoretical predictions of nonlinear behavior for acoustic signals.

Other expressions exist which fit the data well and satisfy the pressure gradient requirement. One example is

$$r = r_1 + r_3 u^2 \quad . \tag{2.10}$$

Equation (2.10), which we shall refer to as the "quadratic model" rather than the "sgn(u) model," is more attractive for analytical study than Eq. (2.9), but does not bring us any closer to closed form solutions of the wave equation. Furthermore, predicted behavior based on this model does not differ substantially from that predicted for the sgn(u) model (see again Fig. 2-1). Although we have carried out parallel theoretical developments using the quadratic model, the results are somewhat redundant and are not covered here in detail. The quadratic model can be used to obtain a perturbation solution. Analytical expressions for propagation of intense tones and numerical results for propagation of more complex finite-amplitude signals subject to quadratic resistivity are given in Appendix B. The sgn(u) model, however, receives the bulk of the attention in the remainder of this work.

### 3. Frame Rigidity

The material frame is set in motion by the sound field but under certain conditions is nearly stationary and can be considered rigid. Lambert[11] and Zwikker and Kosten[10] determined that forces coupling the frame and gas motion are insignificant if

$$\omega_1 > r_1/\rho_{es} \quad , \tag{2.11}$$
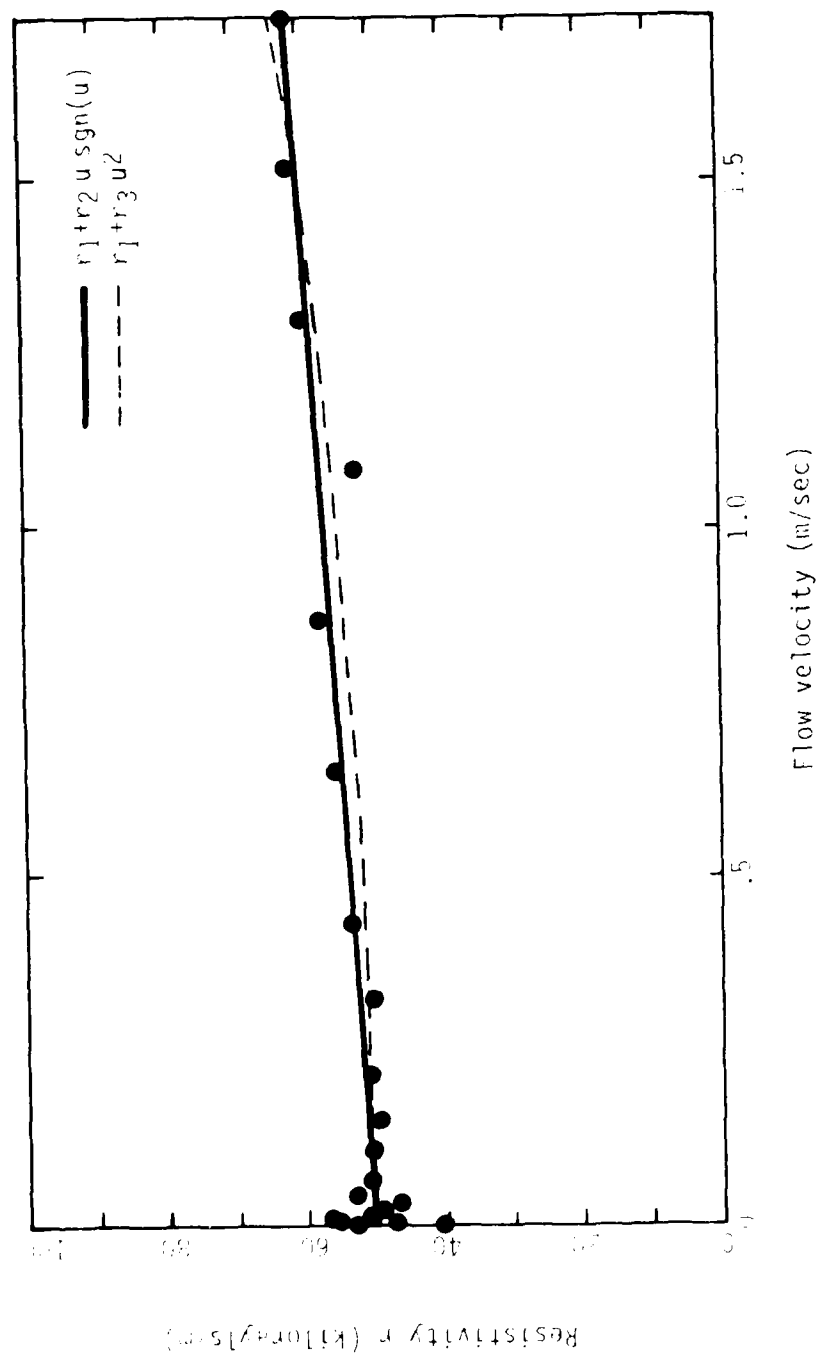
Figure 2-1

Measured static flow resistivity data
and empirically fitted curves

11

Measured data indicate that the resistivity depends on the flow velocity; a mathematical expression of the resistivity is sought which is appropriate for both ac and dc flows. Static flow resistivity data[†] (see Fig. 2-1) seem at first glance to indicate that the resistivity is of the form

$$r = r_1 + r_2 u \quad , \tag{2.6}$$

in which case

$$-dp/dx = r_1 u + r_2 u^2 \quad . \tag{2.7}$$

Closer examination, however, reveals the implausibility of using Eq. (2.7) for an ac signal: it suggests that the nonlinear contribution to the pressure gradient is positive regardless of the instantaneous direction of flow. If the discrepancy is to be remedied, the pressure gradient must not contain any even functions of u. The simplest improvement is to affix sgn(u) to the $r_2$ term in Eq. (2.7). The pressure gradient then becomes

$$-P_x = r_1 u + r_2 u^2 \mathrm{sgn}(u) \quad , \tag{2.8}$$

from which it follows that the resistivity has the form

$$r = r_1 + r_2 u \, \mathrm{sgn}(u) \quad , \tag{2.9}$$

where $u \, \mathrm{sgn}(u)$ is the instantaneous _speed_ of the flow. The coefficient $r_1$ is referred to as the linear resistivity because it plays a large part in determining the small-signal propagation effects. Similarly, the nonlinear resistivity is so called because it causes nonlinear behavior. Equation (2.9) is still compatible with the

---

[†]A detailed discussion of the data is given in Chapter 4. The large number of trials at small flow velocities was taken to find an accurate value of $r_1$.

$$\Omega_a\big|_{z_o} = \frac{1}{\text{area}} \iint D(x,y;z_o) \, dx \, dy \quad . \tag{2.3}$$

The average of the local value over all possible planes is the quantity $\langle \Omega_a \rangle$,

$$\langle \Omega_a \rangle = \frac{1}{\text{length}} \int \frac{1}{\text{area}} \iint D(x,y;z_o) \, dx \, dy \, dz_o \quad . \tag{2.4}$$

Note that Eq. (2.4) reduces to Eq. (2.1), so that in general

$$\langle \Omega_a \rangle = \Omega \quad .$$

The percent open area and the porosity must be equal because the aggregate open area of all infinitesimally thin slices defines the total open volume. This result is obtained regardless of the material geometry.

## 2. Resistivity

Viscous drag causes the material to resist the passage of an acoustic wave. The resistance per unit length is called the resistivity r, and is defined for a one-dimensional flow as follows.

$$dp/dx = -ru \quad , \tag{2.5}$$

where dp/dx is the pressure gradient parallel to the flow and u the flow velocity.

Since in general the details of the flow cannot be analyzed, the resistivity cannot be calculated explicitly and must therefore be measured directly. A dc flow test is the most straightforward way of measuring the resistivity. The fact that the dc flow resistivity also applies to oscillatory flows is not intuitively obvious, but Zorumski and Parrot[2] have shown that the ac and dc resistivities are indeed equivalent over a wide range of particle velocities. It is therefore possible to determine the ac resistivity of the medium by measuring the dc resistivity.

## B. Modeling

Porous materials in general have geometrically disorganized structures; the frame elements are arranged helter-skelter in near-random fashion. This fact makes detailed analysis of the hydrodynamic field virtually impossible. We therefore prefer to take a macroscopic viewpoint in which the summed effect of local flows determines the material properties.

### 1. Porosity

The porosity is defined as the fraction of the material volume which is filled with air. We have devised an abstract function $D(x,y,z)$ to describe the structure of a porous material; the function is merely a convenient mathematical construct and need not be directly measurable. The value of $D$ is 0 at a point occupied by a structural element and 1 otherwise. It therefore follows that the porosity is simply the value of $D$ averaged over a volume substantially larger than the mean pore size:

$$\Omega = \frac{1}{vol} \iiint D(x,y,z) \, dx \, dy \, dz. \tag{2.1}$$

The sample is assumed to be homogeneous and the porosity stationary throughout the sample. In practice, the porosity is determined by empirical means: the known densities of a sample $\rho_s$, the frame $\rho_f$, and the air trapped within $\rho_o$ combine in the relation

$$\Omega = (\rho_f - \rho_s)/(\rho_f - \rho_o) \quad . \tag{2.2}$$

While the porosity defines the fraction of volume occupied by air, the percent open area $\Omega_a$ defines the unobstructed fraction of a representative plane through which the flow passes. First, the local percent area $\Omega_a$ for a plane located at $z=z_0$ is

8

# CHAPTER 2

## THEORY AND MODELING

### A. Introduction

The theories of sound propagation which pertain most directly to the present investigation were reviewed in Chapter 1. In Chapter 2 we develop a simple model for studying propagation of high intensity sound through air-filled bulk porous absorbers. Some of the assumptions made have been used previously by other authors, namely,

1)   the frame is assumed rigid,[11,12]

2)   dc flow resistivity can be substituted for the ac value through-out,[2,13] and

3)   isothermal sound speed is appropriate for all frequencies of interest.[1]

The fourth assumption,

4)   hydrodynamic nonlinearities are small relative to the resistive nonlinearity,

is unique to the present work.

In Section B the concepts of porosity and resistivity are defined. Assumptions used in generating of the model are examined in detail. The continuity and momentum conservation equations, derived in Section C, are combined in Section D to produce a wave equation and the corresponding Helmholtz equation.

---

Because the process has been assumed isothermal, the energy equation is not needed in the derivation of the wave equation and is therefore not discussed here.

An outline of the current investigation is as follows. Chapter 2 begins with a section on material modeling. Equations of motion are then derived, which lead to a nonlinear wave equation and an infinite set of inhomogeneous Helmholtz equations. The solution of the Helmholtz equations and the predictions which can be made from them are given in Chapter 3. The chapter is divided into two sections: (1) propagation of low amplitude waves and (2) finite-amplitude effects. The second section is further divided into an analysis of the behavior of the fundamental and a study of the growth and decay of the harmonics. Chapter 4 is devoted to experiments. Discussions of the experimental apparatus and procedures are followed by a detailed comparison between theoretical predictions and measurements. Observed phenomena include excess attenuation of the fundamental, phase speed (of the fundamental) which _decreases_ with amplitude, and a cubic distortion pattern in the harmonics. Hysteresis in the amplitude dependent phase speed seems to imply the presence of a nonlinear bistability. Chapter 5 is a summary and conclusion of the first four chapters of the study, which constitute the thesis work. Chapter 6 was added after the thesis and presents an application of the theory to the acoustics of lined ducts. The vector wave equation is derived, and a frequency domain perturbation in the velocity potential is set up to solve the problems of reflection from a porous half-space and propagation in a lined duct. Appendix A gives a discussion of thermal effects on propagation in porous materials. A discussion of the alternative use of a resistivity model $r = r_1 + r_3 u^2$ is given in Appendix B. Appendix C contains the listing for and a short description of the computer program which calculates the numerical solutions.

There have been other investigations of the nonlinear properties of porous materials, but most are based on empirical observation of nonlinearly induced phenomena, with no clue about the relevant physical processes. Because they do not reveal the source of the nonlinearity, these studies have been of little value to the present work.

## C. Present Work

In the present investigation we seek a simple theory which quantifies the effects of amplitude dependent resistivity. In particular, we seek to explain and rectify the discrepancies between Kuntz's theory and experiment. The theory is based on the following model of the porous material: the material is rigid, incompressible and homogeneous, and it has only two important properties, porosity $\Omega$ and resistivity r. Knowledge of the microscopic structural details of the material is unnecessary. The porosity and resistivity are determined by direct measurement. The resistivity is shown to be the following function of velocity u: $r = r_1 + r_2 u \, \mathrm{sgn}(u)$. The effects of hydrodynamic nonlinearities, e.g., shock formation, are neglected, and sound propagation through the material is assumed to be isothermal. This model leads to a nonlinear wave equation, the solutions of which agree favorably with experimental observations.

Two of Kuntz's experiments have been repeated (with minor modifications): propagation of complex periodic signals, and dc flow resistivity measurements. Measurements were performed on batted Kevlar[R]29 in the 400 to 6200 Hz frequency range for small-signal waves, and 500 to 1500 Hz for finite-amplitude waves up to 165 dB source sound pressure level (SPL). The porosity of the samples ranged from $\Omega = 0.94$ to 0.98.

4

for Lambert's hypothesis is offered in Chapter 2. His work increased confidence in subsequent theories in which frame motion was neglected altogether. Kuhl and Meyer[12] were the first to introduce the following two crucial assumptions: (1) the dc flow resistance can be used directly in the momentum equation for acoustic signals, and (2) frame motion is negligible. Their theory provides the foundation for the present study.

Hersh and Walker[13] elaborated on Kuhl and Meyer's theory. They used hydrodynamic flow theory to formulate empirical relations between viscosity, porosity, fiber diameter, and resistivity. Heat transfer effects were also accounted for.[14]

Other influential linear theories (see, for example, Biot[15] and Lambert[16]) are comprehensive and generally quite useful. We are not able, however, to derive any benefit from them because their inherent complexity precludes extension for nonlinear behavior.

B. High-Amplitude Behavior

Zorumski and Parrot[2] combined theoretical work with experimental observation in their study of the amplitude dependent impedance of thin porous sheets. Most important, they showed that the ac resistivity is not only independent of frequency, but that it closely approximates the dc flow resistivity over a wide range of particle velocities as well. The equivalence of the ac and dc resistivity apparently proves the first assumption of Kuhl and Meyer.

Kuntz's investigation[1] builds on the best aspects of the contributions of Kuhl and Meyer and Zorumski and Parrot. However, a single error in Kuntz's expression for the nonlinear resistivity caused his theoretical predictions to differ markedly from his experimental observations.

The theoretical work has two hallmarks: (1) the theoretical model is very simple, and (2) the analysis is done in the frequency domain. The result is a relatively uncomplicated theory and predictions that compare favorably with experimental data over a wide range of intensities, frequencies, and input signals.

Since the number of investigations and treatments of porous material problems is vast, it is useful to show the relationship of the present work to that which has gone before. Because a thorough review of the literature has already been given by Kuntz,[1] we offer an abbreviated review to establish a succession of reference points.

## A. Small-Signal Theory

Rayleigh[3] was apparently the first to correlate sound absorption in porous materials with viscous and thermal losses occurring across the substantial internal surface area of the material. He characterized the material as a solid riddled with a multitude of narrow tubular channels. Rayleigh combined this model with the work of Kirchhoff[4] who had investigated the effect of viscosity and heat conduction on sound traveling in a narrow tube, to create the first modern theory of sound propagation in porous materials.

Many investigations which followed were based on Rayleigh's pioneering work.[5,6,7,8,9] The most prominent and thorough work along this line was performed by Zwikker and Kosten.[10] They took into account fiber motion, and also introduced the concept of the structure factor.

Lambert[11] discovered that above a certain frequency the gas motion and frame motion are indeed decoupled. The decoupling frequency depends on the material. For Kevlar[R]29, which figures heavily in the experimental phase of this work, the decoupling frequency is below 85 Hz for porosities above $\Omega = 0.94$. Support

2

# CHAPTER 1

## INTRODUCTION

Porous materials have proved useful as sound absorbers in high intensity environments, such as jet engine inlet ducts, where sound levels routinely exceed 140 dB. At this level most porous materials exhibit amplitude dependent properties, i.e., they act nonlinearly.[1,2] Although it is known that the nonlinearity significantly alters the efficiency of the absorber, the physical processes which cause the nonlinearity have not been well understood. Moreover, the precise effects of nonlinearity are not well documented. There is thus a need to understand more fully the high amplitude behavior of bulk porous materials.

Propagation of sound in porous materials is fundamentally different from that in an ordinary fluid. The acoustic flow encounters frictional resistance at each of the many gas/fiber interfaces. As a result the sound wave is attenuated, the phase speed reduced, and the impedance increased. The severity of these effects depends on frequency. For example, low frequency signals pass through the material more by diffusion than by propagation: attenuation and phase speed are both proportional to $\sqrt{f}$. At high frequency, on the other hand, the attenuation and phase speed reach constant values. Furthermore, because the frictional resistance increases with flow velocity, the acoustical properties also depend on amplitude. The combination of nonlinearity and diffusion causes some unusual and interesting behavior; it also makes the problem difficult to solve.

The present study covers high intensity sound propagation in air-filled fibrous bulk porous materials. The investigation is both theoretical and experimental.

layers must not overlap. If they do overlap the actual temperature distribution cannot be determined, but is expected to yield a sound speed that is more isothermal than Fig. 2-2 would indicate. The boundary layer interaction turns out to be significant at surprisingly high frequencies. The vertical lines which intersect the sound speed curves represent the frequencies below which the sound speed calculation cannot be trusted. A detailed discussion of how these frequencies are determined is given in Appendix A.

The results shown in Fig. 2-2 are based on the assumption of laminar flow conditions. The high particle velocities of intense waves, however, render the flow highly turbulent. Carman[17] has determined that the onset of turbulent flow in porous materials occurs when the modified Reynold's number

$$R_m = \frac{u}{\nu S} \qquad (2.13)$$

reaches a value in excess of unity, where $S = 4(1 - \Omega)/d$ is the surface area of the fibers per unit volume, d the fiber diameter, and $\nu$ is the kinematic viscosity. For Kevlar$^{®}$29 in porosities ranging from 0.98 to 0.94, the velocity at which turbulent flow begins is 0.1 to 0.3 m/sec, respectively. The flow velocities used in our experiments often exceed these values by as much as an order of magnitude: the assumption of laminar flow is clearly not applicable in these cases. Turbulent mixing of the fluid has a significant effect on the sound speed because it greatly improves the heat transfer between the air and the fibers. We therefore expect conditions to be significantly closer to isothermal than would be predicted from a laminar flow model. Since we are primarily interested in measurements at high intensity in frequency ranges where the boundary layer interaction is significant, we are justified in assuming the isothermal sound speed.

## 5. Relative Importance of Hydrodynamic Nonlinearity

Hydrodynamic nonlinear effects are extremely important for finite-amplitude progressive waves in an open medium, but their influence on wave propagation in porous materials is small. Many fine discussions of the physics of intense sound propagation in air already exist;[18,19,20,21] we shall cover only those points pertinent to the present discussion. An intense wave in an open medium distorts because the propagation speed $dx/dt$ varies over the waveform,

$$dx/dt = c_0 + \beta u(\chi, \tau) \quad ,$$

where $\beta \simeq (\gamma + 1)/2$ and $\gamma$ is the ratio of specific heats. The waveform distortion, which we shall call hydrodynamic distortion, is cumulative. An initially sinusoidal wave tends to distort into a sawtooth wave, i.e., a periodic sequence of shock waves. The shock formation distance

$$\bar{x} = 1/\beta \epsilon k_0 \quad ,$$

where $\epsilon = u_0/c_0$ is the dimensionless wave amplitude and $k_0 = 2\pi f_0/c_0$ is the wave number, serves as a measure of the rate of distortio. . If $\bar{x}$ is large the distortion builds up very slowly; the reverse is true if $\bar{x}$ is small. The shock formation distance in our experiments ranged from about 1.5 m to 5.5 km. These values should be compared with the characteristic length for the absorption,

$$x_a = 1/\alpha .$$

where $\alpha$ is the small-signal attenuation coefficient. Since values of $x_a$ for our experiments were between 2 and 9 cm, i.e., $\bar{x} \gg x_a$, the wave was completely absorbed before hydrodynamic distortion had a chance to develop. Furthermore, the effects of the nonlinear resistivity turn out to be much more severe than those for hydrodynamic distortion (see Chapter 3). Our experimental conditions are expected

to be typical of those encountered in practical uses of Kevlar as a high intensity sound absorber. We therefore assume the hydrodynamic nonlinearity to be negligible relative to the resistive nonlinearity and neglect any second and higher order terms not pertaining to the resistivity in the following derivation of the equations of motion.

### 6. Structure Factor

A true one-dimensional flow in a porous material exists only as a convenient fiction. In reality the flow is deflected by the frame in directions perpendicular to its net direction of travel. Some of the force applied in the x direction to a fluid particle is therefore wasted in the process of accelerating the fluid around obstacles. This inefficiency causes the fluid to appear more dense than it actually is. The effects of increased inertia are most notable at high frequency, where they cause the phase speed and attenuation to be reduced.

Most studies of porous materials include factors to account for the extra inertia. They are called by many names: structure factor, apparent density, tortuosity, and others. Some of the theoretical discussions of the underlying physics are quite elaborate.[10,15,22] Direct measurement of the structure factor is, however, not possible nor can one determine its value theoretically without considering the microscopic structural details of the material. Furthermore, the dependence on amplitude of the structure factor is not known. It seemed better to this author to do without such an enigmatic parameter, lest in our desire to assign it a numerical value we reduce it to a "fudge factor". We therefore choose to overlook the structure factor in formulating the equations of motion, physical significance notwithstanding.

18

## C. Equations of Motion

The foregoing discussion of the physics of acoustic flow in a porous material demonstrates that the resistivity effects far outweigh those of frame motion, frequency dependent sound speed, and hydrodynamic nonlinearity. The latter effects are therefore neglected so that needless complication is eliminated. The problem is thus reduced to a rather simple one: plane wave propagation through a "fluid" with one easily definable property, namely amplitude-dependent resistivity. The purpose of this section is to convert this physical understanding into equations of motion.

A number of general comments and definitions must be made at the outset. We are presently concerned with only one-dimensional aggregate flows. Local perpendicular flow components are assumed to sum to zero over a given plane. We define the control volume, depicted in Fig. 2-3, to be a differential section of length $\Delta x$ and cross-sectional area A. The material within the volume is homogeneous and has the same porosity throughout. Flow enters the volume at the left side through the open area $\Omega A$ and exits through the same area to the right. Pressures exerted on the sides of the control volume act on the entire cross-sectional area A, not just the open area. A resistive force due to viscous drag is presumed to act throughout the volume, not just in the pores. The velocity, density, and pressure are mean values across a given plane. The velocity and density are averaged only within the pores.

### 1. Continuity Equation

The equation of continuity mathematically expresses the balance between the rates of mass influx, efflux, and accumulation. At some instant in time the flow carries a certain amount of mass into the control volume through the open area at a

19
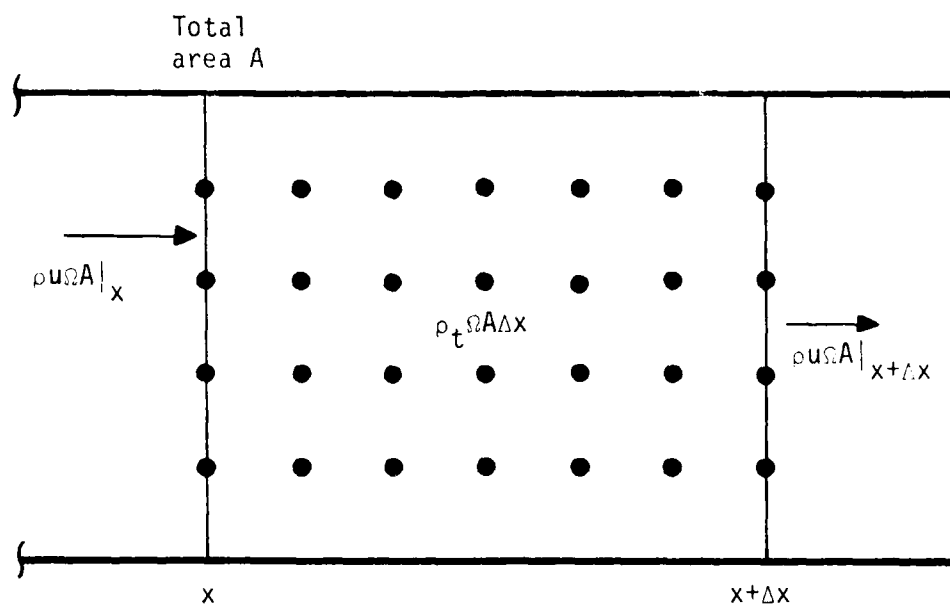
Figure 2-3

Stationary control volume for determination of the
conservation of mass relation for porous materials

AS-85-561

rate $(\rho u)(A\Omega)\big|_x$. Mass exits the volume at the rate $(\rho u)(A\Omega)\big|_{x+\Delta x}$. Since we expect the mass to be conserved, the difference between these two rates represents a rate of mass accumulation, $\rho_t \Omega A \Delta x$. The continuity equation may therefore be written as

$$\rho_t \Omega A \Delta x = \rho u \Omega A \big|_x - \rho u \Omega A \big|_{x+\Delta x} \quad . \tag{2.14}$$

The differential form of Eq. (2.14) is found by dividing by $\Omega A \Delta x$ and taking the limit as $\Delta x$ goes to zero:

$$\rho_t + (\rho u)_x = 0 \quad . \tag{2.15}$$

The porosity factor does not appear in this equation because the volume fraction in which the mass accumulates is equivalent to the area fraction through which the flow passes.[†]

Nonlinear terms not pertaining to the resistivity are neglected on the basis of the discussion in Section A.5 . Furthermore, we assume that there is no dc flow through the sample. We can therefore reduce Eq. (2.15) to the familiar linearized continuity equation

$$\rho_t + \rho_0 u_x = 0 . \tag{2.16}$$

2. Momentum Equation

The derivation of the momentum equation proceeds along similar lines. An identical control volume (depicted in Fig. 2-4) is established, but this time the momentum of the volume is considered. The rate of momentum accumulation $(\rho u)_t \Omega A \Delta x$ is balanced by the net momentum influx to the volume and body and surface forces acting on the control volume. Momentum enters the volume at the

---

[†] Particle velocity at or within a rigid obstacle is, of course, zero.

21
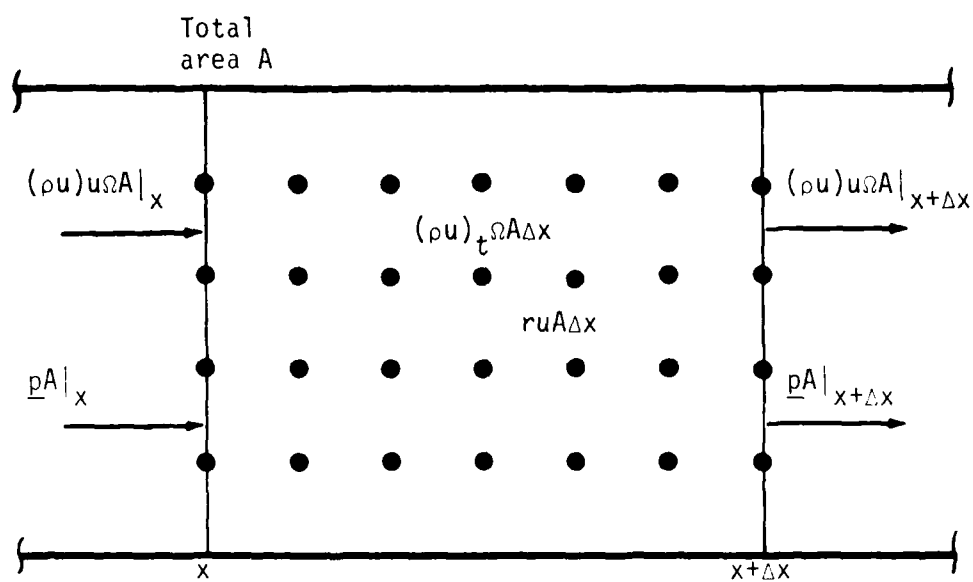
Figure 2-4

Stationary control volume for determination of the
conservation of momentum relation for porous materials

22

left at the rate $(\rho u) u \Omega A \big|_x$ and exits to the right at the rate $(\rho u) u \Omega A \big|_{x+\Delta x}$. Pressure exerted on the sides of the volume result in surface forces $\underline{p}A \big|_x$ at the left side and $\underline{p}A \big|_{x+\Delta x}$ at the right. A body force due to viscous drag $ru A \Delta x$ acts throughout the volume in opposition to the flow. Although the form of $r(u)$ is already known, it has been left in its general form for the moment.

The mathematical statement of conservation of momentum is

$$(\rho u)_t \Omega A \Delta x = (\rho u) u\, A \Omega \big|_x - (\rho u) u\, A \Omega \big|_{x+\Delta x} + \underline{p}A \big|_x - \underline{p}A \big|_{x+\Delta x} - ru\, A \Delta x \ . \qquad (2.17)$$

This equation is divided by $A \Delta x$ and take the limit as $\Delta x$ goes to zero to find the differential form

$$\Omega (\rho u)_t + \Omega (\rho u u)_x + \underline{p}_x + ru = 0 \quad . \qquad (2.18)$$

Again dropping hydrodynamic nonlinear terms, we obtain

$$\Omega \rho_o u_t + p_x + ru = 0 \quad . \qquad (2.19)$$

The porosity factor appears in Eq. (2.19) because the flow enters the control volume through an area determined by the porosity while the pressure and body force act on the entire surface and volume, respectively.

## 3. Pressure-Density Relation

We recall from Section B.4 that the gas within the pores is constrained to the ambient temperature value $T_o$ because of rapid convective heat transfer between the air and the frame. Equation (2.12) therefore reduces to

$$p = \rho R T_o \quad , \qquad (2.20)$$

where $c_i = \sqrt{R T_o}$ is the isothermal sound speed.

## D. Wave Equation

In the previous sections the continuity, momentum, and constitutive equations appropriate for high intensity sound propagation through rigid bulk porous materials were derived. The wave equation is found by combining these three relations. We first apply the differential operator $c_i^2 \partial/\partial x$ to the continuity equation and $\partial/\partial t$ to the momentum equation. Density and pressure terms cancel via Eq. (2.20), and the wave equations is found to be

$$\Omega u_{tt} - c_i^2 u_{xx} + \frac{(ru)_t}{\rho_o} = 0 \quad . \tag{2.21}$$

We adopt the sgn(u) model for the nonlinear component of r. Substitution of Eq. (2.9) in Eq. (2.21) yields

$$\Omega u_{tt} - c_i^2 u_{xx} + \frac{r_1}{\rho_o} u_t + \frac{r_2(u^2 \operatorname{sqn} u)_t}{\rho_o} = 0 \quad . \tag{2.22}$$

It turns out that solutions of Eq. (2.22) are best sought in the frequency domain. If the nonlinear term is ignored for the moment, we see that the behavior implied by Eq. (2.22) is a combination of lossless plane wave propagation

$$\Omega u_{tt} - c_i^2 u_{xx} = 0,$$

and a diffusion process

$$\frac{r_1}{\rho_o} u_t - c_i^2 u_{xx} = 0.$$

For most cases of practical interest the diffusive behavior is dominant; that is, the resistance term $r_1 u_t/\rho_o$ is much larger than the $\Omega u_{tt}$ term. The diffusion equation has wavelike solutions, but they are characterized by severe frequency dependent attenuation and dispersion. In particular, no general time domain solutions like

g(x+ct) or f(x-ct) for incoming or outgoing waves, respectively, can be found. Functions corresponding to incoming and outgoing waves are, however, identifiable in the frequency domain. It is therefore advantageous to transform Eq. (2.22) into its frequency domain counterpart, the Helmholtz equation.

Before transforming Eq. (2.22) we find it convenient to rewrite the equation in nondimensional form, vis.,

$$v_{\tau\tau} - \frac{v_{\chi\chi}}{\Omega} + R_1 v_\tau + R_2 (v^2 \text{sgn} v)_\tau = 0 \quad , \tag{2.23}$$

where

$$v = u/c_i \quad , \qquad\qquad R_1 = r_1/\Omega \rho_o \omega_o \quad ,$$

$$\tau = \omega_o t \quad , \qquad\qquad R_2 = r_2 c_i/\Omega \rho_o \omega_o \quad ,$$

$$\chi = \omega_o x/c_i \quad ,$$

and $\omega_o$ is a characteristic frequency, such as the fundamental frequency of the incident acoustic wave.

## 2. Helmholtz Equation

We now transform Eq. (2.23) to the frequency domain. The transformation is done in a manner popularized by Fenlon[23] and Korpel.[24] Time and distance dependences of the velocity variable $v(\chi,\tau)$ are separated by expanding v as a doubly infinite series of exponentials in time, with range dependent amplitude $V_n(\chi)$,[†]

$$v(\chi,\tau) = \sum_{n=-\infty}^{\infty} V_n(\chi) \exp(jn\tau) \quad . \tag{2.24}$$

---

[†] The index n represents the nth harmonic of the signal.

25

Since v is a real quantity, we require that $V_{-n}$ and $V_n$ be complex conjugates. The series approach is preferred to an integral transform because our incident signals are monochromatic or at least periodic. The nonlinear term contains the factor

v sgn(v), here abbreviated as $w(\chi, \tau)$, which represents the speed (not velocity) of the acoustic flow

$$w(\chi, \tau) \equiv \text{vsgnv} = \sum_{n=-\infty}^{+\infty} W_n(\chi) \exp(jn\tau) \quad , \tag{2.25}$$

and $W_{-n} = W_n^*$. The speed w corresponds to a full-wave rectified version of the signal, and the spectrum $W_n$ corresponds to the spectrum of the velocity-dependent resistivity.

Substitution of Eqs. (2.24) and (2.25) in Eq. (2.23) leads to the in-homogeneous Helmholtz equation,

$$V_n'' + q_n^2 V_n = jn\Omega R_2 \sum_p V_p W_{n-p} \quad , \tag{2.26}$$

where the double prime denotes two differentiations with respect to the argument $\chi$, and $q_n = n\sqrt{\Omega(1 - jR_1/n)}$ is the complex dimensionless wave number, which may be written

$$q_n = q_{nr} - j \, q_{ni} \quad . \tag{2.27}$$

The real and imaginary parts are

26

$$q_{nr} = n \sqrt{\frac{\Omega}{2} \left( 1 + \sqrt{1 + \left(\frac{R_1}{n}\right)^2} \right)} , \qquad (2.28)$$

and

$$q_{ni} = n \sqrt{\frac{\Omega}{2} \left( -1 + \sqrt{1 + \left(\frac{R_1}{n}\right)^2} \right)} . \qquad (2.29)$$

The polar forms are

$$q_{nr} = \left| q_n \right| \cos(\tan^{-1} Q_n) , \qquad (2.30)$$

$$q_{ni} = \left| q_n \right| \sin(\tan^{-1} Q_n) , \qquad (2.31)$$

where

$$\left| q_n \right| = n \sqrt{\Omega} \; \sqrt[4]{1 + \left(\frac{R_1}{n}\right)^2}$$

and

$$Q_n = \sqrt{\frac{-1 + \sqrt{1 + \left(\frac{R_1}{n}\right)^2}}{1 + \sqrt{1 + \left(\frac{R_1}{n}\right)^2}}} .$$

Despite its compact form, the inhomogeneous Helmholtz equation is extremely difficult to solve. Approximate solutions of Equation (2.26) are the subject of Chapter 3.

# CHAPTER 3

## SOLUTIONS

### A. Introduction

Chapter 3 is devoted to solutions of the inhomogeneous Helmholtz equation for progressive waves. Solutions for low intensity linear behavior are investigated in Section B. Examination of these solutions gives a basic understanding of the effects of resistivity on small-signal waves. An introduction to the theoretical problem of finite-amplitude waves in porous media is offered in Section C. An approximate first integral of Eq. (2.26) is developed that is the basis of the solutions in subsequent sections. In Section D, we investigate propagation of a tone subject to nonlinear resistivity effects. It is assumed here that the harmonic distortion products, though inevitable, are weak enough to be neglected. Concentrating, then, on the fundamental, we obtain approximate analytical solutions for pressure, particle velocity, phase velocity, and impedance magnitude and phase angle. Section E contains a discussion of the approximate solution for high intensity periodic waves in which the harmonics are taken into account. The multiplicity of harmonic interactions and interlocking solutions, as defined by the convolution term in Eq. (2.26), makes it necessary to seek a numerical solution. Harmonic propagation curves, i.e., amplitude versus distance for the various harmonic components, are generated. The numerical solution gives insight into the evolution of harmonic distortion products and in addition provides predictions against which experimental data may be compared.

A series of general expressions are now given in preparation for the analytical solutions discussed in Sections B and D. These definitions simplify the analysis and clarify the effects of resistivity in the linear and nonlinear regimes.

## 1. Velocity and Pressure

The particle velocity $v(\chi,\tau)$ can be expressed as an infinite sum of sinusoids with range dependent phases $\phi_{vn}(\chi)$ and amplitudes $A_n(\chi)$:

$$v(\chi,\tau) = \sum_{n=0}^{\infty} A_n(\chi)\left(\sin\ n\tau - \phi_{vn}(\chi)\right) \quad , \tag{3.1}$$

where $A_n(\chi)$ and $\phi_{vn}(\chi)$ are real and are related to $V_n$ (defined in Eq. (2.24)) by

$$V_n(\chi) = \frac{A_n(\chi)}{2j}\left(\exp\ -j\phi_{vn}(\chi)\right) \quad . \tag{3.2}$$

Use of the $A_n$ notation allows the amplitude and phase effects to be easily separated so that they may be considered independently.

The nondimensionalized pressure signal is defined as

$$\hat{p}(\chi,\tau) \equiv \frac{p(\chi,\tau) - P_o}{\rho_o c_i^2} = \sum_{n=-\infty}^{\infty} \hat{P}_n(\chi)\ \exp(jn\tau) \tag{3.3}$$

where $\hat{P}_{-n} = \hat{P}_n{}^*$ and, alternatively,

$$\hat{p}(\chi,\tau) = \sum_{n=0}^{\infty}\ _n(\chi)\ \sin\left(n\tau - \phi_{pn}(\chi)\right) \quad , \tag{3.4}$$

where $_n$ and $\phi_{pn}$ are real, and

For a progressive forward-traveling wavefield $B_n(0)$ is expected to be identically zero. Unfortunately, we are unable to accurately specify the boundary conditions for finite amplitude waves, so that $B_n(0)$ retains some residual value. Since the backward-traveling wave decays for decreasing $X$, it grows just as rapidly in the forward direction as the forward-traveling wave decays. Eventually a point is reached where the spurious backward-traveling wave solution obscures the desired solution. The larger the values of $q_{ni}$ the more rapidly the accuracy of the solution deteriorates.

In order to achieve a stable solution, the second order system of equations must be reduced to first order by applying the condition that the wave field is progressive. An exact first integral of Eq. (2.26), similar in form to Eq. (3.13), has not been found because of the complexity of the convolution term. We therefore seek an approximate first integral.

## 2. Approximate First Integral

The approximate first integral isolates forward wave behavior within Eq. (2.26), but does so at the expense of some accuracy. Since we seek solutions for the forward-traveling waves, we propose a solution of the form

$$V_n(X) = F_n(X) \exp(-jq_n X) \quad , \qquad (3.26) \quad ,$$

where the deviation of $F_n(X)$ from a constant value is due to nonlinear effects, and the exponential term represents small-signal effects for a forward-traveling wave. One may think of $F_n(X)$ as an apparent harmonic source amplitude which is allowed to vary with distance in response to nonlinear effects. Substitution into Eq. (2.26) gives

$$F_n'' - 2jq_n F_n' = jn\Omega R_2 \sum_p V_p W_{n-p} \exp(jq_n X) \quad . \qquad (3.27)$$

44

of the signal at the microphone closest to the source, which we call the reference microphone. Although the transducer input is always sinusoidal, various nonlinear processes cause the high amplitude signal to distort before it reaches the first microphone position; the signal at the initial point therefore contains all harmonics of the original tone. The SPL of the harmonics are measured and from these the harmonic pressure amplitudes $\hat{P}_n(0)$ are determined. These amplitudes serve as starting points for the solutions $\hat{P}_n(X)$, to which we compare the data from microphones at other positions.

In order to specify the solution of Eq. (2.26), it would be necessary to know the initial values (that is, the values at the initial point) of both $V_n$ and $V_n'$. However, only one of the boundary conditions can be synthesized from the pressure data; the value of $V_n'$ is linked to $\hat{P}_n$ through the continuity equation, Eq. (3.10). The remaining boundary condition, however, is the value of $V_n$ at the reference microphone. No exact general relation has yet been found between $\hat{P}_n$ and $V_n$. The value of $V_n$ must therefore be estimated. We tried using various successive approximation methods to obtain the necessary estimates but found solutions of Eq. (2.26) to be so unstable that all attempted approximation schemes ended in failure. The reason for the extreme instability is that the Helmholtz equation belongs to a class of differential equations called "stiff". In a stiff equation the real parts of the roots (eigenvalues) of the characteristic equation are widely separated, i.e., the values $|q_{ni}|$ are large. Attempted solutions based on one eigenvalue of the system are easily contaminated by errors (numerical and otherwise) which become forcing functions for the undesired solution.

A better understanding of this problem may be gained by examining the homogeneous solution of Eq. (2.26),

$$V_n(X) = B_n(0) \exp(jq_n X) + F_n(0) \exp(-jq_n X) \ . \tag{3.25}$$

43

The method of separating the amplitude and phase information developed in this section is applied in Section D to the problem of a finite-amplitude tone.

## C. Introduction to the Nonlinear Problem

The method of solution of Eq. (2.26) for finite-amplitude waves is dictated largely by the information available from the experiment. Without going into great detail, we can say that the experiment provides the harmonic pressure amplitudes $\hat{P}_n$ at several ranges for a progressive wavefield. While a single boundary condition per harmonic is available, the inhomogeneous Helmholtz equation, Eq. (2.26), is second order and thus requires two boundary conditions per harmonic. The missing condition is the radiation condition, for which we have found no general analytical expression. Without this expression we can neither specify the second boundary condition exactly, nor can we integrate Eq. (2.26), in which case one boundary condition would be sufficient. Moreover, the missing boundary condition cannot be estimated accurately enough to prevent the numerical solution from becoming unstable. An approximate first integral is therefore developed which allows a stable solution for a progressive wavefield. Errors arise in the approximate solution but they are at least qualitatively predictable.

For future reference we here introduce some special nomenclature. We are oftentimes concerned only with how the fundamental component of the wave propagates. The fundamental with higher harmonics neglected is, for simplicity, referred to as a "finite-amplitude tone". When the higher harmonics are included in the analysis the signal is referred to as a "distorted sinusoid".

### 1. Boundary Conditions

The boundary conditions are taken to be the harmonic pressure amplitudes

42
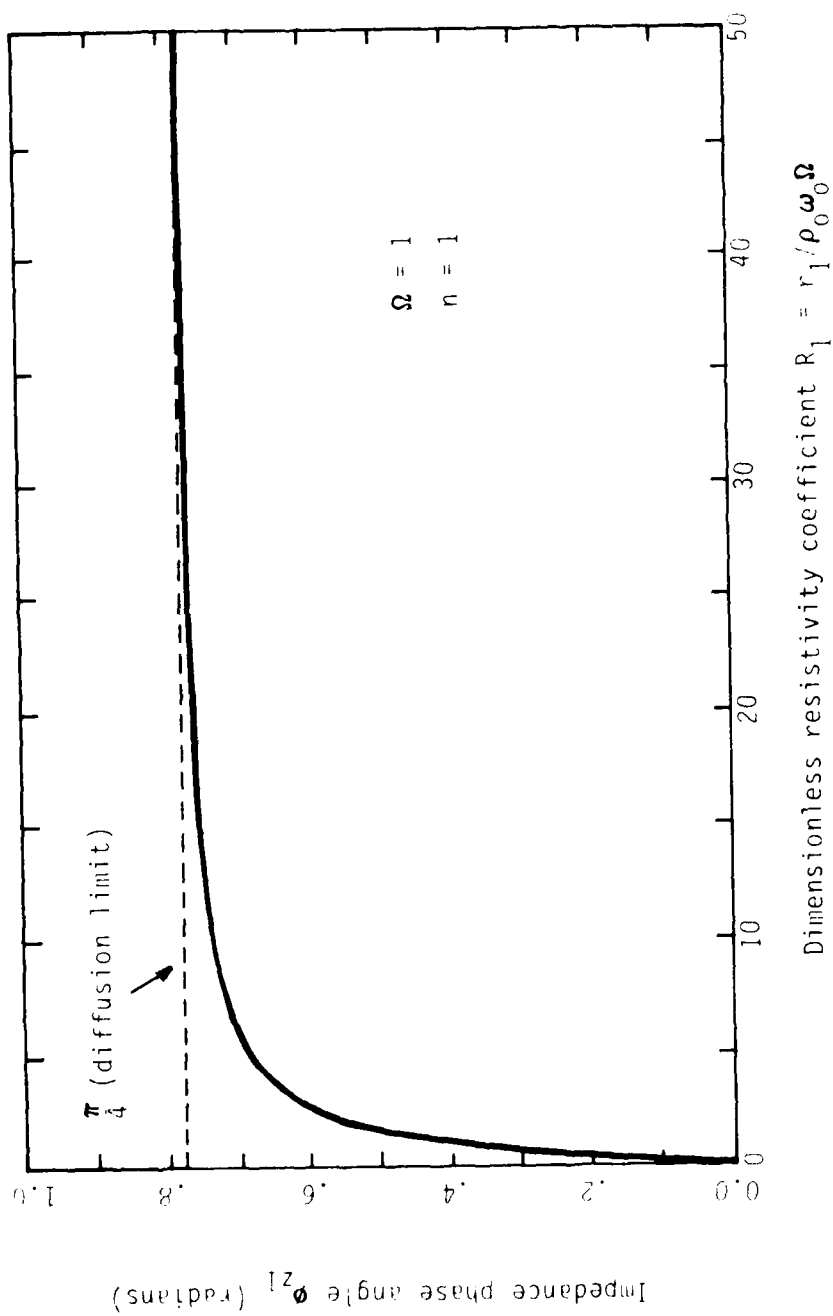
Figure 3-4

Impedance phase angle versus dimensionless
resistivity coefficient $R_1$

AS-85-566
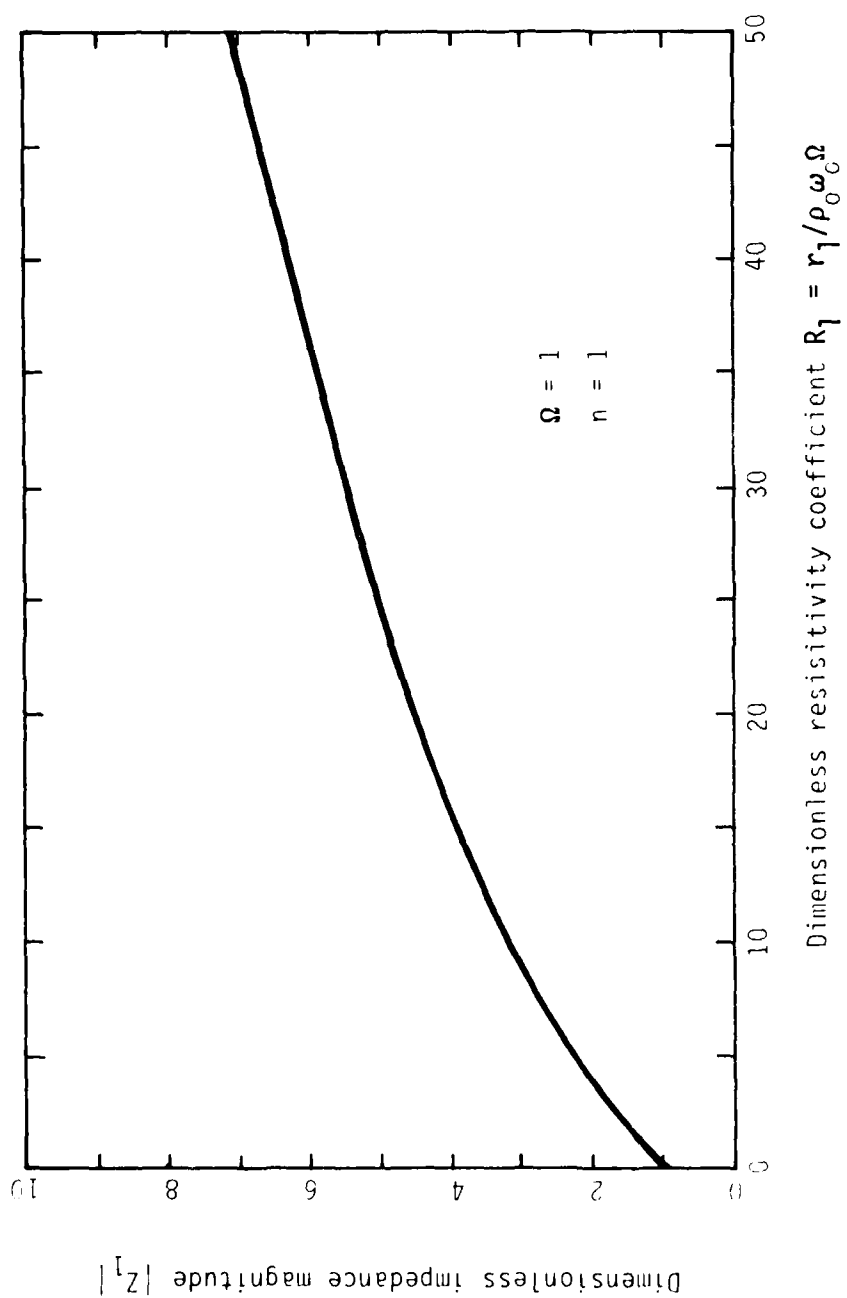
Figure 3-3

Dimensionless impedance magnitude versus
dimensionless resistivity coefficient $R_1$

AS-85-565

zero. Figure 3-3 illustrates the dependence of the impedence magnitude on $R_1$ and Fig. 3-4 does so for the impedance phase angle.

### 3. Small-Signal Pressure Wave Solution

The solution for pressure waves is found by simply taking the product of the particle velocity and impedance. Since $Z_n$ is independent of amplitude at low intensity, the pressure has a similar solution

$$\hat{p}(\chi,\tau) = \sum_{n=0}^{\infty} \Pi_n(\chi) \exp(-c_{ni}\chi) \sin\left(n\tau - q_{nr}\chi - \phi_{pn}(0)\right) \quad . \tag{3.23}$$

The phase velocity of the pressure wave and that of the particle velocity wave are therefore identical:

$$C_{pn} \equiv \frac{n}{\phi'_{pn}} = \frac{n}{q_{nr}} \quad . \tag{3.24}$$

The attenuation constant of the pressure signal is the same as well. This is the expected result.

### 4. Summary

The effects of resistivity on low intensity acoustic signals are summarized as follows: the linear resistivity coefficient $R_1$ is the most important parameter controlling the flow of acoustic energy, since it

1) causes attenuation,

2) causes dispersion, and an overall decrease in the component phase speeds, and

3) increases the impedance magnitude, and introduces a constant phase angle between the pressure and particle velocity signals.
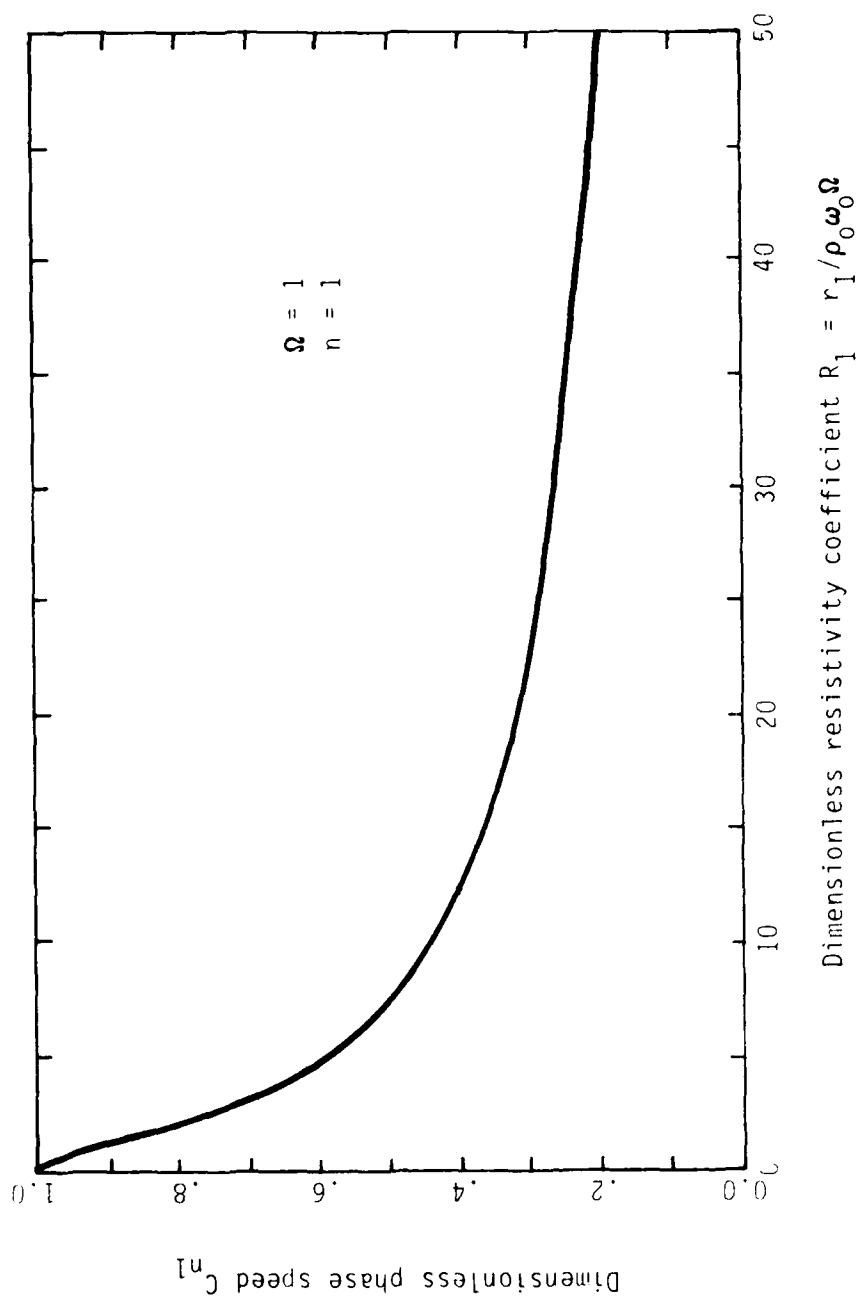
Figure 3-2

Dimensionless phase speed $C_{n1}$ versus
dimensionless resisitivity coefficient $R_1$

AS-85-564

Another effect of the resistivity is to reduce the phase speed of the wave. The phase speed is evaluated by combining Eqs. (3.6) and (3.17) to obtain

$$C_{vn} = \frac{n}{\phi'_{vn}} = \frac{n}{q_{nr}} \quad . \tag{3.21}$$

Resistivity causes the phase velocity to be substantially less at low frequencies than the sound speed. The dependence of $C_{vn}$ on $R_1$ can be seen in Fig 3-2, where once again a value of $\Omega = 1$ has been used for simplicity. The true phase speed value is $c = c_i C_{vn}$. The high and low frequency asymptotes, subject to frequency constraints on the theory, are the isothermal sound speed at high frequencies and

$$c = c_i \sqrt{\frac{2\omega}{r_1 \rho_o}}$$

at low frequencies. The low frequency phase speed and attenuation have $\sqrt{f}$ dependence which is indicative of a diffusion process.

### 2. Small-Signal Characteristic Impedance

The characteristic impedance is strongly affected by resistivity. Equations (3.16) and (3.17) are substituted into the general impedance relation, Eq. (3.11), to give

$$Z_n = \frac{1}{n} \left[ q_{nr} - j q_{ni} \right] = \frac{q_n}{n} \quad . \tag{3.22}$$

At low frequencies sound propagation is reduced to a diffusion process, characterized by an impedance magnitude of $\sqrt{r_1 / \rho_o \omega}$ and a phase angle of $45^o$. At high frequency the magnitude of the impedance approaches $\sqrt{\Omega}$ and reactance drops to

Attenuation constant, $q_{ni}$

Dimensionless resistivity coefficient $R_1 = r_1/\rho_o \omega_o \Omega$

$\Omega = 1$

$n = 1$
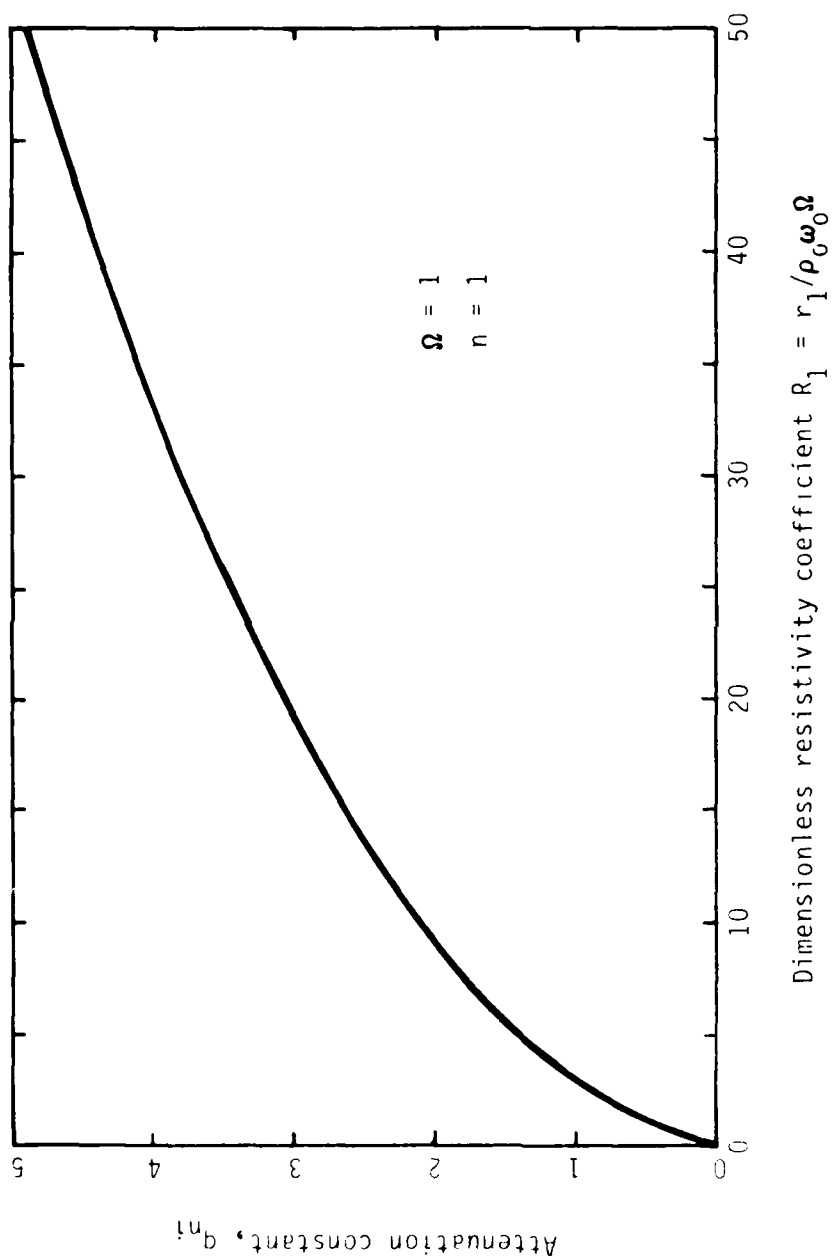
Figure 3-1

Dimensionless attenuation constant $q_{ni}$ versus dimensionless resistivity $R_1$

36

$$\phi_{vn}(\chi) = q_{nr}\chi + \phi_{vn}(0) \quad , \tag{3.19}$$

where $\phi_{vn}(0)$ is the value of $\phi_{vn}(\chi)$ at the effective origin and we see that $q_{nr}$ is the propagation wave number. The general solution for the particle velocity for small-signal progressive waves is therefore

$$v(\chi,\tau) = \sum_{n=0}^{\infty} A_n(0) \exp(-q_{ni}\chi) \sin\left(n\tau - q_{nr}\chi - \phi_{vn}(0)\right) \quad . \tag{3.20}$$

One effect of the resistivity is to attenuate the wave as it travels. The nondimensional rate of attenuation varies according to Eq. (2.29), with the dimensionless grouping $R_1$ defined in Eq. (2.23). Figure 3-1 is a graph of Eq. (2.29) where for simplicity the value $\Omega = 1$ has been used. It is seen that the attenuation increases with the dimensional resistivity $r_1$ and frequency. The dependence of $q_{ni}$ on porosity is complicated because $r_1$ is itself a function of porosity. The range $0 < R_1 < 50$ is sufficient to cover the audio spectrum for most materials. At high frequency ($R_1 \ll 1$) the true attenuation, $\alpha = \omega q_{ni} c_i$, reaches an asymptotic value $\alpha = r_1/2\rho_o c_i$, which is independent of frequency. The low frequency asymptotic result is

$$\alpha = \frac{1}{c_i} \sqrt{\frac{r_1 \omega}{2\rho_o}} \quad ,$$

which is proportional to $\sqrt{f}$ just as in the case of boundary layer dominated attenuation. The high and low frequency results are not very useful, however, because the isothermal sound speed is inappropriate at very high or very low frequencies, nor is the frame rigid at low frequencies.

$$V'_n + jq_n V_n = 0 \qquad (3.13)$$

and

$$V'_n - jq_n V_n = 0 \quad . \qquad (3.14)$$

Equation (3.13) is the relation for the forward traveling wave, Eq. (3.14) for a backward traveling wave. We now concentrate on Eq. (3.13), which may be interpreted as a first integral of the Helmholtz equation for forward traveling signals.

Amplitude and phase information may be obtained by substituting Eq. (3.1) into Eq. (3.13); one finds that

$$A'_n + j(q_n - \varphi'_{vn})A_n = 0 \quad . \qquad (3.15)$$

The real and imaginary parts of this equation give relations for the amplitude and phase, respectively, vis.,

$$A'_n + q_{ni}A_n = 0 \quad , \qquad (3.16)$$

and

$$q_{nr} - \varphi'_{vn} = 0 \quad , \qquad (3.17)$$

where $q_{nr}$ and $q_{ni}$ are given by Eqs. (2.27) through (2.31).

### 1. Particle Velocity Solution

Solutions of differential equations (3.16) and (3.17) are quite simple. The range dependent amplitude is

$$A_n(\chi) = A_n(0) \exp(-q_{ni}\chi) \quad , \qquad (3.18)$$

where $A_n(0)$ is the value of $A_n(\chi)$ at the effective origin of the signal. Thus $q_{ni}$ is the decay constant. The phase function is

$$jn\hat{P}_n + V'_n = 0 \quad . \tag{3.10}$$

We first divide Eq. (3.10) by $V_n$,

$$jnZ_n + \frac{V'_n}{V_n} = 0 \quad ,$$

and then substitute for $V_n$ and $V_n'$ using Eq. (3.2) to solve for $Z_n$,

$$Z_n = \frac{1}{n} \left[ \phi'_{vn} + j \frac{A'_n}{A_n} \right] \quad . \tag{3.11}$$

It is interesting to note that the rate of change of phase of the wave represents the real impedance while changes in the wave amplitude represent the reactive part.

B. Low Intensity

Attenuation and phase velocity are controlled at low intensity by the dimensionless linear resistivity coefficient $R_1$. The Helmholtz equation takes the linear form

$$V''_n + q_n^2 V_n = 0 \tag{3.12}$$

for small signals. This second order differential equation may be factored into two first order relations by use of operational notation. Equation (3.12) is first written as

$$( D_\chi^2 + q_n^2 ) V_n = 0 \quad ,$$

or

$$( D_\chi + j q_n )( D_\chi - j q_n ) V_n = 0 \quad ,$$

where $D_\chi$ represents differentiation with respect to $\chi$. The "roots" of this factored equation are

33

## 3. General Definition of Characteristic Impedance

The characteristic impedance is defined in general as the ratio of the pressure to the particle velocity for a given harmonic component:

$$Z_n = \frac{\hat{P}_n}{V_n} = \frac{\Pi_n}{A_n} \exp\left(-j(\phi_{pn} - \phi_{vn})\right) \quad .$$

(3.8)

If $Z_n$ is written in polar form,

$$Z_n = |Z_n| \exp(-j\phi_{zn}) \quad ,$$

(3.9a)

it follows that

$$|Z_n| = \frac{\Pi_n(\chi)}{A_n(\chi)}$$

(3.9b)

and

$$\phi_{zn} \equiv \tan^{-1}\left(\frac{-\mathrm{Im}(Z_n)}{\mathrm{Re}(Z_n)}\right) = \phi_{pn} - \phi_{vn} \quad .$$

(3.9c)

A general relation for the impedance can be found by using the continuity equation which, although linear in form, provides a relation appropriate for all amplitudes because the hydrodynamic nonlinear terms have been neglected. We first replace $\rho_t$ in Eq. (2.16) by $p_t/c_i^2$ and then nondimensionalize the result to find

$$\hat{p}_\tau + v_\chi = 0 \quad .$$

Equations (3.1) and (3.3) are here substituted into this equation to give the dimensionless continuity equation in terms of the harmonic components,

$$\hat{P}_n(\chi) = \frac{\Pi_n(\chi)}{2j} \exp\left(-j\phi_{pn}(\chi)\right) \quad . \tag{3.5}$$

## 2. Phase Velocity

A general expression for phase velocity, applicable in both the linear and nonlinear cases, may now be derived using the notation of Eqs. (3.1) and (3.4). The phase speed is defined as the rate of travel of a constant phase plane, that is, a plane for which the quantity $n\tau - \phi_{vn}(\chi)$ remains constant. Upon differentiating this expression we find that

$$n\, d\tau - \phi'_{vn}\, d\chi = 0 \quad ,$$

where the prime again denotes differentiation with respect to the argument $\chi$. The phase velocity of the nth component of the particle velocity wave is therefore

$$C_{vn} \equiv \frac{d\chi}{d\tau}\bigg|_{\substack{\text{const.}\\ \text{phase}}} = \frac{n}{\phi'_{vn}} \quad . \tag{3.6}$$

The phase velocity for the pressure signal is similarly defined as the rate of travel of a plane for which $n\tau - \phi_{pn}(\chi)$ stays constant,

$$C_{pn} \equiv \frac{d\chi}{d\tau}\bigg|_{\substack{\text{const.}\\ \text{phase}}} = \frac{n}{\phi'_{pn}} \quad . \tag{3.7}$$

Two phase velocities are defined because the impedance phase angle is amplitude dependent at high intensity and therefore the pressure and particle velocity signals travel at different speeds.

31

Note that this substitution has not reduced the number of eigenvalues in the problem; to accomplish this feat an integration is necessary. The danger of contamination by spurious backward-traveling waves still remains. We have, however, shifted the eigenvalues of the linear problem to 0 and $2jq_n$, so that we can take advantage of the differing relative importance of the terms $F_n"$ and $F_n'$ for the two wave types. The following analysis is carried out as if there were no backward waves, and it is this selective vision which accomplishes the integration. For forward-traveling waves where the nonlinearity is moderate, the transition between nonlinear and linear behavior is thought to be sufficiently gradual to warrant the assumption that $F_n"$ can be neglected relative to $F_n'$. Removal of the $F_n"$ term results in a truncated version of Eq. (3.27),

$$F_n'(\chi) = -n \frac{\Omega R_2}{2q_n} \sum_p V_p W_{n-p} \exp(jq_n \chi) \quad . \tag{3.28}$$

In effect an approximate first integral of Eq. (2.26) has been obtained,

$$V_n' + jq_n V_n = -n \frac{\Omega R_2}{2q_n} \sum_p V_p W_{n-p} \quad . \tag{3.29}$$

The fact that Eq. (3.29) is the appropriate first integral is proved by noting that the relation $|F_n"| << |2q_n F_n'|$ is not satisfied by a backward-traveling wave. Equation (3.29) is therefore an approximate differential equation governing progressive waves.

### 3. Solution Errors

In the process of rejecting the spurious solution, a certain amount of information regarding the spatial dependence of $V_n$ has been lost. Implicit in

45

Eq. (3.29) is the supposition that the transition between nonlinear and linear behavior is gradual. For very large amplitude waves, however, the transition is relatively rapid and $F_n''$ is not negligible. The errors of the approximate solution that result are called "overshooting" after their graphical manifestation. Non-linearly induced gains and losses for the fundamental and various harmonics (see Section E) of the signal are predicted too large. Since the exact solution is not known, there is no way to quantify the errors of the approximate solution. The errors will, however, become apparent when the solution is compared with measured data in Chapter 4.

## D. Propagation of a Single Tone

We now consider propagation of a single tone of finite amplitude. The effects of the inevitable harmonic distortion components on the tone are neglected because the higher harmonics are very weak relative to the fundamental. With the aid of the approximate first integral, we are able to find analytical expressions governing the amplitude and phase of the wave and the impedance of the medium.

Analytical solutions of Eq. (3.29) are obtained for a tone

$$v(\chi,\tau) = A_1(\chi) \sin\left(\tau - \phi_{v1}(\chi)\right) \quad , \qquad (3.30)$$

which has spectral components $V_1 = (A_1/2j)\exp(-j\phi_{v1}(\chi))$, and $V_{-1} = V_1{}^*$. Since these are the only harmonic components assumed to exist, the convolution term of Eq. (3.29) is shortened considerably:

$$V_1' + jq_1 V_1 = \frac{-\Omega R_2}{2q_1} \left(V_1 W_o + V_1^* W_2\right) \quad . \qquad (3.31)$$

46

The spectrum $W_n$ of the full-wave rectivied version of an arbitrary signal is usually too complicated to analyze. In the pure tone case, however, it is straightforward. The rectified signal is defined as

$$A_1(X) \left| \sin(\tau - \phi_{v1}(X)) \right| \quad .$$

Application of the Fourier transform gives

$$W_n(X) = \frac{A_1(X) \exp\left(-jn\tau'\phi_{v1}(X)\right)}{2\pi} \left[ \int_0^\pi \sin(\tau') \exp(-jn\tau') d\tau' - \int_\pi^{2\pi} \sin(\tau') \exp(-jn\tau') d\tau' \right] \quad ,$$

where $\tau' = \tau - \phi_{v1}(X)$. Finally, evaluation of the integrals yields

$$W_n(X) = \frac{2A_1(X)}{\pi(1-n^2)} \exp\left(-jn\phi_{v1}(X)\right) \tag{3.32}$$

for $n$=even and 0 otherwise.

A differential equation in $A_1$ and $\phi_{v1}$ arises when we substitute Eq. (3.30) and (3.32) into Eq. (3.31),

$$A_1' + j(q_1 - \phi_{v1}')A_1 = \frac{-\Omega R_2}{q_1} \frac{4}{3\pi} A_1^2 \quad . \tag{3.33}$$

As in the linear analysis (Section B), the real and imaginary parts of Eq. (3.33) give separate relations for amplitude and phase information,

$$A_1' + q_{1i}A_1 = -Kq_{1r}A_1^2 \quad , \tag{3.34a}$$

and

$$q_{1r} - \phi_{v1}' = -Kq_{1i}A_1 \quad , \tag{3.34b}$$

where

$$K = \frac{4R_2}{3\pi \sqrt{1 + R_1^2}}$$   (3.35)

is the coefficient of resistive nonlinearity. For the Kevlar samples used in our experiments the value of K was often 20 or greater. Since the hydrodynamic distortion effects would have been scaled by the dimensionless coefficient $\beta=1.2$, we see that it is indeed correct to neglect them.

The amplitude of the particle velocity wave is found by integrating Eq. (3.34a) directly,

$$A_1(X) = \frac{A_1(0) \exp(-q_{1i}X)}{1 + \Gamma\left(1-\exp(-q_{1i}X)\right)} \quad ,$$   (3.36)

where $\Gamma=KA_1(0)/Q_1$, which is directly analogous to the Gol'dberg number.[†] Figure 3-5 gives plots of $\log(A_1)$ versus distance for various initial particle velocity amplitudes. Low intensity waves experience simple exponential decay. Hence, the corresponding curves are straight lines. High amplitude waves, however, undergo excess attenuation as a result of nonlinear resistivity. As a result, the propagation curves bend. For very high source amplitudes the pressure amplitude approaches an asymptote (the dotted line in Fig. 3-5): the amount of energy that can be transmitted to a given point cannot be exceeded regardless of the starting

--------

[†] The Gol'dberg number, which was originally developed for distortion due to nonlinear effects in nonporous fluids, measures the relative importance of the nonlinear distortion effects to small-signal attenuation.
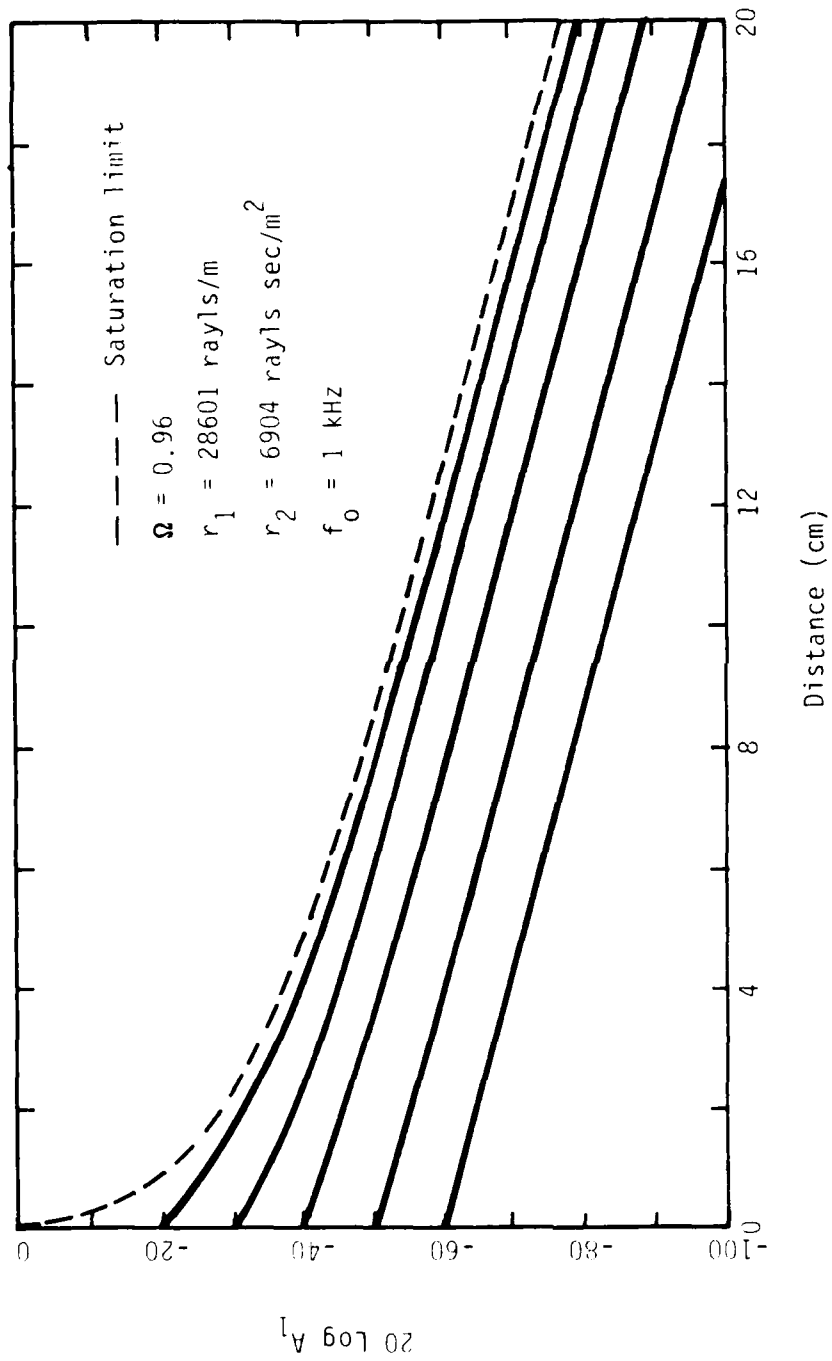
Figure 3-5

Particle velocity amplitude of fundamental component
versus distance for various initial amplitudes

amplitude. The "saturation"[25] limit is determined by the properties of the medium and is independent of the initial amplitude.

Although some have heretofore thought the excess attenuation in porous materials is due to conventional nonlinear effects in the fluid, we now see that the true cause is nonlinear resistivity. Equation (3.36) is of the same form as the equation derived by Webster and Blackstock[25] to describe excess attenuation and saturation of a nonlinearly propagating pure tone in free air. In their model, excess attenuation and saturation are a direct consequence of shock formation. Intense sound waves in porous media, however, do not form shock waves because the harmonics are rapidly attenuated and dispersed. The form of Eq. (3.36) was also obtained by Kuntz[1] as a result of his empirical model of attenuation of a tone in a porous medium. The fact that Eq. (3.36) can be derived analytically proves that the basis of Kuntz's model was correct.

The phase speed of the particle velocity wave is affected by the nonlinearity in a rather unexpected way. Substituting Eq. (3.10) into Eq. (3.6), we obtain

$$C_{v1} = \frac{1}{\phi'_{v1}} = \left[ q_{1r} + K q_{1i} A_1 \right]^{-1} \quad . \tag{3.37}$$

The phase speed is seen to depend on the inverse of the propagation wave number $q_{1r}$ at low intensity, but the amplitude dependence causes $C_{v1}$ to decrease at high amplitude (see Fig. 3-5). A high intensity wave therefore starts by propagating slowly, but as the wave is attenuated the phase velocity increases, eventually reaching the linear value $q_{1r}^{-1}$. The resemblance of the characteristic shape of the curve in Fig. 3-6 and that in Fig. 3-2 should be noted.

In Chapter 4 the relative phase between two points is measured as an indication of the phase speed, to which it is closely related. Equation (3.34b) can be
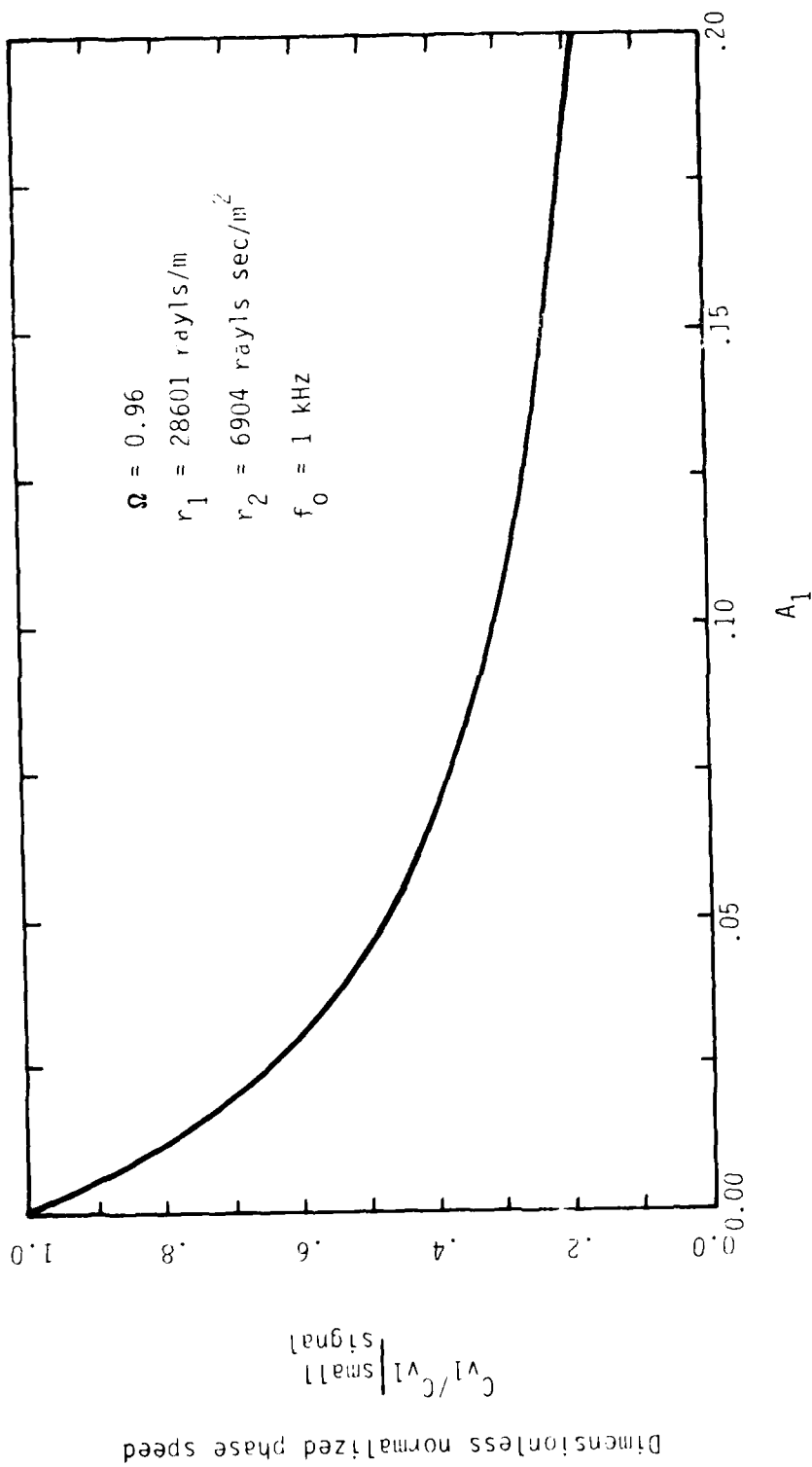
Figure 3-6

Dimensionless normalized phase speed versus dimensionless
particle velocity amplitude for fundamental component

AS-85-568

integrated to give the phase function

$$\phi_{v1}(X) = q_{1r}X + Q_1 \ln\left(1 + \Gamma\left(1-\exp(-q_{1i}X)\right)\right) + \phi_{v1}(0) \quad . \tag{3.38}$$

The nonlinearly induced decrease in the phase speed is manifested here in the logarithmic term, which represents the increased relative phase at high intensity between two points. The full particle velocity solution is therefore

$$v(X,\tau) = \frac{A_1(0)\exp(-q_{1i}X)}{1 + \left(1-\exp(-q_{1i}X)\right)}$$

$$\times \sin\left(\tau - q_{1r}X - Q_1\ln\left(1+\Gamma\left(1-\exp(-q_{1i}X)\right) - \phi_{v1}(0)\right) \quad . \tag{3.39}$$

The impedance of the wave is strongly amplitude dependent. The general impedance relation Eq. (3.10), combined with Eqs. (3.34a) and (3.34b), gives

$$Z_1 = (q_{1r} + Kq_{1i}A_1) - j(q_{1i} + Kq_{1r}A_1) \quad , \tag{3.40a}$$

or

$$Z_1 = q_1 - jKA_1 q_1^* \quad . \tag{3.40b}$$

The magnitude of the impedance can, after some manipulation, be shown to be

$$|Z_1| = \left(|q_1|^2\left(1+(KA_1)^2\right) + 2R_1 KA_1\right)^{1/2} \quad , \tag{3.41a}$$

which can be approximated by

$$|Z_1| \simeq |q_1|(1 + KA_1) \tag{3.41b}$$

when $R_1$ is sufficiently greater than unity. As one may readily observe from Eq. (3.41b) and Fig. 3-7, the impedance magnitude increases linearly with particle
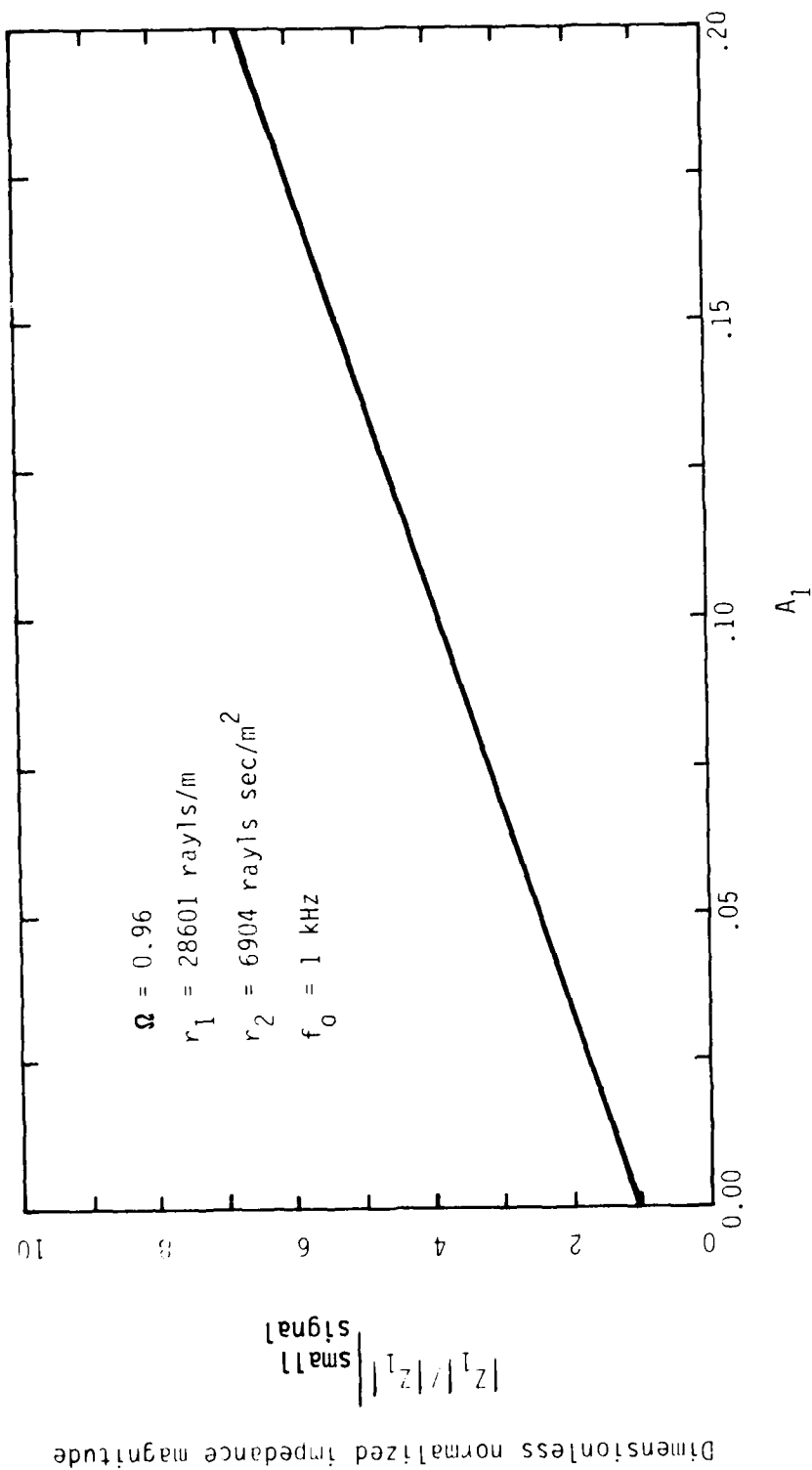
Figure 3-7

Dimensionless normalized impedance magnitude versus dimensionless
particle velocity amplitude for fundamental component

AS-85-569

velocity. The phase angle of the impedance is

$$\phi_{z1} = \tan^{-1}\left(\frac{q_{1i} + Kq_{1r}A_1}{q_{1r} + Kq_{1i}A_1}\right) \quad . \tag{3.42}$$

Once again the phase information gives a surprising result. The impedance phase angle varies between a high intensity asymptote $\tan^{-1}(1/Q_1)$ and a low intensity limit $\tan^{-1}(Q_1)$. The material is relatively more reactive at high amplitude; as the wave travels and is attenuated, the reactance approaches its low intensity value. The amplitude-dependent impedance phase angle has interesting consequences for the pressure wave phase velocity, as we shall see shortly. A plot of Eq. (3.42) appears in Fig 3-8.

The solution for finite-amplitude pressure waves is again simply the product of the particle velocity and impedance,

$$\hat{p}(x,\tau) = A_1(x) \, Z_1(x) \, \sin\left(\tau - \phi_{v1}(x) - \phi_{z1}(x)\right) \quad . \tag{3.43}$$

The pressure signal is subject to excess attenuation and saturation just as the particle velocity is. But since the impedance magnitude is amplitude dependent, the functional dependence is slightly different. Although not apparent from Fig. 3-7, the impedance reaches a high amplitude limiting value which is determined by the particle velocity amplitude at saturation. The product of the saturation limits of the impedance and particle velocity as a function of $x$ gives the high intensity pressure amplitude asymptote. Propagation curves for various initial pressure amplitudes are given in Fig. 3-9.

The most surprising result of this section comes when we consider the phase velocity of the pressure wave which, from Eq. (3.7) and the definition of impedance phase angle, is
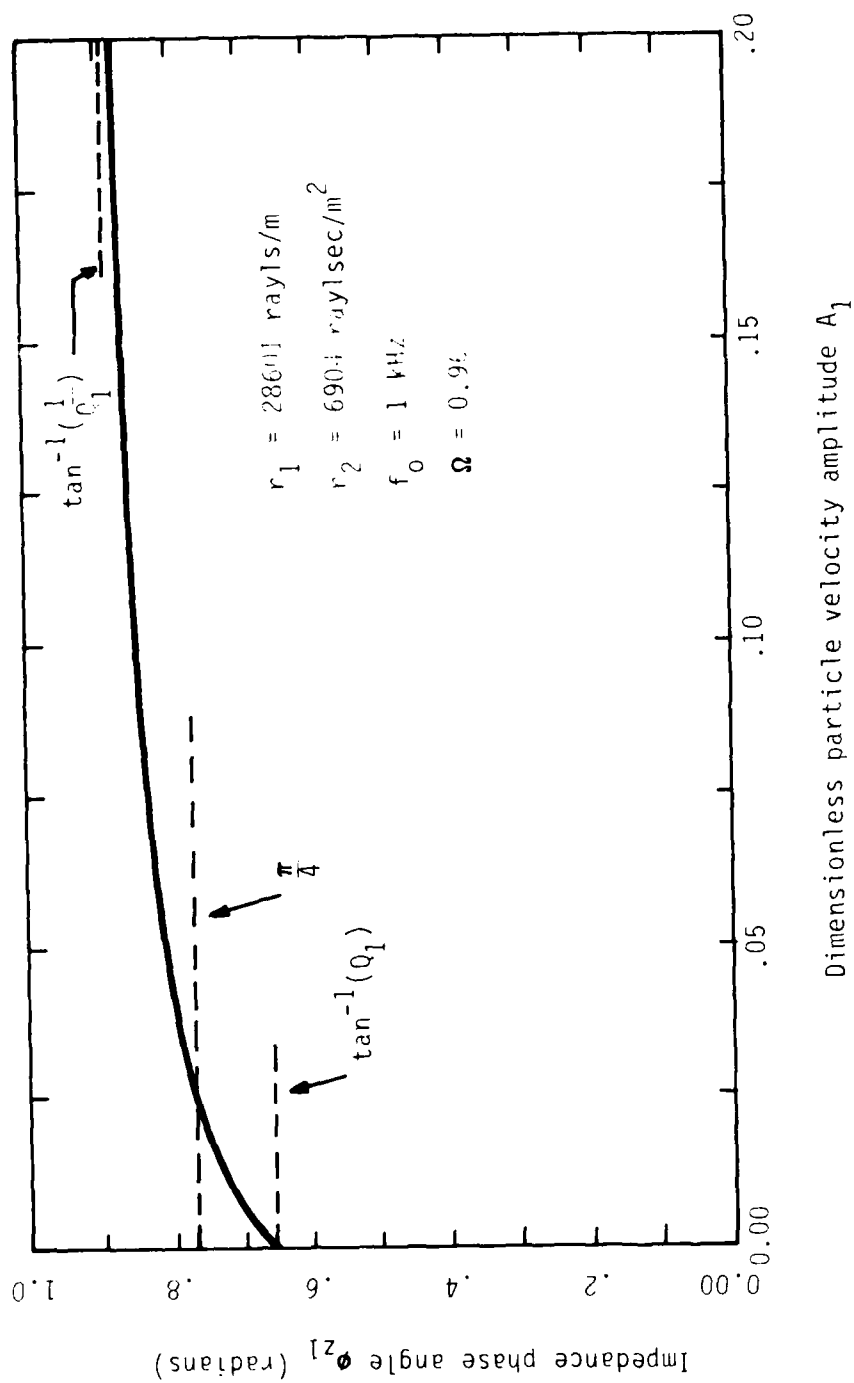
Figure 3-8

Impedance phase angle $\varphi_{z1}$ versus dimensionless
particle velocity amplitude
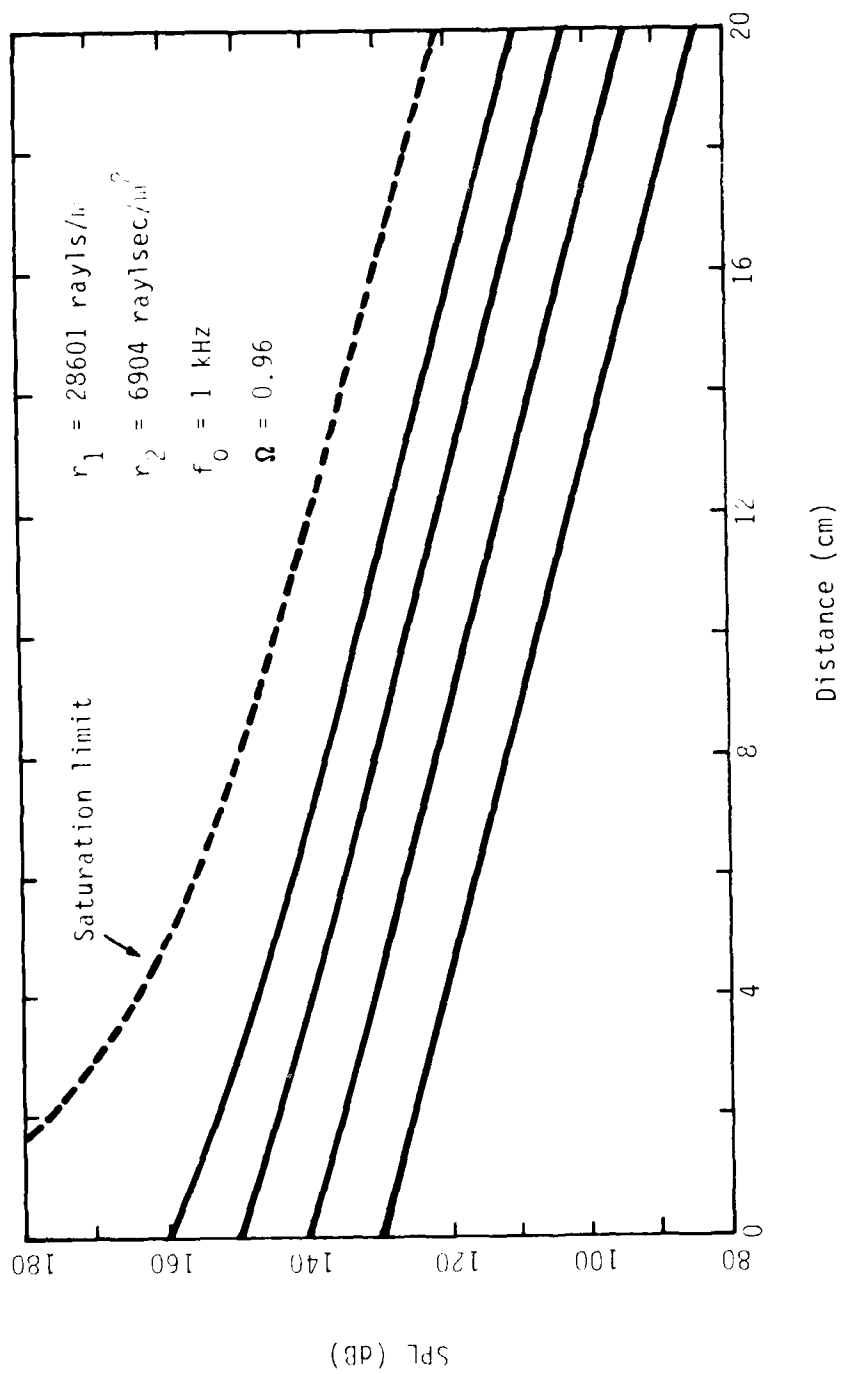
Figure 3-9

Fundamental SPL versus distance
for various initial amplitudes

$$C_{p1} = (\phi'_{p1})^{-1} = (\phi'_{v1} + \phi'_{z1})^{-1} \quad . \tag{3.44}$$

This phase speed is different from that for the particle velocity because at large amplitudes $\phi'_{z1}$ does not equal zero. The value of $\phi'_{v1}$ has previously been given, but the value of $\phi'_{z1}$ must be obtained by differentiating Eq. (3.42) with respect to $x$. It can be shown that the rate of change in the impedance phase angle with distance is

$$\phi'_{z1}(x) = \frac{-q_{1i}Q_1 B \exp(-q_{1i}x)}{\left(1 - B \exp(-q_{1i}x)\right)^2 + Q_1^2} \tag{3.45}$$

where

$$B = \frac{\Gamma(1-Q_1^2)}{1 + \Gamma} \quad .$$

The $\phi'_{z1}$ term opposes the $\phi'_{v1}$ term. The pressure signal therefore travels slightly faster than the particle velocity signal. As the wave is attenuated, the phase speeds of the two waves eventually converge to their mutual small-signal value $q_{1r}^{-1}$. In Fig. 3-10 the pressure phase velocity $C_{p1}$ is shown as a function of distance for a given source level. The corresponding curve for $C_{v1}$ is provided for comparison. This phenomenon has been observed during the course of our experiments, and is reported in Chapter 4.

Several general conclusions can be made regarding the effects of high intensity on propagation of a finite-amplitude single tone:

1) The nonlinearity causes excess attenuation and, in the limit, saturation.

2) The phase velocity is less than its small-signal value.

Distance (cm)

$C_{p1}$
$C_{v1}$

$r_1 = 28601$ rayls/m

$r_2 = 6904$ rayls$\cdot$sec/m$^2$

$f_0 = 1$ kHz

$\Omega = 0.96$

SPL(0) = 170 dB
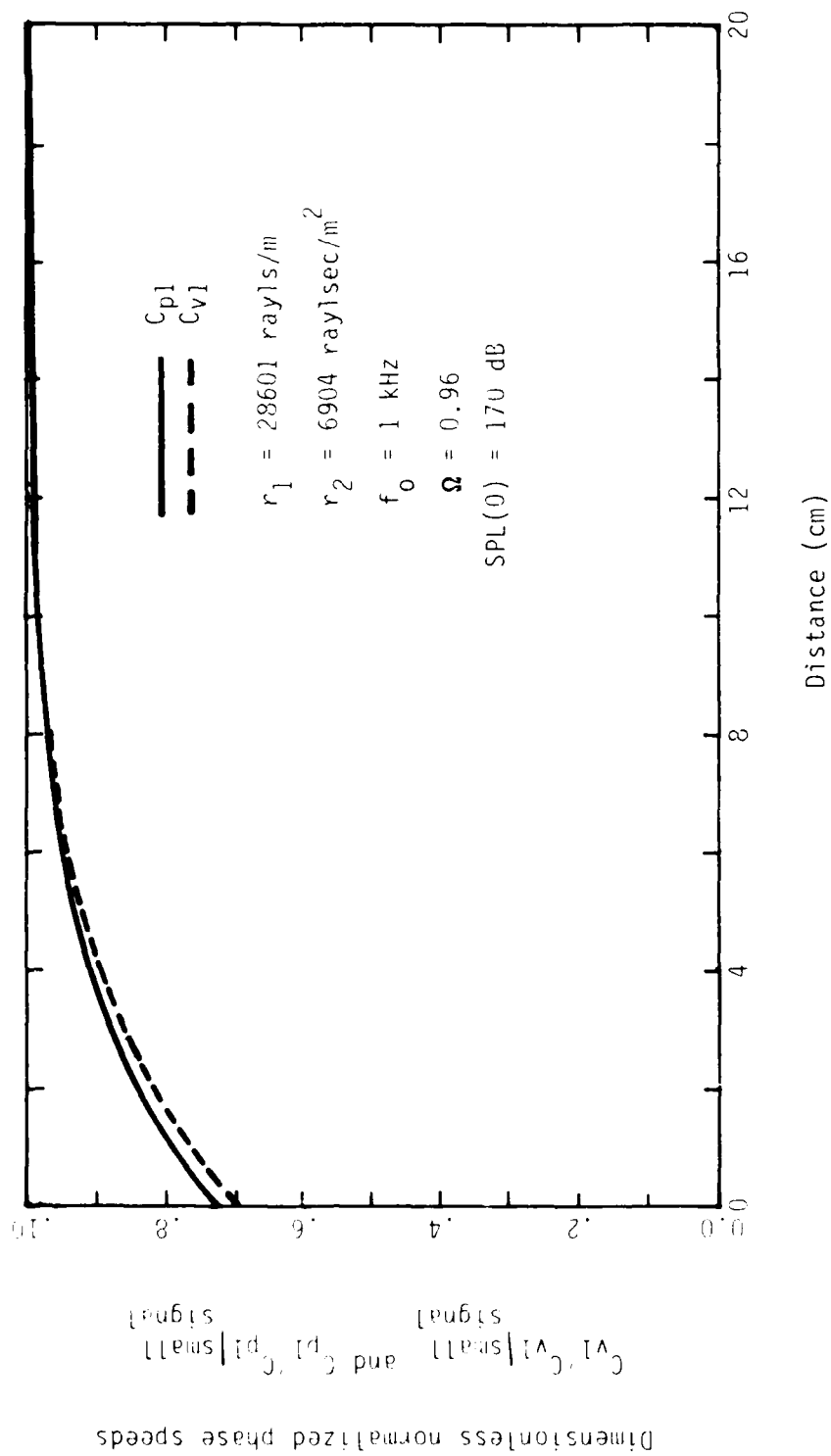
Figure 3-10

Dimensionless normalized phase speeds versus
distance for a finite-amplitude wave

$C_{v1}/C_{v1}|_{small}$ and $C_{p1}/C_{p1}|_{small}$ signal

Dimensionless normalized phase speeds

58

PLUGS (3)

0 375 DIA.
0 25 DIA.

MICROPHONE HOLDERS (2)

0 625 RUBBER GASKET

0 250 HOLES (3)

PLUGS (13)

0 375 DIA.
0 25 DIA.

0.25 WIDE BY 0 06 DEEP
EPOXY-FILLED SLOT WITH
8 HOLES FOR 0008 PIANO WIRE

2 25 ALUMINUM HEXAGONAL STOCK

105 SQUARE HOLE,
1/4 RADIUS CORNERS

3/16-32 THREAD

0 625 RUBBER GASKET

75° TAPER

SECTION A-A

0.75 HOLE

188 DIA.

ACOUSTIC DRIVER/WAVE TUBE ADAPTOR

REFERENCE FOR SPACING 13, 0.25" HOLES AT DISTANCES
OF: 1, 2, 3, 4, 5, 8, 11, 15, 20, 25, 30, 35, 40 cm (±0 02 cm)

SECTION B-B

TRAVELING WAVE TUBE

(UNLESS NOTED, ALL DIMENSIONS
IN INCHES)

Figure 4-1

Drawings of the traveling wave tube, acoustics
driver adaptor, and accessories

72

AS-85-576

## B. Experimental Apparatus

This section is divided into discussions of the traveling wave tube, the dc flow test apparatus, and the acoustic test apparatus. Since the traveling wave tube is common to all experiments, it is discussed first, followed by a discussion of the dc flow apparatus and of the acoustic test equipment.

The traveling wave tube is the central piece of equipment for all the experiments. The sample fills the tube and is held in place by friction with the walls. The tube provides for measurement of acoustic and static flows in the sample. The length of the tube is 26 in., the inside cross-section is 3/4 in. on a side, and the wall thickness is 1/8 in. A screen of 0.008 in. steel piano wire restrains the sample just inside what we call the downstream end of the tube. A series of ¼ in. diam. holes are drilled in the top side of the tube to serve as microphone ports. Engineering drawings of the tube are presented in Fig. 4-1 for the convenience of the reader (reproduced from Kuntz's dissertation by his kind permission).

### 2. dc Flow Apparatus

The dc flow apparatus measures the pressure drop across a porous sample as a function of flow speed. The traveling wave tube was originally designed for acoustical measurements, not for high pressure dc flow tests, so the tube had to be modified to accept a static flow input and to prevent leakage from the microphone holes. An adapter, fabricated from a block of hexagonal aluminum stock, is affixed at the upstream end of the tube to provide attachment points for the incoming flow and for the pressure gages. The adapter is clamped to the tube and a gasket guarantees a tight seal. A strip of rubber gasket material backed with aluminum is clamped on top of the tube to seal the microphone holes. These modifications were quite effective; at no time was the tube observed to leak.

71

1)     the dc and ac flow resistivities are the same, and

2)     the dominant nonlinear mechanism is a speed dependent resistivity

of the form $r = r_1 + r_2 u \, \text{sgn}(u)$.

The ac resistivity inferred from the small-signal attenuation data is compared with the dc resistivity to test the former assumption, and the qualitative agreement of the harmonic data and predictions is taken as an indication of the validity of the latter assumption. Data from the phase velocity test provides, for comparison with the prediction of Eq. (3.35), that a high intensity tone propagates more slowly than a small-signal wave of the same frequency.

The static flow and acoustic tests previously performed by Kuntz used a separate apparatus for each test type. Hence the static flow and acoustic measurements were performed on different samples. Since it is very difficult to create samples with identical properties, one is led to wonder about the compatability of the two data sets. We have therefore modified Kuntz's traveling wave tube to accommodate both the acoustic and static flow experiments. Experimental results indicate that the key assumptions stated above are at least qualitatively valid.

The remainder of Chapter 4 is divided into four parts. Section B contains a discussion of the equipment used in the experiments. Experimental procedure is detailed in Section C. Finally, the experimental data and theoretical predictions are compared in Section D. Section E is a summary of the experimental work and the conclusions drawn therefrom.

CHAPTER 4

EXPERIMENTAL WORK

A. Introduction

Three experiments have been performed to measure the effects of a
porous material on static flows and acoustic signals. Comparison of measured data
to theoretical predictions provides an indication of the validity of the theory. We
discuss the experiments in the following order:[†]

1)    static measurement of flow resistance,

2)    propagation measurements at high and low intensity,

3)    phase speed measurements.

In the first we measure the pressure drop across a length of bulk porous material for
various dc flow rates, from which we determine the resistivity of the sample as a
function of flow speed. The second experiment comprises measurements of the
harmonic sound pressure levels at various ranges. In the third test we determine the
phase speed from the relative phase of the fundamental between two points. The
latter two experiments are referred to here as the acoustic tests.

The dc data and the acoustic data serve different purposes. By fitting
Eq. (2.9) to the dc flow resistivity data for a given sample, we determine the
constants $r_1$ and $r_2$. These constants are treated as properties of the medium and
serve as input parameters for the numerical and analytical solutions. The
experiments are intended to confirm or refute two of our key assumptions, namely:

---

[†]The actual chronological order is discussed in Section C of this chapter.
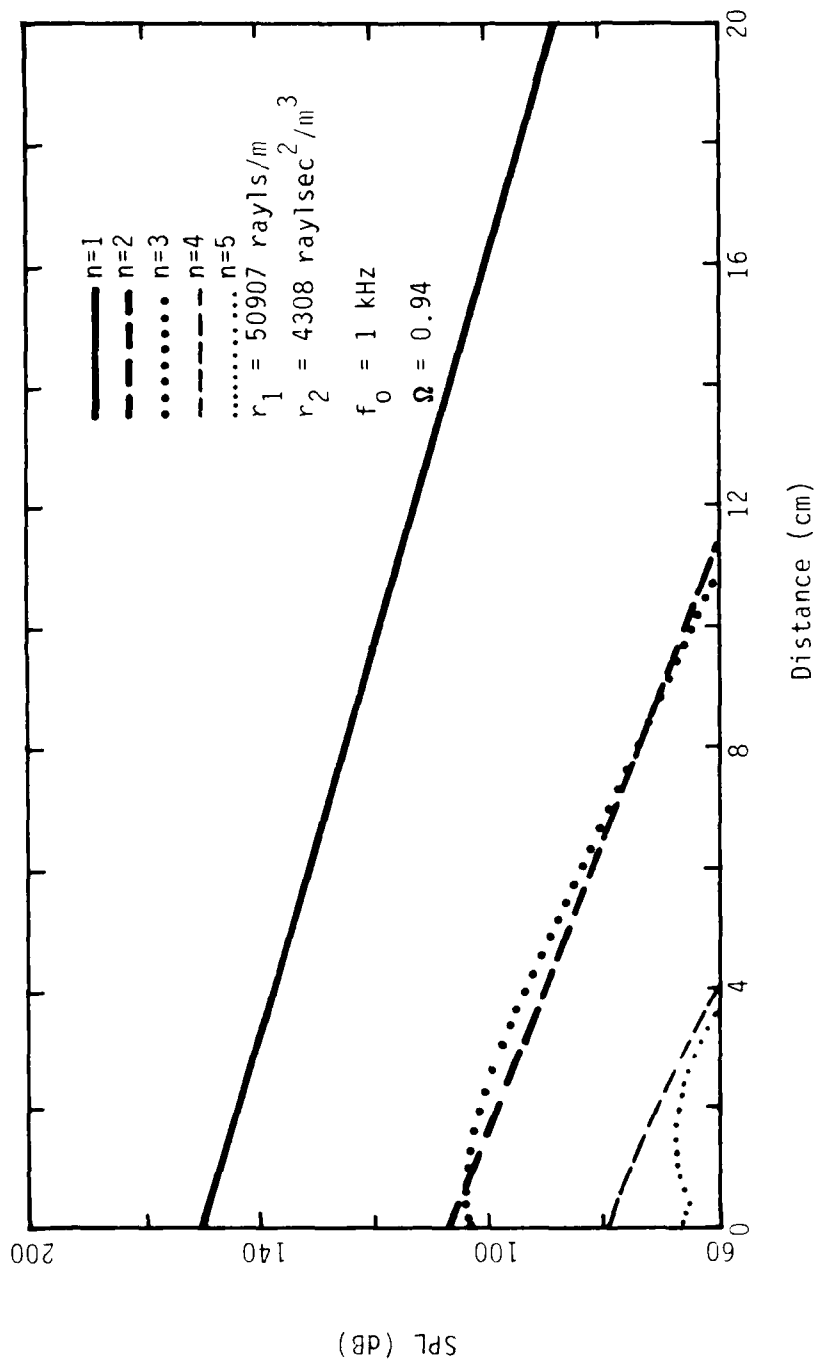
Figure 3-13

Predicted propagation curves for a
distorted sinusoid, $r = r_1 + r_2 u^2$

n=1
n=2
n=3
n=4
n=5

$r_1 = 50907$ rayls/m
$r_2 = 4308$ raylsec$^2$/m$^3$

$f_0 = 1$ kHz

$\Omega = 0.94$

Distance (cm)

SPL (dB)

The computer program for the numerical solution is easily reconfigured to accommodate the cubic nonlinearity. The modified program was run starting with the same initial levels used to produce the curves in Fig. 3-12. The predicted behavior for cubic nonlinearity, shown in Fig. 3-13, is qualitatively very much like that for the $v^2\text{sgn}(v)$ nonlinearity. This should come as no surprise, since the resistivity curves r(u) for the two models are designed to mimic the same set of resistivity data. Although the u sgn(u) model gave a better fit to the resistivity data, the quantitative results are not that much different here. Moreover, when compared to the measured acoustic data the differences between the two solutions are smaller than the approximation errors inherent in the solution (see Chapter 4 and Appendix B). We are therefore led to believe that a cubic nonlinearity may be substituted for the $v^2\text{sgn}(v)$ nonlinearity. This approach will be of considerable usefulness for a planned perturbation solution of a high intensity sound field in a lined duct.

Analytical solutions of Eq. (3.54) for the finite-amplitude tone case are very similar to their counterparts based on Eq. (3.29), and are given in Appendix B.

We have acquired basic understanding of the harmonic distortion caused by nonlinear resistivity. The numerical solution, which is based on an approximate first integral of Eq. (2.26), provides quantitative predictions for the cases of initially pure tones and distorted sinusoids. The fundamentals of the distorted sinusoids are shown to behave like the tones discussed in Section D, and the growth of harmonics is in a cubic distortion pattern. In Chapter 4 we compare the numerical solution results with measured data. Details of the computer program used to implement the solution are discussed in Appendix C.
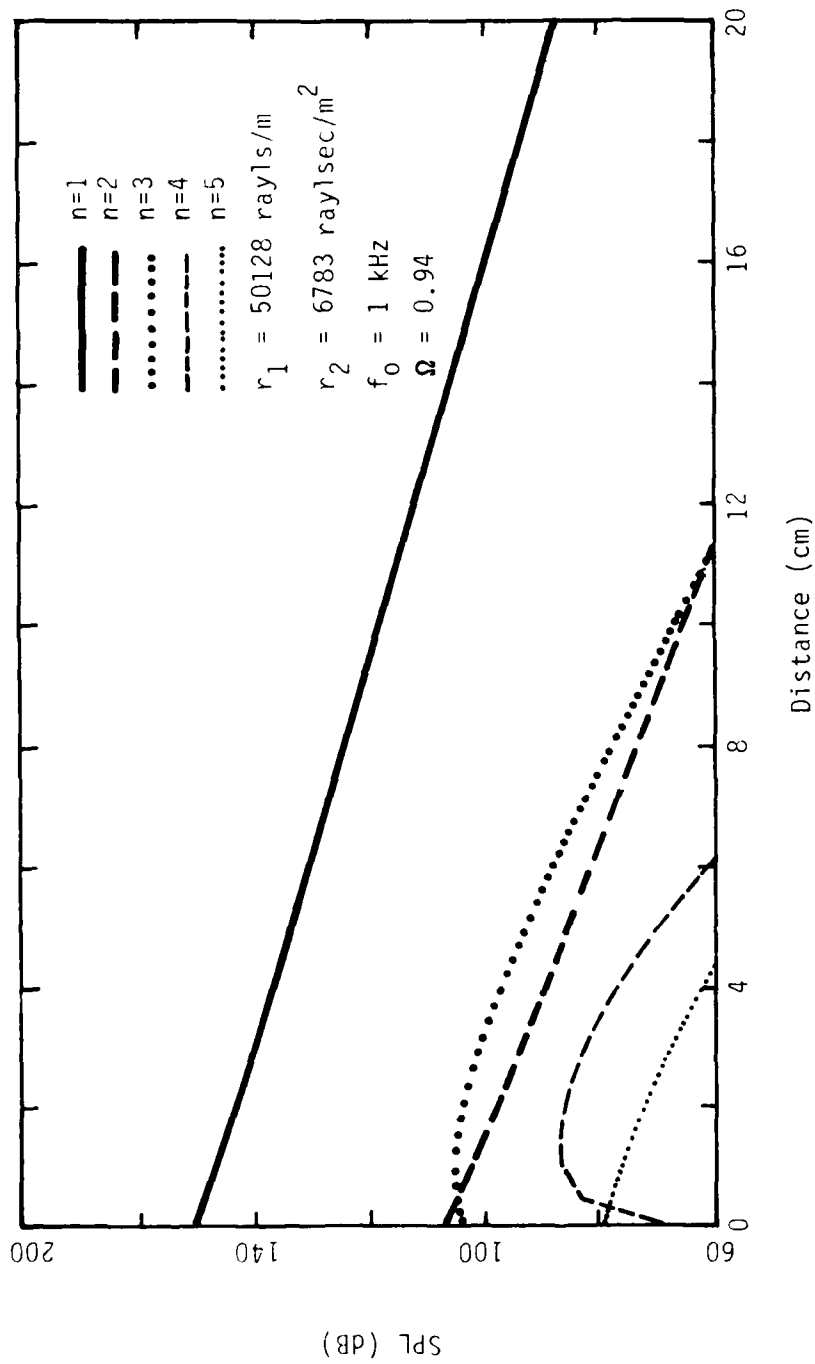
Figure 3-12

Predicted propagation curves for distorted
sinusoid, $r = r_1 + r_2 \, u \, \text{sgn}(u)$

SPL (dB)

Distance (cm)

n=1
n=2
n=3
n=4
n=5

$r_1 = 50128 \ \text{rayls/m}$

$r_2 = 6783 \ \text{raylsec/m}^2$

$f_0 = 1 \ \text{kHz}$

$\Omega = 0.94$

AS-85-574

energy is dissipated). The second harmonic is less strong than the fundamental but, because a negligible amount of energy reaches it from the fundamental, it too functions as a primary. Most of its energy is lost to augmented resistivity and in so doing it energizes the higher even harmonics. In fact, a second harmonic independently undergoing cubic distortion would energize the sixth, tenth, and fourteenth harmonics, and so on. It is therefore of interest to note that the fourth harmonic and its multiples are not members of the second harmonic cubic distortion product group. They are products of coupling between the primaries as represented by the forcing function $V_2 W_2$ which relies heavily on the fundamental strength through the factor $W_2$. Figure 3-12 shows the first five numerically calculated propagation curves for a distorted sinusoid. The initial harmonic levels are those of an actual measured signal.

### 3. Cubic Nonlinearity

All of the aforementioned distortion spectra could be explained equally well in terms of a cubic nonlinearity, i.e., the nonlinearity which results from use of the quadratic resistivity form

$$r = r_1 + r_3 u^2 \quad .$$

In this case, the corresponding form of Eq. (3.29) is

$$V'_n + j q_n V_n = \frac{-n \Omega R_3}{2 q_n} \sum_p \sum_q V_p V_q V_{n-p-q} \quad . \tag{3.54}$$

Analysis of the convolution term reveals that a pure tone input produces odd harmonic distortion products. Indeed, the "cubic" distortion pattern was named after the effects of just such a nonlinearity. This pattern leads us to suspect that other results for cubic distortion are similar to those for $v^2 \text{sgn}(v)$ distortion.

## 2. Propagation of Distorted Sinusoids

We now consider the case of propagation of distorted sinusoids like those used in our experiment. These signals are characterized by a strong fundamental accompanied by both odd and even harmonics which decrease in amplitude with increasing harmonic number. Although it is difficult to demonstrate analytically, it turns out that the addition of even harmonics to the signal has the effect of causing odd harmonics to appear in the rectified signal spectrum. We can make predictions of the harmonic propagation curve shapes by examining the differential equations governing the first four harmonics,

$$V'_1 + jq_1 V_1$$
$$- \frac{\Omega R_2}{2q_1} (V_1 W_0 + V_1^* W_2 + V_2 W_1^* + V_2^* W_3 + V_3 W_2^* + V_3^* W_4 + \ldots) \; ; \; V_1(0) = V_{10} \; , \qquad (3.53a)$$

$$V'_2 + jq_2 V_2$$
$$- \frac{2\Omega R_2}{2q_2} (V_2 W_0 + V_2^* W_4 + V_1 W_1 + V_1^* W_3 + V_4 W_2^* + V_4^* W_6 + \ldots) \; ; \; V_2(0) = V_{20} \; , \qquad (3.53b)$$

$$V'_3 + jq_3 V_3 = \frac{-3\Omega R_2}{2q_3} (V_1 W_2 + V_1^* W_4 + V_3 W_0 + V_5^* W_6 + \ldots) \; ; \; V_3(0) = V_{30} \; , \qquad (3.53c)$$

and

$$V'_4 + jq_4 V_4 = \frac{-4\Omega R_2}{2q_4} (V_2 W_2 + V_2^* W_6 + V_1 W_3 + V_1^* W_5 + \ldots) \; ; \; V_4(0) = V_{40} \; . \qquad (3.53d)$$

Again, only the most prominent forcing functions have been listed.

The fundamental is the strongest component in the signal. It is subject to excess losses because of the augmented resistivity, but some of its lost energy is upshifted in frequency and strengthens the family of odd harmonics (the rest of the
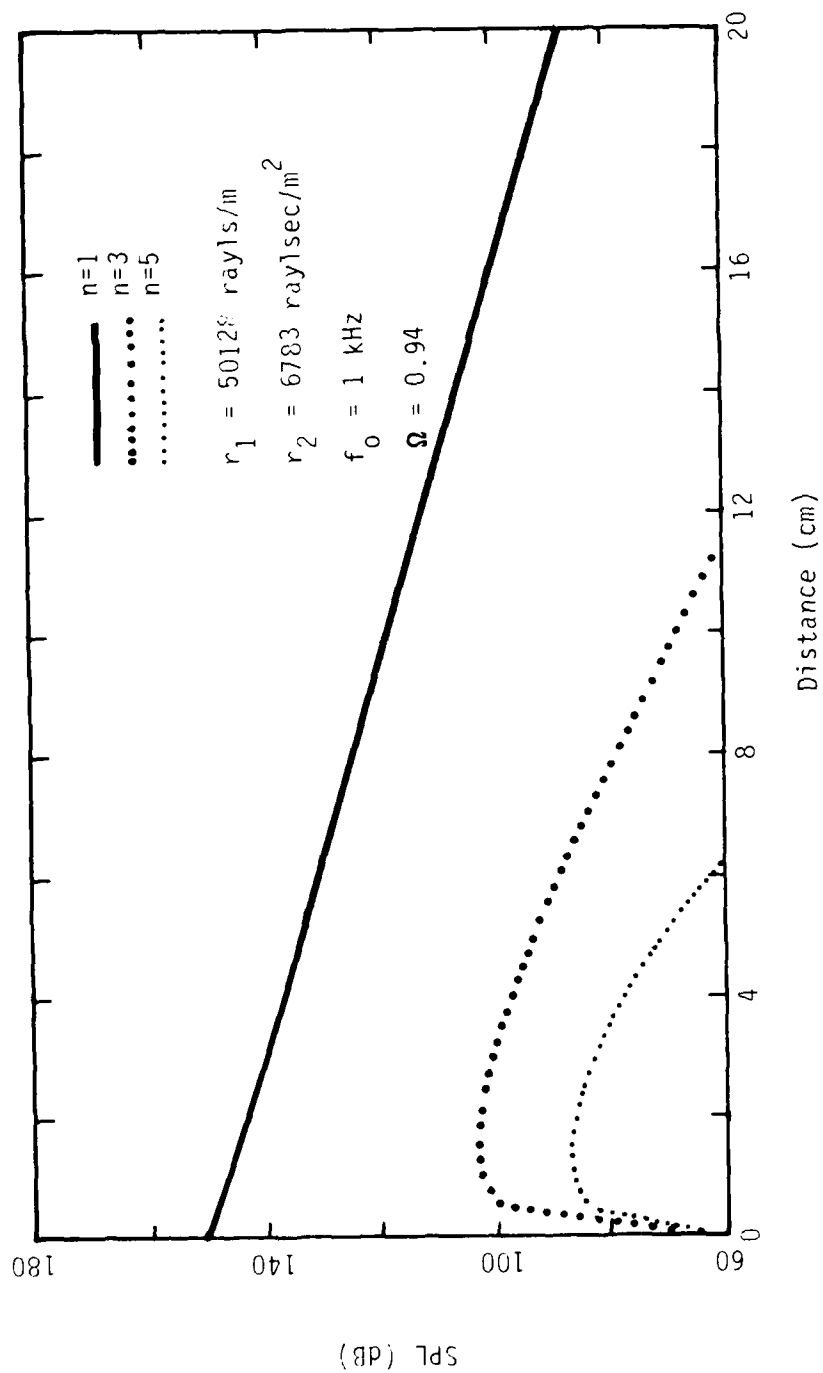
Figure 3-11

Predicted propagation curves for an
initially pure finite-amplitude tone

63

For the pure tone case, it is rather easy to recognize the primary and the distortion products. The differential equations governing the first four harmonics are

$$V'_1 + jq_1 V_1 = -\frac{\Omega R_2}{2q_1}(V_1 W_0 + V_1^* W_2 + V_3 W_2^* + V_3^* W_4 + \ldots) \quad ; \quad V_1(0) = V_{10} \quad , \quad (3.52a)$$

$$V'_2 + jq_2 V_2 = 0 \quad ; \quad V_2(0) = 0 \quad , \quad (3.52b)$$

$$V'_3 + jq_3 V_3 = -\frac{-3\Omega R_2}{2q_3}(V_1 W_2 + V_1^* W_4 + V_3 W_0 + V_3^* W_6 + \ldots) \quad ; \quad V_3(0) = 0 \quad , \quad (3.52c)$$

and

$$V'_4 + jq_4 V_4 = 0 \quad ; \quad V_4(0) = 0 \quad . \quad (3.52d)$$

The fundamental can be identified as a primary by the term $R_2 V_1 W_0$ on the right-hand side of Eq. (3.52a). The equations for the even harmonics are homogeneous. Because the initial values for these equations are zero, the even harmonics stay at zero amplitude for all distances. The odd harmonics, however, are vigorously energized by the fundamental as shown by the presence of forcing terms containing $V_1$ and $V_1^*$. Because their initial amplitude is zero, the odd harmonics are expected to have the characteristic rainbow shape. Figure 3-11 is a graph of the propagation curves for an initially pure tone. It is not possible to compare these predictions with data because we were not able to produce a true pure tone at high intensity in a porous material. This example is, however, very useful for helping us understand the distortion of more complicated signals.

$$\frac{d}{dx} |V_n| + q_{ni} |V_n| \leq 0 \quad , \qquad (3.49)$$

which implies that the attenuation rate exceeds that for a small-signal wave $q_{ni}$. Other harmonics are net receivers of energy. They are called distortion products, and are characterized by the relation

$$\frac{d}{dx} |V_n| + q_{ni} |V_n| \geq 0 \quad . \qquad (3.50)$$

Occasionally a distortion product receives such a rapid influx of energy that the harmonic amplitude initially increases with distance,

$$\frac{d}{dx} |V_n| \geq 0 \quad . \qquad (3.51)$$

The harmonic amplitude does not increase indefinitely, however. As the primary decays the loss mechanisms soon overtake the energy influx. In this case the corresponding propagation curve takes on a characteristic rainbow shape.

### 1. Propagation and Distortion of an Initially Pure Tone

The case at hand is that of an initially pure tone, for which the rectified spectrum has been shown (see Eq. (3.32)) to consist entirely of even harmonics. In the case of a pure tone, the resistivity varies in time at even multiple frequencies of the fundamental. As a result, odd harmonic distortion products are introduced into the signal. Despite their introduction, it turns out that the $W_n$ spectrum retains its even harmonic character. An initially pure tone is therefore expected to acquire only odd harmonic distortion components. This pattern is commonly referred to as cubic distortion.

61

particular, we are interested in the solutions for a distorted sinusoid like those used in our experiment. Closed form analytical solutions are not possible in the general case because the spectrum of the full wave rectified signal $(W_n)$ cannot be expressed as a direct function of the signal harmonics $V_n$. In addition, the full solution consists of a large number of interdependent individual solutions, one for each harmonic in the signal. For these reasons the general case is best solved by computation. Nevertheless, qualitative predictions can be made by inspection of Eq. (3.29).

A single initial value for each harmonic is required to solve Eq. (3.29), namely $V_n(0)$. The values of $V_n(0)$ are easily determined from the available data for $P_n(0)$ by means of an approximate impedance relation that we now derive. The continuity equation, Eq. (3.10), relates $P_n$ and $V_n'$, and the first integral Eq. (3.29) relates $V_n'$ and $V_n$. These relations are combined to give an approximate impedance relation

$$\frac{\hat{P}_n}{V_n} = \frac{q_n}{n} - j \frac{\Omega R_2}{2q_n} \sum_p \frac{V_p W_{n-p}}{V_n} \quad , \tag{3.48}$$

Since the distortion spectrum $\sum_p V_p W_{n-p}$ depends on the signal spectrum $V_n$, we determine $V_n(0)$ by successive approximation. Minute approximation errors are no longer a cause for concern, since the possibility of spurious wave solutions has been eliminated; the single initial value per harmonic is sufficient to fully specify a stable solution.

The velocity dependent resistivity causes energy to be exchanged between the various harmonics of the signal. Two basic but loosely defined classes of harmonics arise: primaries and distortion products. Primaries are net suppliers of energy to other harmonics. They are characterized by the relation

60

3) The impedance magnitude and reactance increase with amplitude.

4) The phase velocities of the pressure and particle velocity signals differ. The difference is due to the dependence of the reactance of the material on amplitude.

Since the wave decays as it travels, the attenuation, impedance, and phase velocity eventually revert to their small-signal values.

It is clear that small-signal resistivity effects are augmented at high amplitude, that is, the higher amplitude wave encounters a larger resistivity. The increased resistivity can be demonstrated by direct calculation. We consider a nondimensionalized version of Eq. (2.9),

$$R = R_1 + R_2 \, w(x, \tau) \quad . \tag{3.46}$$

The average value of the resistivity over a cycle of the tone is simply

$$\langle R \rangle = R_1 + R_2 \, W_o(x) \quad . \tag{3.47}$$

This result demonstrates a local increase in the mean resistivity because of the passage of the wave.

The reader should note, however, that the resistivity actually fluctuates in time because of the acoustic signal, as defined in Eq. (3.46). Time-varying properties of the medium signify that new harmonic components are produced by the interaction of the signal and the fluctuating resistivity. In the next section we expand the analysis to include the harmonic distortion products as well.

## E. Numerical Solution for Initially Pure Tones and Distorted Sinusoids

The purpose of the numerical solution is to generate theoretical predictions for comparison with actual signals. We must therefore extend the solutions of the inhomogeneous Helmholtz equation to include the harmonics of the signal. In

59

The apparatus is best understood if the flow is followed from source to outlet (see the block diagram in Fig. 4-2). A regulated 100 psi air supply drives the flow. The flow rate $F_r$ in standard cubic feet per hour (SCFH) is measured by one of a collection of flowmeters which cover various ranges. The flow then enters the tube at the adapter, passes through the sample, and exhausts into the atmosphere at the left end of the tube. The gage pressure in inches of water (in. $H_2O$) at the adapter block is measured by a series of pressure gages. Since the gage and tube share the same outlet pressure, the gage reading indicates the pressure drop across the sample $\Delta p$. The resistivity is

$$r = \frac{\Delta p\, A}{F_r\, L} \quad ,$$

where L is the length of the sample and A is the cross-sectional area of the tube.

### 3. ac Test Apparatus

The ac test apparatus permits measurement of harmonic SPLs and relative phase of the fundamental at six down range positions. Six microphones were used in the experiment so that they would not have to be moved repeatedly. The only drawback to this approach is that the signals from the microphones must be adjusted so that the microphones respond equally to a given input. The microphone nearest the source is called the reference microphone; the harmonic spectrum measured at this position provides the boundary conditions for the numerical calculation. Phase angle measurements are referred to the signal at this microphone as well. The ac apparatus includes some rather elaborate electronics; the reader is encouraged to make use of the block diagram provided in Fig. 4-3. Four distinct sections of the apparatus are identified:

73
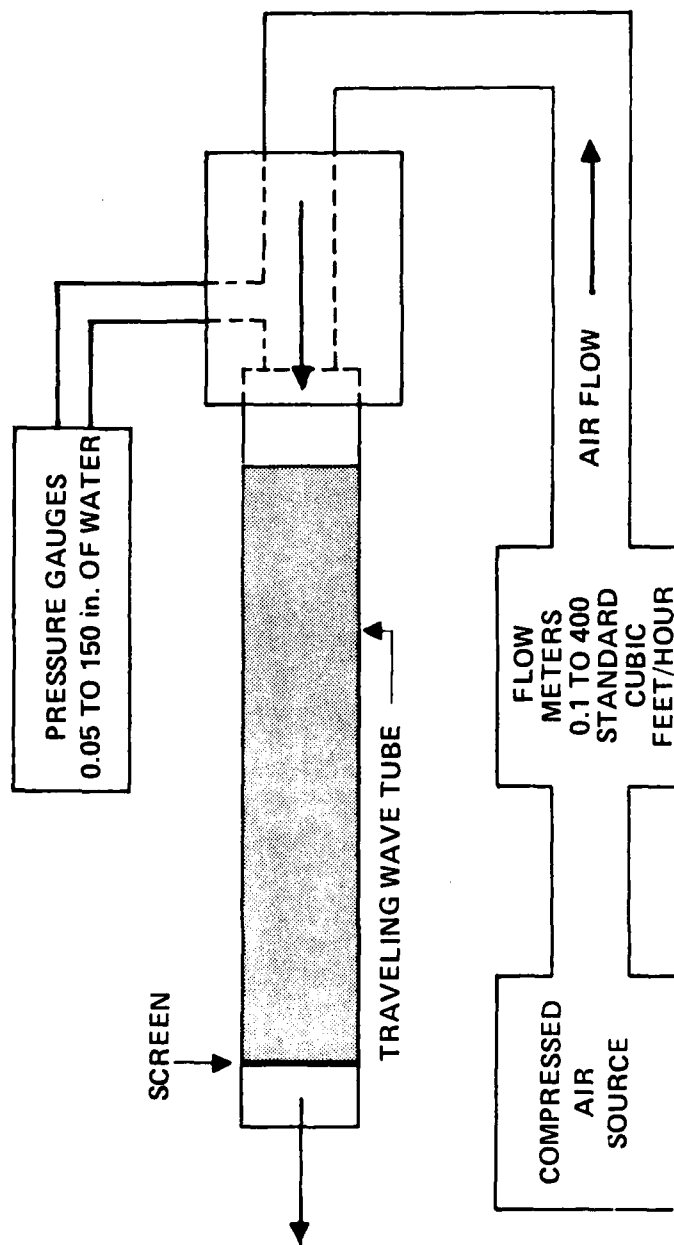
FIGURE 4-2
BLOCK DIAGRAM OF DC FLOW RESISTIVITY MEASUREMENT APPARATUS

PRESSURE GAUGES
0.05 TO 150 in. OF WATER

TRAVELING WAVE TUBE

SCREEN

FLOW
METERS
0.1 TO 400
STANDARD
CUBIC
FEET/HOUR

AIR FLOW

COMPRESSED
AIR
SOURCE
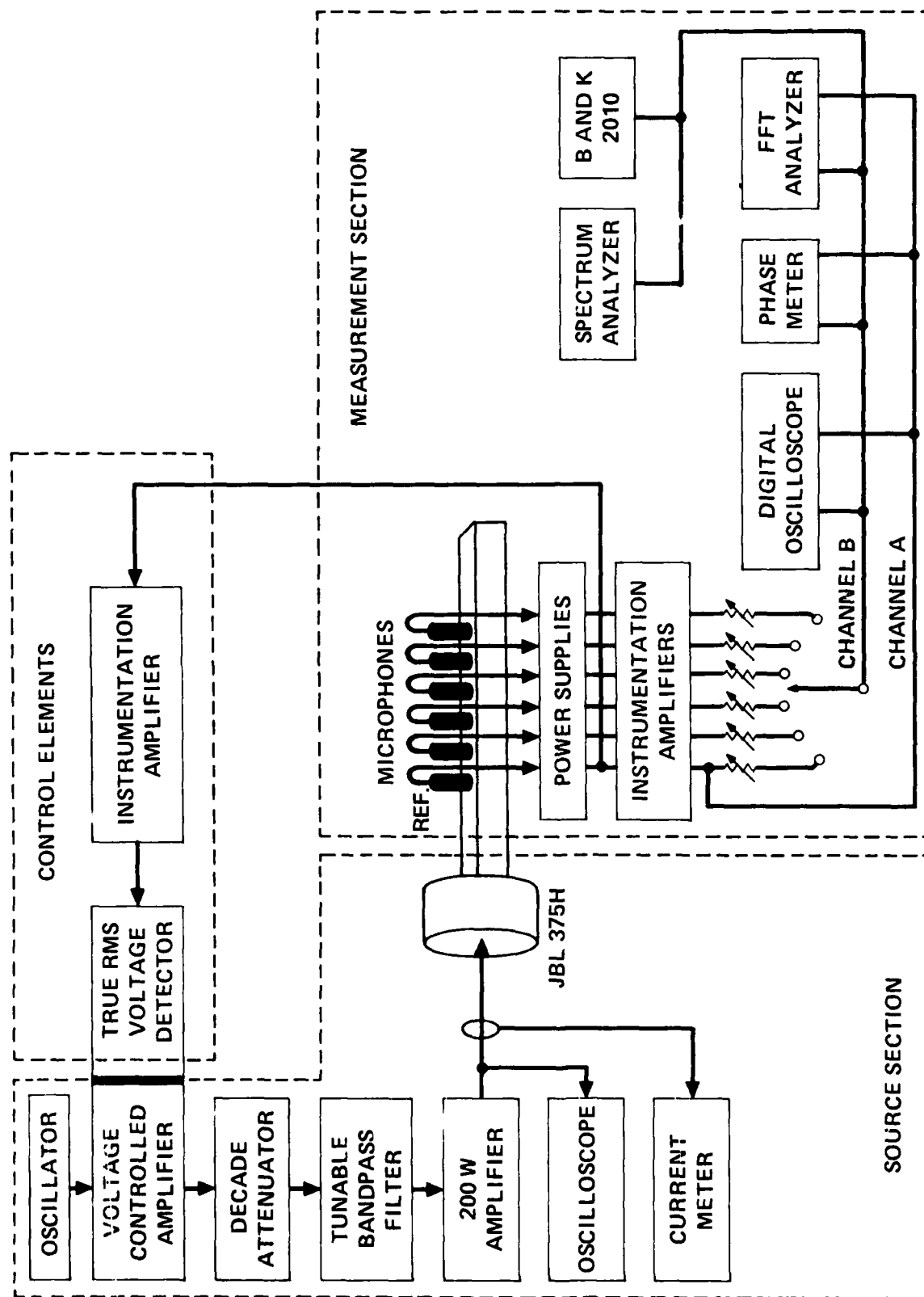
FIGURE 4-3
BLOCK DIAGRAM OF
ACOUSTIC MEASUREMENT APPARATUS

75

1)     the source section,

2)     the acoustical section,

3)     the measurement section, and

4)     the control elements.

They are discussed in this order.

The source section begins with the oscillator and ends with the compression driver.[†]  The oscillator produces a continuous pure tone which is appropriately amplified or attenuated by the voltage controlled amplifier (VCA) section of the compressor.  The compressor is a control element and is discussed below. Since signal distortion is introduced by the VCA, a high-Q bandpass filter tuned to the fundamental signal frequency is inserted in the circuit to remove unwanted harmonics.  It is desirable to have as pure a spectrum as possible at the reference microphone because the harmonic distortion effects are more apparent.  A decade attenuator compensates for the gain of the filter.  The source signal then passes to the DuKane 200W amplifier and on to the acoustic source, a JBL 375H compression driver with titanium diaphragm.  The power applied to the driver was kept below 25 W continuous rms which, for 8 $\Omega$ nominal impedance, corresponds to a current limit of 1.768 A as measured by the Keithley VOM.  The oscilloscope was used to visually warn the experimenter in the event of signal fluctuations or clipping.

The acoustic section of the experiment includes the tube, all associated hardware, and the sample itself.  The empty tube has a first cross-mode cut-on at about 9 kHz; frequencies used here are low enough that inadvertent modal excitation is not expected to be a factor in the measurements.  An adapter connects

---

[†]A compression driver is usually used to drive an acoustic horn.

the driver to the tube by means of a tapered bore which smooths the cross-sectional area difference. The microphones are placed in holders at the reference (0 cm), 2, 5, 8, 11 and 20 cm positions. In addition, the microphone holders grip the tube tightly. Thus, tube wall mass loading is provided, which reduces vibration of the holders. A narrow air gap is left between the microphone face and the sample to avoid noise caused by direct contact of the fibers with the microphone face. Finally, the porous sample serves as its own acoustic termination, since it provides small-signal attenuations in the hundreds of dB/m. The sample extends well beyond the 20 cm microphone position; no reflected waves are expected to be present within the sample near the microphones.

Although the source signal is originally sinusoidal, the signal received at the reference microphone is somewhat distorted at high intensity. Harmonics are added to the signal by a variety of nonlinear mechanisms, including transducer nonlinearity, propagation through the air, transmission through the material/air interface, and propagation through the material.

The measurement signal paths begin at each of the six microphones. Five Bruel and Kjaer model 4136 and one model 4135 microphone were used. The signals from the individual microphones pass to a rack of instrumentation amplifiers where the dc power supply voltages are removed and coarse microphone calibration is done. Fine calibration is performed with a separate set of potentiometers so that the microphones respond uniformly to the calibrated signal from a B&K pistonphone. A six-position rotary switch is used to select the output of one microphone channel at a time. The harmonic spectrum of the signal from the selected microphone is measured with either a B&K 2010 heterodyne analyzer or an HP 3580A spectrum analyzer.

In early phase tests the relative phase between unfiltered signals from the reference microphone and a selected microphone was measured using a Dranetz 305-PA-3009 phase meter. However, phase errors induced by the presence of harmonics in the signals complicated the measurement considerably. Consequently, later tests were performed using a Spectral Dynamics SD375 2-channel digital FFT spectrum analyzer which measured the transfer function between the two signals for a multitude of narrow passbands. Phase shifts of the fundamental component measured with the SD 375 are not subject to intrusion of harmonics and are therefore much more trustworthy.

The control elements exist so that the experimenter need not continuously monitor the source section of the experiment. A signal is tapped from the reference microphone channel and is returned to the control input of the compressor. The compressor senses the rms voltage of the signal at the control input, compares it with a voltage set by the operator, and automatically adjusts the VCA gain so that the reference microphone signal stays constant. The compressor therefore guarantees a stable SPL at the reference position.

## C. Experimental Procedure

The following is a description of a single segment of the experimental regimen as applied to an individual porous sample. A flowchart of the process is provided in Fig 4-4.

### 1. Preparation

Preparation for the experiments consumed nearly as much time as the experiment itself because the procedure of packing the tube was extremely tedious. We began by selecting one of three sample porosities, namely $\Omega = 0.94$, 0.96, or 0.98. A large number of 3/4 in. squares were cut out of sheets of batted Kevlar[R]29. The

**PREPARATION**

START

CHOOSE POROSITY

PACK TUBE

HOMOGENEITY TEST

FAIL

PASS

**SPL TESTS**

SET SPL

SET FUNDAMENTAL FREQUENCY

SELECT MICROPHONE

MEASURE $n^{th}$ HARMONIC SPL

$n + 1^{th}$ HARMONIC

NEXT MICROPHONE

NEXT FREQUENCY

NEXT SPL

**PHASE TESTS**

SET FREQUENCY

SET SPL

SELECT MICROPHONE

MEASURE MAGNITUDE AND PHASE OF TRANSFER FUNCTION

NEXT MICROPHONE

NEXT SPL

NEXT FREQUENCY

**STATIC FLOW RESISTIVITY MEASUREMENT**

MEASURE SAMPLE LENGTH

SET FLOW RATE

READ PRESSURE

MEASURE SAMPLE LENGTH (OPTIONAL)

INCREMENT FLOW RATE

END

**FIGURE 4-4**
**FLOWCHART OF EXPERIMENTAL PROCEDURE**

ARL:UT
AS-84-948-P
DN - GA
10 - 30 - 84

79

squares were originally ¼ in. thick and had a natural porosity of about 0.985. The squares were inserted one at a time a predetermined distance into the tube to create a sample having the desired porosity as defined by

$$\Omega = 1 - \frac{m}{\rho_{Kev} LA} \quad , \tag{4.1}$$

where m is the mass of the sample, L is the total sample length, $\rho_{Kev}$ is the density of solid Kevlar (1450 kg/m$^3$), and A is the cross-sectional area of the tube. The natural spring of the Kevlar resists packing, but friction with the tube walls holds it in place. Once the packing was completed the microphone holders and driver adapter were affixed to the tube.

The homogeneity of the sample was tested by measuring the small-signal attenuation in the material at each of the microphone positions. With the source adjusted for a 100 dB SPL tone at 1 kHz at the reference microphone, the SPL at each of the microphone positions was measured. If the SPL differences between the signals at the 2, 5, 8 and 11 cm positions covered a range of more than 1 dB, the sample was pronounced inhomogeneous and rejected. In this case the hapless experimenter discarded the sample and repacked the tube. Otherwise, the propagation tests could begin.

## 2. Propagation Experiment

The sound pressure levels of the signal harmonics at each of the six microphone positions were measured for all possible combinations of the following frequencies and reference microphone fundamental SPLs: 500, 1000, and 1500 Hz, and 100, 120, 140, 150, and 160 dB. It was not necessary to perform all combinations of microphone position, frequency, and SPL for the phase test.

Microphone selection was limited to the reference and the 8 cm and 11 cm microphones because the changes in phase at high intensity were cumulative and were not fully developed at earlier microphone positions; at the 20 cm position the signal-to-noise ratio was usually too low to obtain stable phase readings. A full complement of reference SPLs was used, however, since the nonlinearly induced phase shifts tended to appear rather suddenly. Once the phase test was completed the microphones, microphone holders, and driver adapter were removed and the tube was reconfigured for the dc test.

The accuracy of our measurements was potentially quite good. The B&K 2010 is highly accurate and can be read to within ±0.2 dB. Digital sampling errors in the Spectral Dynamics analyzer give errors of ±0.2 dB and about $0.5^\circ$ in phase. The HP spectrum analyzer, which was not designed for such exacting tasks, can be read to an accuracy of ±1 dB. The high level of accuracy is in reality unnecessary: inhomogeneities in the sample cause readings to deviate from simple small-signal attenuation by up to ±.5 dB .[†] Since the theoretical predictions assume a homogeneous material, the inhomogeneities are the limiting factor for the applicability of the data.

### 3. dc Test

The dc test was performed last for one reason: the sample usually compresses during the test, and the final porosity was unpredictable. Moreover, the sample can compress so far that it ceases to function as a termination. In extreme cases, the sample may recede beyond the last microphone.

---

[†]Samples with larger deviations are rejected.

The test itself was quite simple. The flow rate was increased in steps that would be roughly equidistant on a log u plot. A large number of measurements were clustered at low flow velocities to ensure a good estimate of $r_1$. As the flow rate was increased, care was taken to stay within the operating ranges of the flowmeters and pressure gages. The adapter block was occasionally removed for measurement of the sample length so that the compression effects could be accounted for at a later time. The experiment was completed when the range of the available pressure gages and/or flowmeters was exceeded. The sample was then discarded and the tube repacked.

### 4. Compensation for Porosity Changes

The purpose of the static flow resistivity test is to determine the resistivity of a sample as a function of flow speed. Implicit in this statement is the understanding that the frame is rigid, i.e., $\Omega =$ constant. Unfortunately, because the static flow test operates far below the decoupling frequency, the material is compressed by the flow, i.e., the sample length L is dependent on the velocity as L(u). As the sample compresses, the porosity is reduced and the resistivity of the material changes. These compressions do not take place for signals which, as in our experiments, lie well above the decoupling frequency. The subject of this section is a method of compensating the resistivity measurement for sample compression.

The velocity dependent porosity $\Omega(u)$ can be determined via Eq. (4.1) if the sample length L as a function of velocity is known. The sample length was measured for several velocities during the experiment, but the limited number of discrete data points obtained is hardly sufficient to define a function L(u). We therefore use the method of cubic T-splines as developed by Foreman[26] to generate an approximate curve from the discrete length data. The advantage of Foreman's method is that it

minimizes spurious curve "oscillations" and other inaccuracies caused by the inadequacy of a cubic polynomial fit.

In order to distinguish between resistivity changes due to sample compression and those due to the expected amplitude dependence, we develop a model which describes the changes in resistivity with velocity and porosity. Hersh and Walker have determined the functional dependence of the linear resistivity $r_1$ on porosity to be

$$r_1(\Omega) = \frac{\mu}{d^2 g} \left[ \frac{1 + g \sqrt{\frac{\pi}{4(1-\Omega)}}}{\left(\frac{\pi}{4(1-\Omega)}\right)^{3/2}} \right] \quad , \qquad (4.2)$$

where $\mu$ is the dynamic viscosity, d is the fiber diameter, and g is an empirically determined constant of the material. From our data we calculate the average value of g for batted Kevlar[R] 29 to be roughly 0.065. Kuntz's data[1] imply a value of about 0.062, and Hersh and Walker[13] reported a value of 0.059. We have used a compromise value of g=0.063 throughout these calculations. The nonlinear resistivity $r_2$ also changes with porosity, but its functional dependence has yet to be determined. We have observed, however, in Kuntz's data and our own, that the value of $r_2$ seems to be related to $r_1$ by a simple constant for a given material for a number of porosities. If we call this constant h, the resistivity can be determined from known values of $r_1, \Omega$, and h:

$$r(\Omega, u) = r_1(\Omega)\,(1 + h\,u) \quad .$$

A more general form, which favors neither Eq. (2.9) nor Eq. (2.10), is

$$r(\Omega, u) = r_1(\Omega)\,f(u) \quad , \qquad (4.3)$$

where the coefficients of the polynomial f(u) are porosity independent constants of the medium. For our experiment the porosity was a function of velocity $\Omega(u)$, so that our measured resistivity data is assumed to obey the relation

$$r_{meas.}(\Omega(u),u) = r_1(\Omega(u)) \, f(u) \quad . \tag{4.4}$$

If the sample had remained rigid, the data would have obeyed the relation

$$r(\Omega(0),u) = r_1(\Omega(0)) \, f(u) \quad , \tag{4.5}$$

where $\Omega(0)$ is the nominal porosity before any flow is applied. In order to adapt the data from a compressed sample to an ideally rigid one, the two relations are combined to eliminate f(u). The rigid sample data is therefore related to the measured data by

$$r\left(\Omega(0),u\right) = \frac{r_1\left(\Omega(0)\right)}{r_1\left(\Omega(u)\right)} \, r_{meas.}\left(\Omega(u),u\right) \quad . \tag{4.6}$$

Note that the explicit form of f(u) is unimportant here; it is sufficient merely to acknowledge its existence.

## D. Experimental Results and Comparison with Data

This section is the confluence of the theoretical work of Chapter 3 and the experimental work of Chapter 4. Here we examine the correspondence between theoretical predictions and the experimental observations. The dc resistivity data is discussed first, since the resistivity properties of the medium are needed as inputs for the predictions. The acoustic data is then discussed in the same order followed in the theoretical discussions of Chapter 3: propagation of small-signal waves, finite-amplitude tones, and finite-amplitude distorted sinusoids.

# 1. Resistivity

Resistivity data for six samples, adjusted for sample compression, were fitted to the u sgn(u) model, Eq. (2.9), and the $u^2$ model, Eq. (2.10), by the method of curvilinear regression. The quality of fit, as measured by the mean squared deviation of the data from the fitted curve consistently favored the u sgn(u) model (see Table B-1 in Appendix B). A plot of some typical resistivity versus flow velocity data is shown by the circles in Fig. 4-5 (see also Fig. 2-1). The data are somewhat scattered at low flow velocities because our equipment is less accurate for very small values of u and $\Delta p$. The calculated values of the constants $r_1$ and $r_2$ for the samples are shown in Table 4-1, along with the calculated values of the empirical constant g and the "relative nonlinearity" ratio $r_2 c_i / r_1$. The sample numbers were assigned in the order in which they were tested.

TABLE 4-1

Resistivity properties of porous samples

| Sample | $\Omega$ (nominal) | $r_1$ (mks rayl/m) | $r_2$ (rayl sec/m$^2$) | g | $r_2 c_i / r_1$ |
|---|---|---|---|---|---|
| 1 | 0.94 | 50233 | 6715 | 0.066 | 38.9 |
| 2 | 0.98 | 10437 | 3261 | 0.071 | 90.8 |
| 3 | 0.96 | 29789 | 6831 | 0.062 | 66.7 |
| 4 | 0.94 | 51539 | 12708 | 0.064 | 71.7 |
| 5 | 0.96 | 28601 | 6904 | 0.066 | 70.2 |
| 6 | 0.94 | 52891 | 11354 | 0.062 | 62.4 |
| 7 | 0.96 | 28784 | 6204 | 0.065 | 62.7 |

Resistivity r (kilorayls/m)

Flow velocity (m/sec)

● Data corrected for sample compression
▲ Raw data (uncorrected)

batted Kevlar 29
Sample #5
$\Omega = 0.96$
$r_1 = 28601$ rayls/m
$r_2 = 6904$ raylsec/m$^2$

$r = r_1 + r_2 u \, sgn(u)$
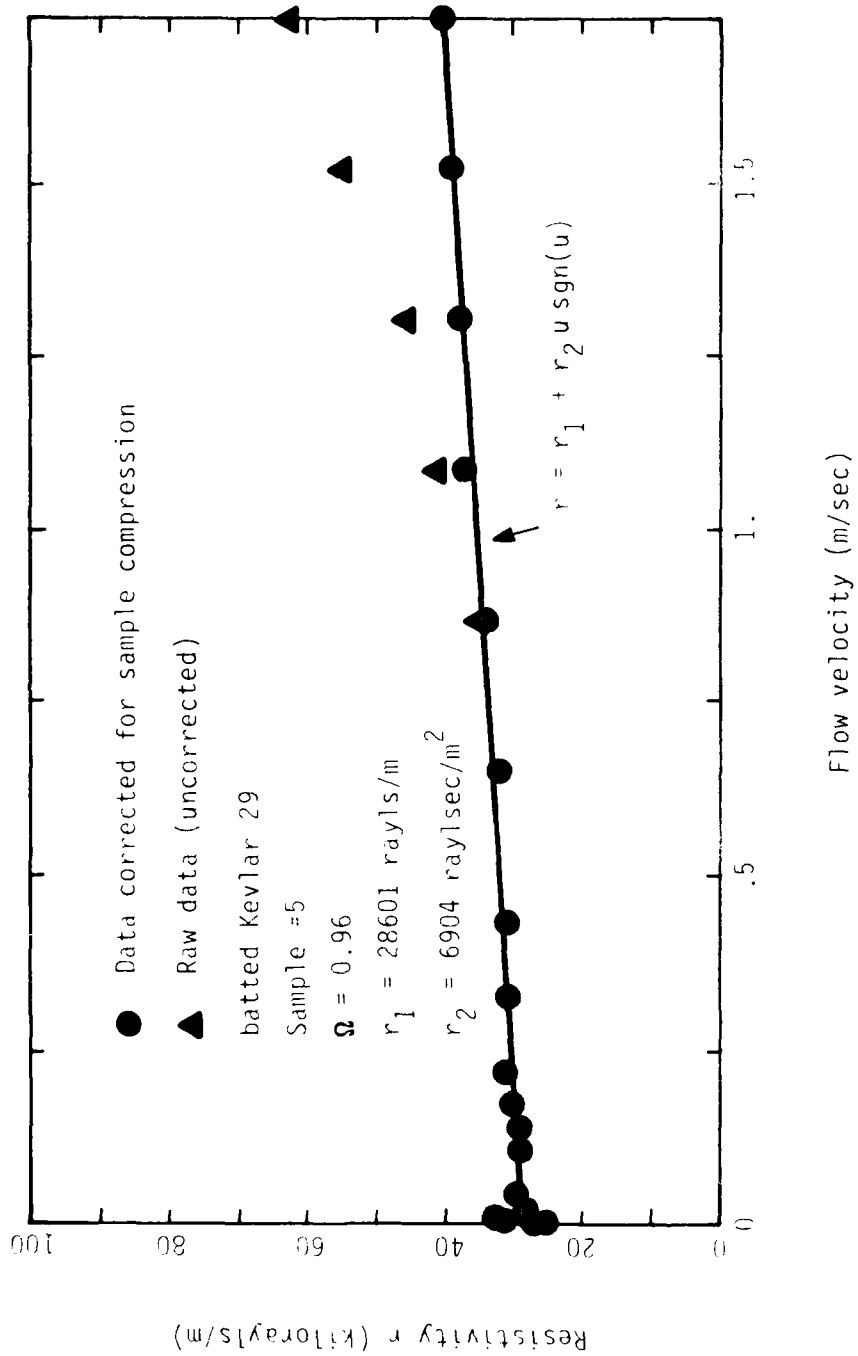
Figure 4-5

Measured static flow resistivity data and demonstration
of compression compensation algorithm

AS-85-578
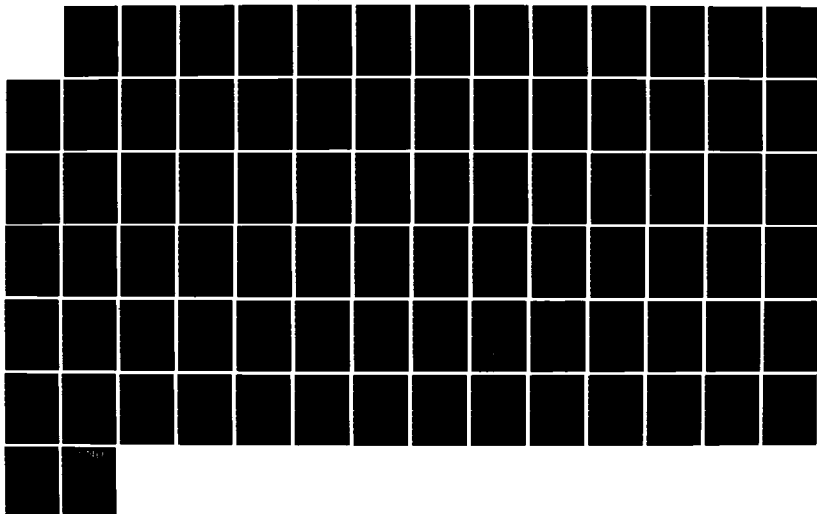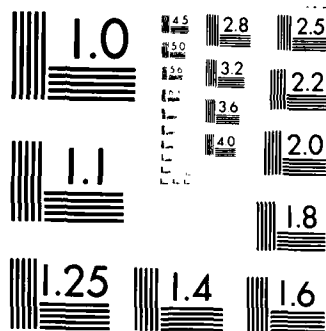
MICROCOPY RESOLUTION TEST CHART

NATIONAL BUREAU OF STANDARDS 1963 A

An illustration of the power of the compression compensation algorithm can be found in Fig. 4-5. The triangular symbols represent the raw data prior to correction for sample compression. The porosity of the sample remained constant at the value $\Omega = 0.96$ for flow rates below 1 m/sec. For higher flow rates, however, the sample compressed quite a bit: a flow rate of 1.73 m/sec reduced the porosity of this particular sample to $\Omega = 0.946$. The uncompensated resistivity datum at this flow velocity was actually 62,139 rayl/m before the algorithm reduced it by 35% to 40,538 rayl/m, where it falls right into line with the pattern set by the lesser flow rates. The remarkable consistency of the corrected points with those for which the sample was in fact rigid implies that the assumption underlying Eq. (4.3) is valid. Adjustments made to resistivity data were similarly successful for all samples for which there was adequate L(u) information, save one. The exception was sample 2 which, because of its very high porosity ($\Omega = 0.98$), compressed to about one third of its initial length. The cubic polynomial curve fit was simply insufficient to match the length data.

Five of the seven samples studied had very consistent properties. Sample 1, for no apparent reason, had a much lower relative nonlinearity than the others.

## 2. Small-Signal Tests

Attenuation and phase velocity predictions of Section 3.B were tested by measuring the change in SPL and phase of a propagating tone as a function of distance through the sample. The attenuation determined therefrom is plotted versus frequency and compared to predicted values in Fig. 4-6. The phase speed measurements and predictions are shown in Fig. 4-7. In both figures the solid lines represent predictions based on Eq. (3.23). The dashed line in Fig. 4-7 represents the isothermal sound speed value. Low frequency predictions agree well, but as the

87
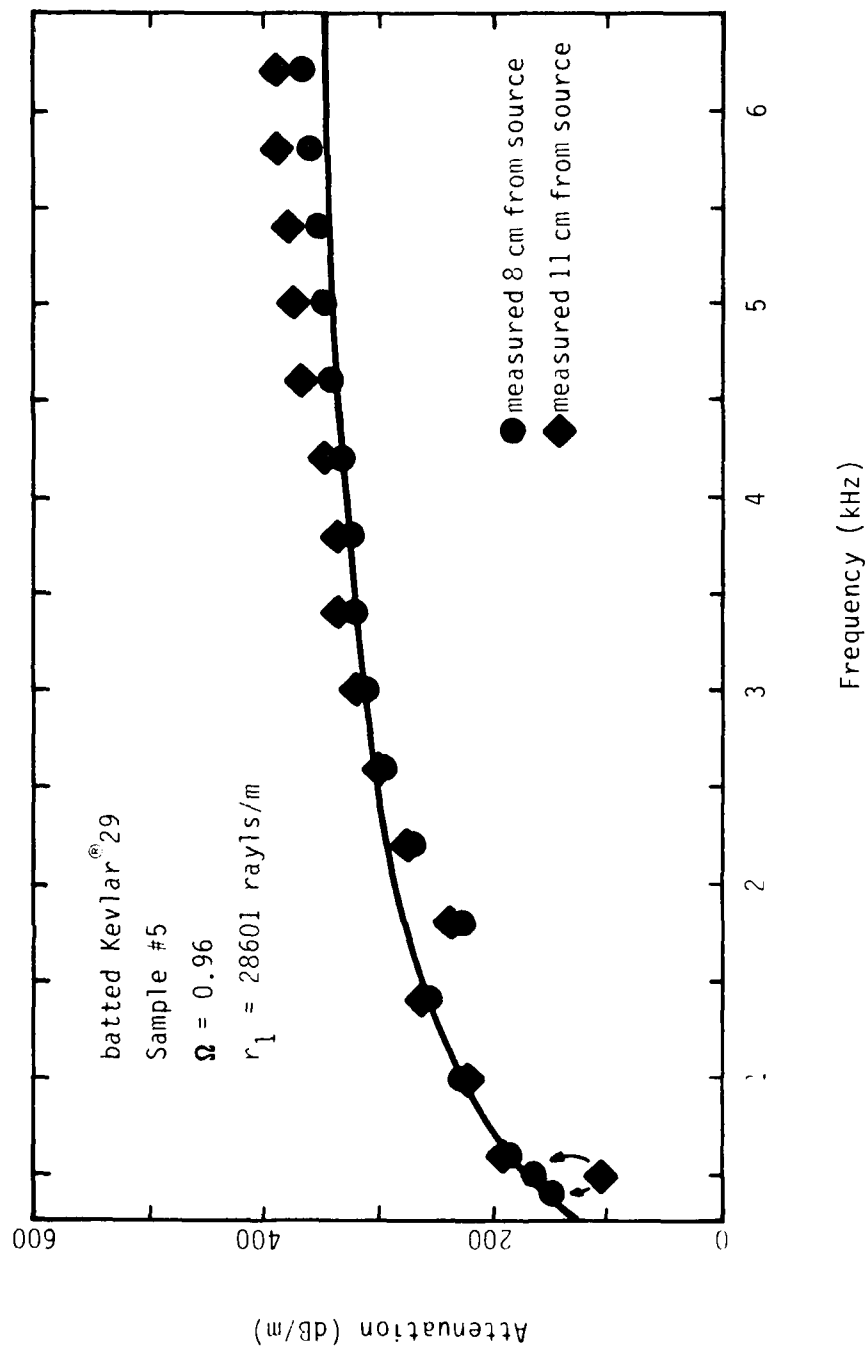
Figure 4-6

Comparison of measured and predicted
small-signal attenuation

AS-85-579
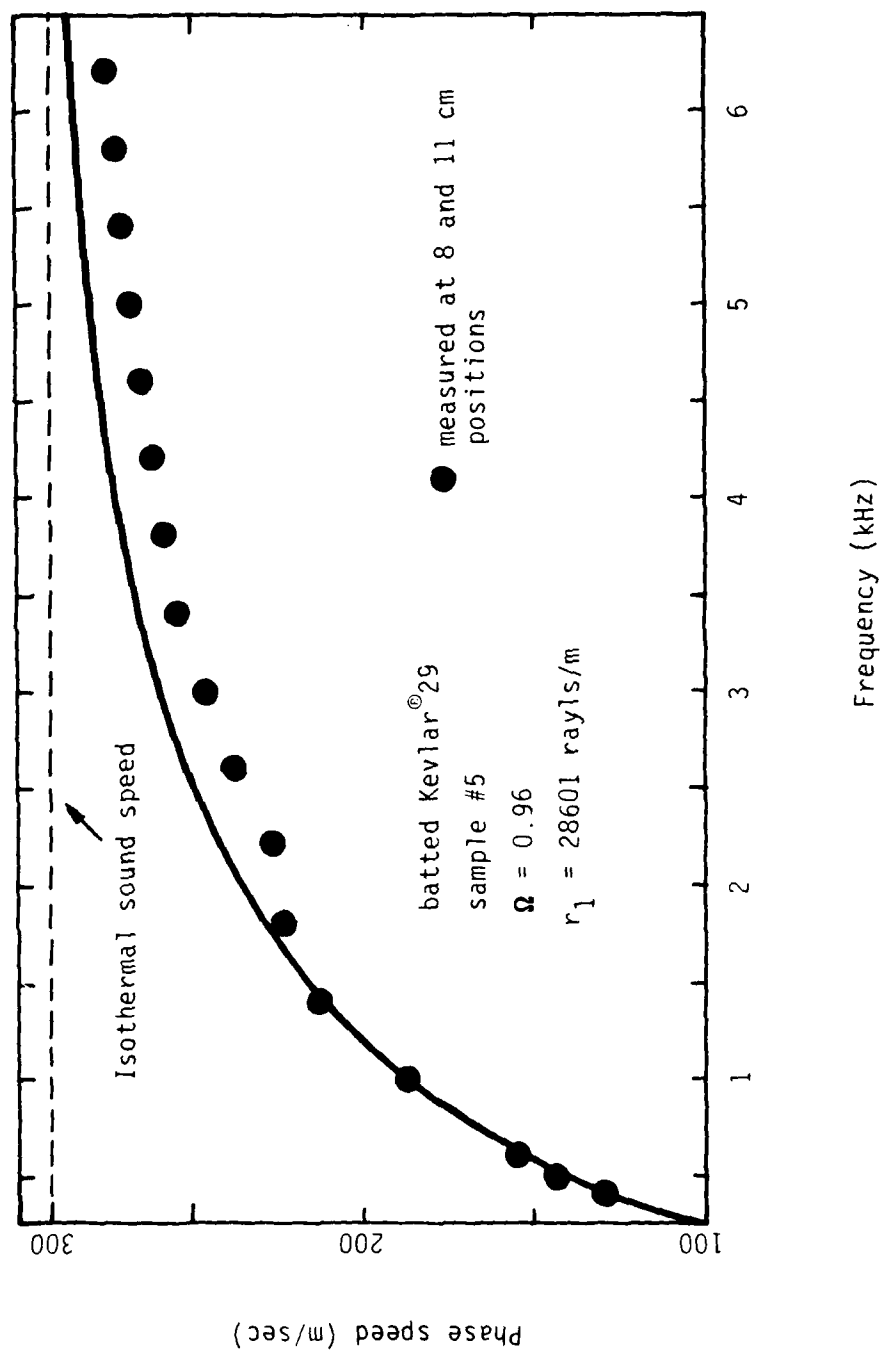
Figure 4-7

Comparison of measured and predicted
small-signal phase speed

AS-85-580

89

frequency is increased the predicted phase velocity and attenuation curves diverge from data. Preliminary calculations indicate that most of the discrepancy could be removed by introducing a frequency dependent sound speed and a structure factor (see below). We have no explanation for the slight discontinuity in the data near 1750 Hz in both figures.

Recently published work by Lambert and Tesar[7] apparently makes it possible to obtain an a priori value of the structure factor and the frequency dependent bulk modulus from resistivity tests no different from those discussed here. Lambert and Tesar's theory is somewhat involved, but predictions of the small-signal phase speeds and attenuation constants for Kevlar[R]29 are accurate over a wide range of porosities. Indeed, if their work had been published earlier, their formulations of the structure factor and frequency dependent sound speed would probably have been incorporated in the present study. The behavior of these properties at high intensity remains, however, unknown. Nevertheless, predictions based on our simple theory are, by demonstration, reasonably accurate and have the advantage of being substantially less complex. A more detailed comparison of the two approaches, including application to nonlinear effects, would be a good idea for a future study.

The attenuation data serves as a check of the assumption that $r_1$ is the same for ac and dc flows. Table 4-2 compares the linear resistivity coefficients for ac and dc flows for six of the samples tested. Data taken at low frequency (where our theory is highly accurate) yield estimates of the value of $r_1$ which are consistently lower than their dc counterparts by a few percent. The agreement is good enough, however, to validate our assumption that the ac and dc resistivities are equivalent for small signals.

## TABLE 4-2

### Comparison of measured static flow and acoustic resistivity

| Sample | $\Omega$ (nominal) | $r_1dc$ (mks rayl/m) | $r_1ac$ (mks rayl/m) | $\Delta\%$ |
|--------|--------|--------|--------|--------|
| 1 | 0.94 | 50233 | 48831 | -2.8 |
| 2 | 0.98 | 10437 | 9895 | -5.2 |
| 3 | 0.96 | 29789 | 29054 | -2.5 |
| 4 | 0.94 | 51539 | 48395 | -6.1 |
| 5 | 0.96 | 28601 | 27059 | -5.4 |
| 6 | 0.94 | 52891 | 50898 | -3.8 |

### 3. Finite-Amplitude Tones

We now discuss the SPL and relative phase data for finite-amplitude tones. The finite-amplitude signal at the reference microphone is not a pure tone, but rather a distorted sinusoid. Here we are concerned mainly with the fundamental and assume that the harmonics are small and have a negligible effect on the SPL of the fundamental. Theoretical predictions from Chapter 3 lead us to expect excess attenuation and a reduction of the phase velocity at high amplitude. In other words, a finite-amplitude tone behaves as a primary, as defined in Chapter 3. The nonlinear behavior is thought to be caused by the local increase of resistivity due to the passage of the wave. A good example of data that show excess attenuation is found in Fig. 4-8. The data is taken for sample 2, for which the porosity is $\Omega = 0.98$. The three data sets correspond to three initial source amplitudes, and the dashed lines represent small-signal attenuation. No prediction curves have been included here because the tabulated value of $r_2$ for this sample is considered inaccurate. This data set contains the most pronounced excess attenuation we measured. The
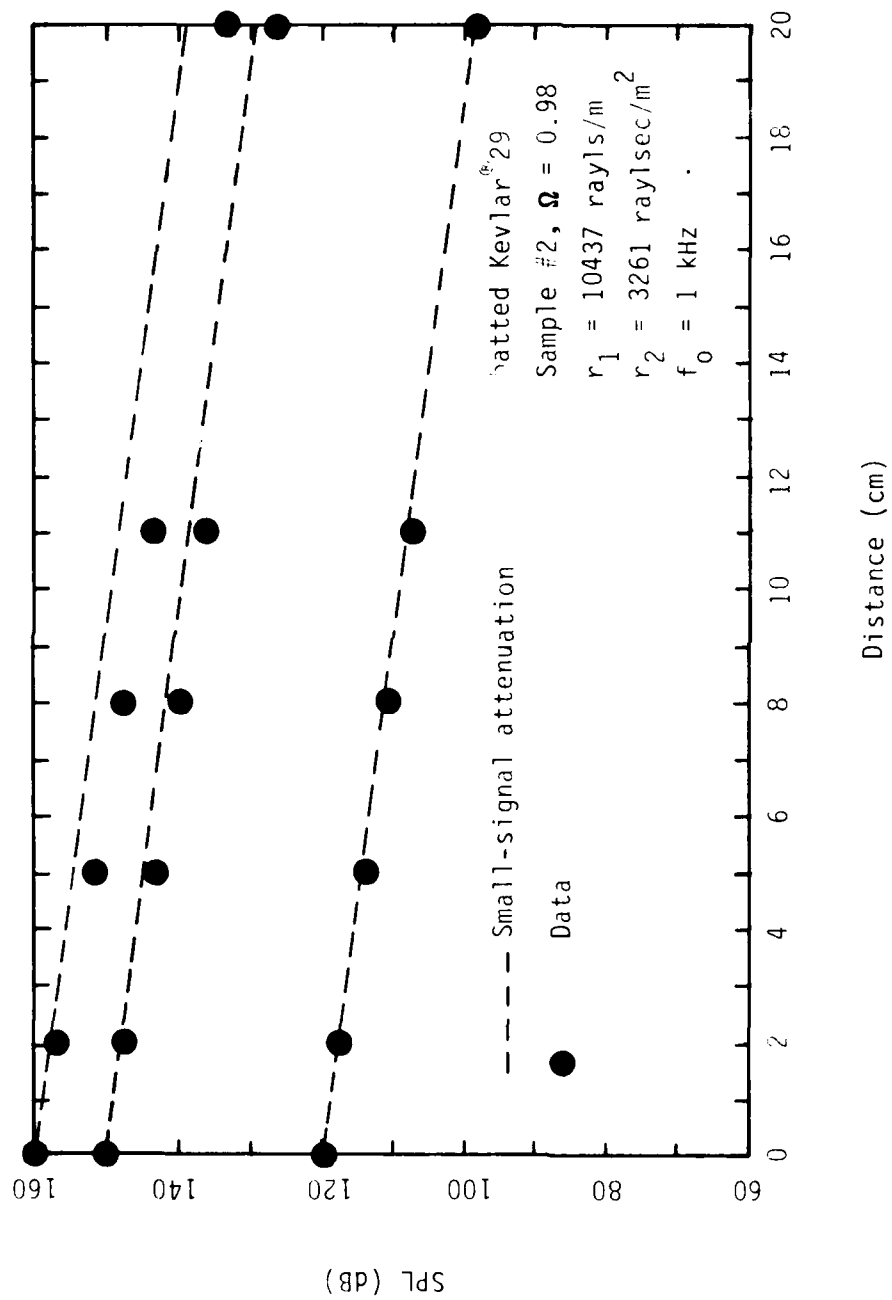
Figure 4-8
Excess attenuation

92

explanation is that the lower small-signal attenuation rate allows the wave to remain strong for a longer period. The nonlinear effects are therefore relatively more important than in other samples.

The other samples we tested showed very little excess attenuation (see, for example, Fig. 4-9) because their small-signal attenuation rates were large and our maximum source level was only 160 dB. (By using source levels of up to 170 dB, Kuntz[1] was able to obtain large excess attenuations over a wide range of porosities.) The three data sets in Fig. 4-9 once again correspond to three initial source amplitudes, but this time predicted propagation curves are included for each. At low intensity the predictions match the data well, but as the intensity is increased the expected amount of excess attenuation is exaggerated by the approximate solution. This is an example of the tendency of the approximate solution to "overshoot" as discussed in Chapter 3. Calculations have shown that the second derivative term discarded from Eq. (3.27) is more important than had originally been thought. Because of the inaccuracy of the solution, we are unable to determine whether $r_2$ is the same for ac and dc flows. If the solution were exact, the validity (or lack thereof) of the measured static flow value would be immediately apparent. Unfortunately, the solution is inexact. It was hoped that the measurements could be used as a test of the theory and, in particular, a check on the assumed value of $r_2$, but since the solution of Eq. (3.29) misrepresents the theory, no direct assessment of the accuracy of the static flow of $r_2$ can be made. Nevertheless, the excess attenuation behavior is at least qualitatively predicted and is compatible with the concept of nonlinearly augmented local resistivity.

Measurements of the relative phase between two points in the wavefield indicate quite strongly that the phase speed of the pressure wave is a function of the wave amplitude. The relative phase is defined as the difference in phase between

93
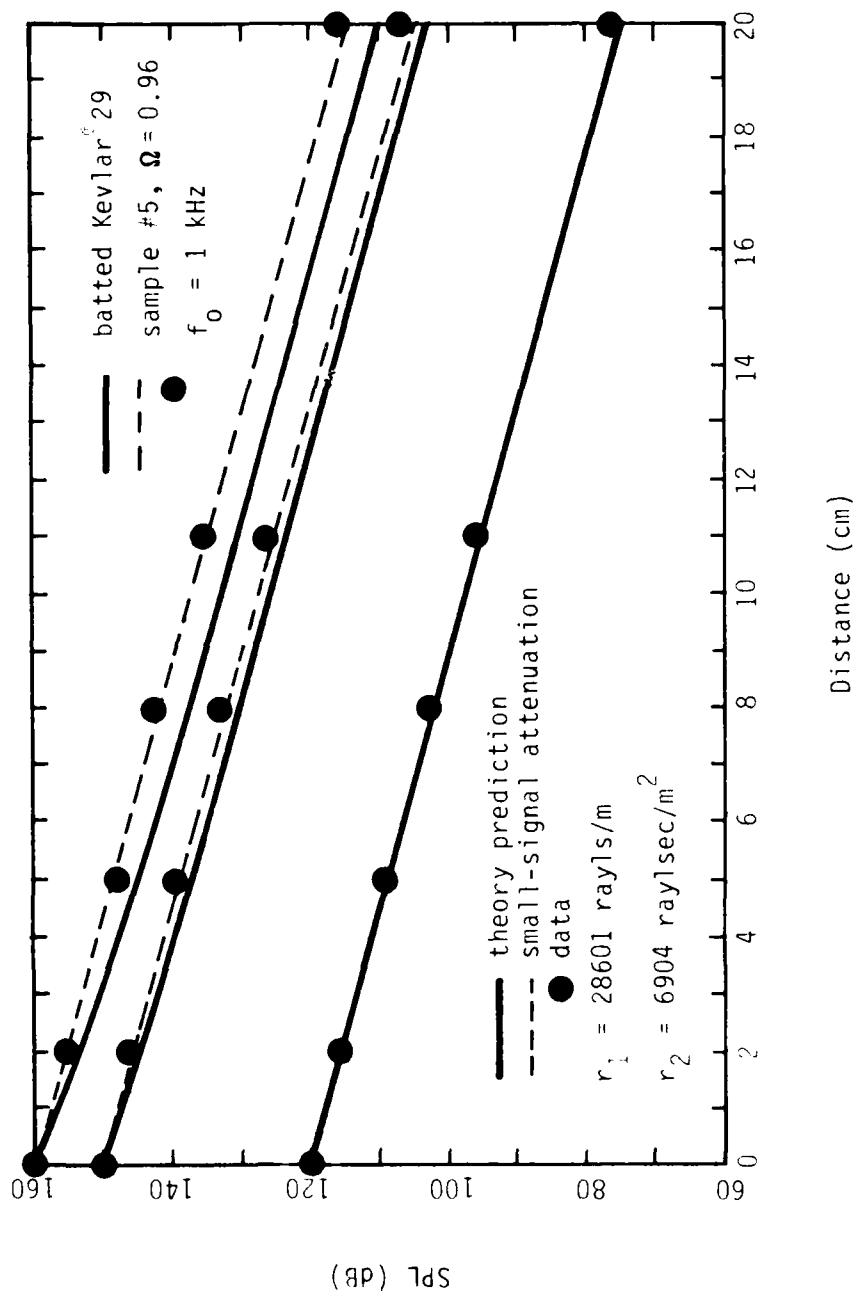
Figure 4-9

Comparison of measured excess attenuation
data and predictions

AS-85-582

the signals at the reference and a downstream point, i.e., $\phi\Delta = \phi(x) - \phi(0)$. An increase of the relative phase corresponds to a decrease in the phase velocity. Figure 4-10 is an example of some typical data. The solid curve represents predicted values of the relative phase as a function of SPL. Abscissa values represent deviations of the relative phase from the predicted small-signal value $\Delta\phi_{ss}$, that is,

$$\Delta\phi_{graph} = \phi(x) - \phi(0) - \Delta\phi_{cs} .$$

Vertical offset errors due to inaccurate predictions of $q_{1r}$ are present which complicate the picture somewhat. However, the shape of the curve is a generally dependable measure of the change in phase velocity.

The measured relative phase data did some things we expected, and others we did not. As the SPL was increased, the relative phase usually decreased at first, but always increased at higher levels. The decrease took many forms; sudden jumps were as common as gradual changes. The overall tendency of the relative phase to increase with SPL is compatible with the concept of augmented resistivity, because the data show that the phase velocity of the pressure wave was reduced at high amplitude. The decrease in the relative phase was totally unexpected. Small hysteresis loops were also observed; that is, the data followed a different path depending on whether the SPL was increasing or decreasing. The anomalous decrease, sudden jumps, and hysteresis behavior suggest a nonlinear bistability for which the local stochastic variation of the quantities $r_1$ and $r_2$ causes there to be more than one possible wave number at high intensity.

The skeptical reader might suspect that the hysteresis behavior was introduced somewhere in the measurement apparatus. The measurements were repeatable, however, for various microphones, microphone positions, frequencies,

95
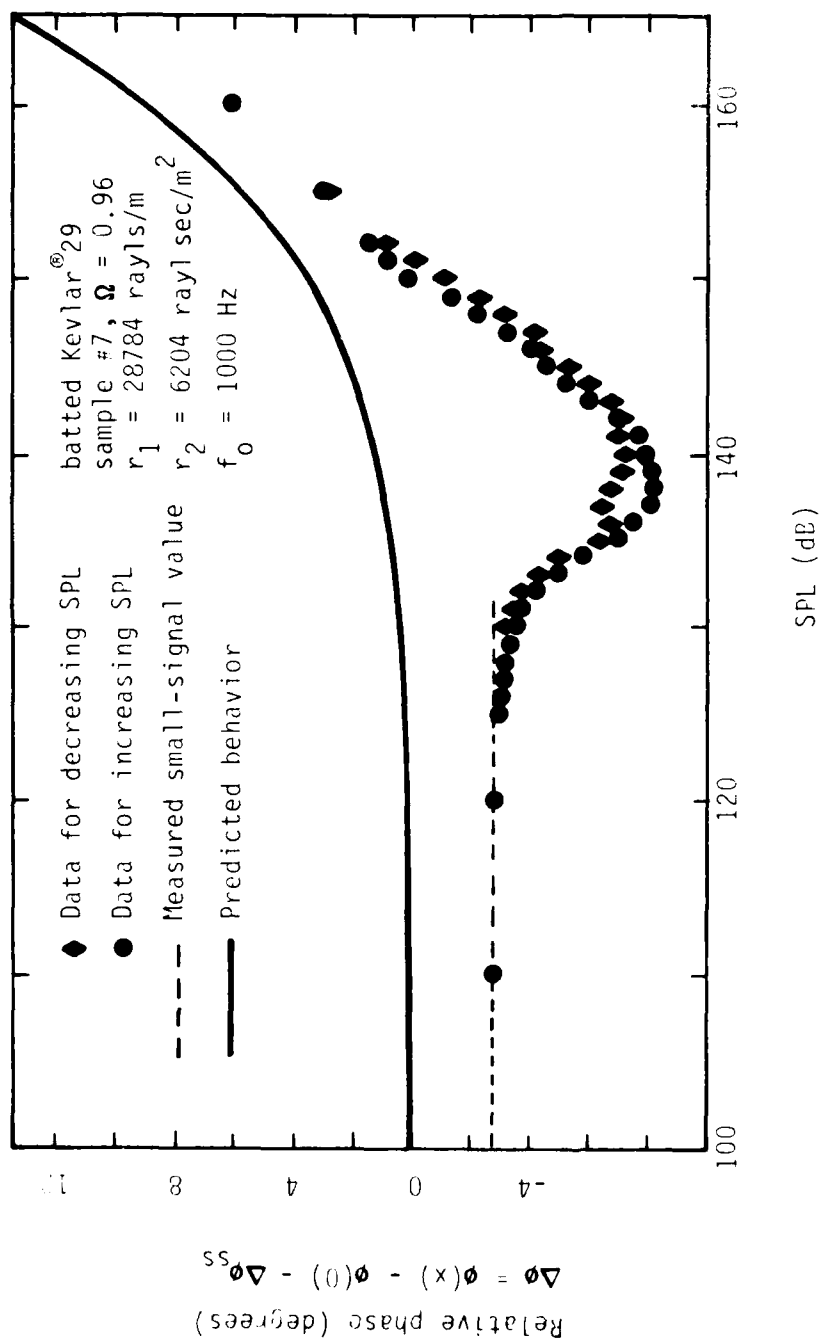
Figure 4-10

Amplitude-dependent relative phase, with hysteresis

AS-85-583

and even different FFT analyzers. We therefore believe the measurements to be true representations of actual acoustical events.

We conclude from the finite-amplitude tone measurements that attenuation is indeed increased and phase velocity reduced at high amplitude. The approximate solution gives good qualitative predictions for both. Although we should have liked to draw a conclusion concerning the values of $r_2$ for ac and dc flows, the inherent inaccuracy of the approximate solution prevents us from doing so. We are therefore unable to confirm or deny our initial assumption that the dc and ac resistivity are interchangeable at all particle velocities.

### 4. Distorted Sinusoids

Having finished with the fundamental, let us now concentrate on the higher harmonics of the signal. The higher harmonics generated by the propagating fundamental are no longer neglected, nor are those present at the reference position. Analyzing the behavior of the higher harmonics gives us information about the form of the $r(u)$ function. A computer program was written to numerically solve Eq. (3.29) for periodic waves. A cubic distortion pattern is predicted and the harmonic propagation curves are predicted to cross. Figures 4-11, 4-12, and 4-13 give measured and predicted harmonic propagation curves for three different samples. In each case, data for the fundamental show that it behaves essentially as treated in the previous section. In fact, the small difference between the analytical (see Fig. 4-9) and numerical solutions for the fundamental demonstrates the minimal effect of the higher harmonics on the fundamental. The SPL of the second harmonic is seen to decrease monotonically with distance just as the SPL of the fundamental does. Therefore the second harmonic also functions as a primary. The third harmonic SPL, however, increases initially and routinely equals or exceeds the level

97
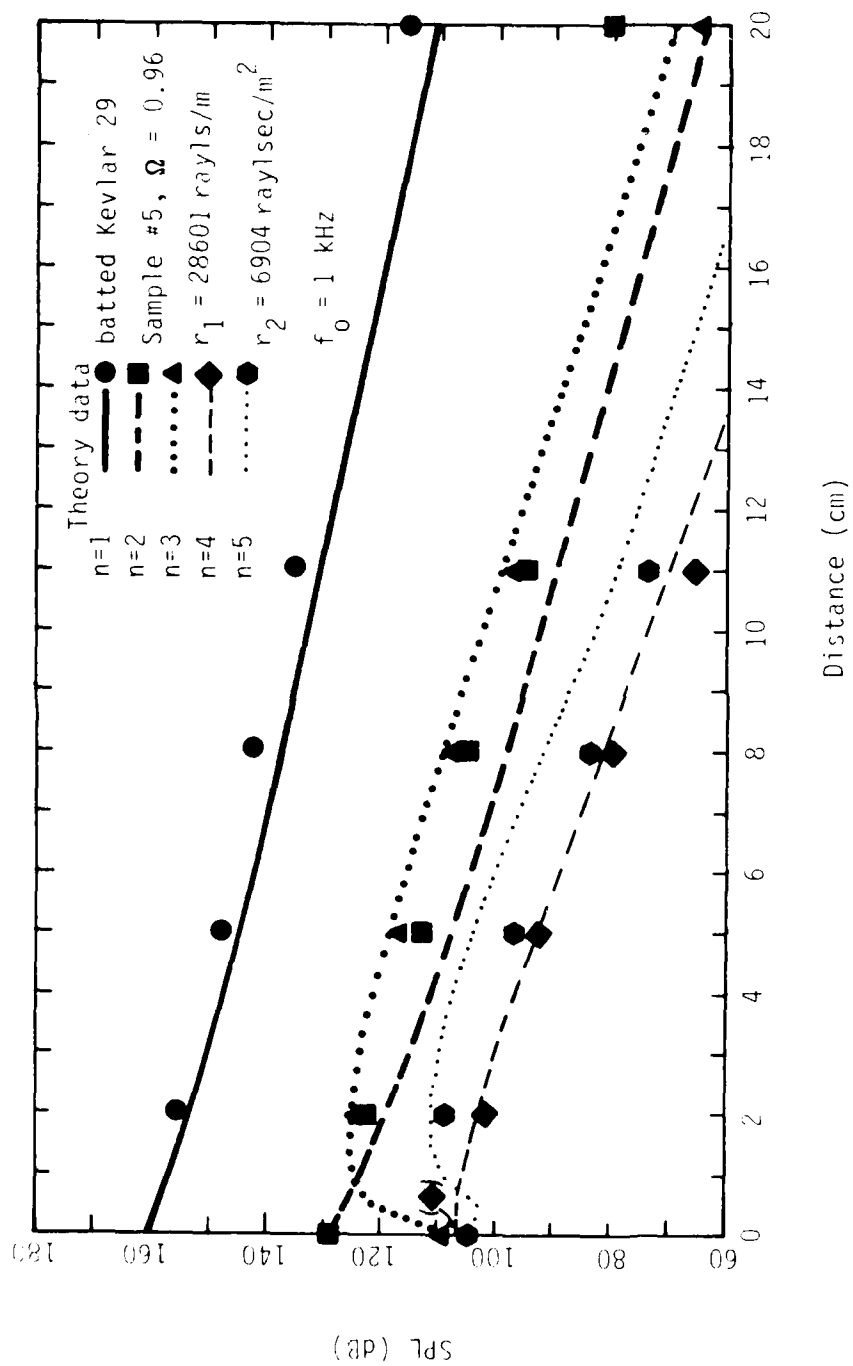
Figure 4-11

Comparison of measured and predicted
harmonic SPL versus distance, sample 5

AS-85-584

root function is not distributive. Even though we prefer the sgn(u) formulation (as discussed extensively in previous chapters), we use the quadratic form of the resistivity in preparation for a perturbation solution.

Since the porous material is assumed isotropic the one-dimensional particle velocity u can be replaced by its vector counterpart,

$$p_t + \rho_0 \vec{\nabla} \cdot \vec{u} = 0 \quad . \tag{6.1}$$

The nondimensional continuity equation, expressed in vector notation, is

$$\hat{p}_T + \vec{\nabla} \cdot \vec{v} = 0 \quad , \tag{6.2}$$

and the momentum equation becomes

$$\vec{v}_T + \frac{\vec{\nabla}\hat{p}}{\Omega} + R_1\vec{v} + R_3\left(\vec{v}(\vec{v} \cdot \vec{v})\right) = 0 \quad , \tag{6.3}$$

where the vector form of the quadratic nonlinear resistivity $R_3\vec{v}\cdot\vec{v}$ has been used. The wave equation is found by adding the results of the operations $-\vec{\nabla}/\Omega$ on the continuity equation and $\partial/\partial_T$ on the momentum equation:

$$\vec{v}_{TT} - \frac{\vec{\nabla}(\vec{\nabla} \cdot \vec{v})}{\Omega} + R_1 v_T + R_3\left(\vec{v}(\vec{v} \cdot \vec{v})\right)_T = 0 \quad . \tag{6.4}$$

This equation is awkward in vector form and has the added disadvantage of allowing rotational solutions. Since we are interested in scalar fields describing irrotational motions, two modifications are made: the velocity vector is first replaced with the gradient of the scalar potential field $\nabla \varphi$,

$$\vec{\nabla}\varphi_{TT} - \frac{\vec{\nabla}(\nabla^2\varphi)}{\Omega} + R_1\vec{\nabla}\varphi_T + R_3\left(\vec{\nabla}\varphi(\vec{\nabla}\varphi \cdot \vec{\nabla}\varphi)\right)_T = 0 \tag{6.5}$$

and the divergence of the result is taken to reach the scalar form

$$\nabla^2\left(\varphi_{TT} - \nabla^2\varphi + R_1\varphi_T\right) + R_3\left((\nabla^2\varphi + \vec{\nabla}\varphi \cdot \vec{\nabla})(\vec{\nabla}\varphi \cdot \vec{\nabla}\varphi)\right) = 0 \quad . \tag{6.6}$$

# CHAPTER 6

## THEORY OF LINED DUCTS

### A. Introduction

Chapter 6 is an application of the accumulated knowledge of the fore-going chapters to the problem of a lined duct. We are particularly interested in the effect of the material nonlinearity on the absorptive power of the duct. We begin by deriving a nonlinear nondimensional vector wave equation for acoustic waves in the material. Next we investigate the process of nonlinear reflection from a porous half-space. Lastly, a third order perturbation solution for a lined duct is prepared, but is never executed because of its forbidding complexity. Instead, we propose an ad hoc model to aid in understanding the nonlinear effects.

### B. Nonlinear Nondimensional Vector Wave Equation

In previous chapters the nonlinear resistivity was calculated assuming one-dimensional flow. In order to consid . a lined duct, however, a general expression for the resistivity is needed. In particular, we are interested in finding vector expressions to replace Eqs. (2.9) and (2.10) for use in a vector wave equation. Of the two previously used forms of the nonlinear resistivity $u \, \text{sgn}(u)$ and $u^2$, the former represents the instantaneous speed of the flow and the latter the square of the velocity. It turns out that the square of the instantaneous particle velocity can be expressed in vector terms as $\vec{u} \cdot \vec{u} = |u|^2$. The vector form of Eq. (2.10) therefore lends itself rather well to a perturbation method of solution. The instantaneous particle speed is of course $\sqrt{\vec{u} \cdot \vec{u}}$. An expression of the resistivity based on this form, however, does not allow a perturbation solution because the square

113

Three topics are suggested for future study. First, there is a definite need for more accurate solutions of the infinite set of coupled second order inhomogeneous ordinary differential equations represented by Eq. (2.26). Second, the accuracy of theoretical predictions may benefit somewhat from a more elaborate model of the material which includes structure factor and a frequency dependent sound speed. Furthermore, the change in these parameters at high intensity should be studied. Third, since the material is likely to be used in an inhomogeneous state, the effects of the inhomogeneity should be investigated.

The theory developed here was originally intended to be applied to the problem of absorption of high intensity sound in a lined duct. Theoretical work on this topic is already being pursued by this author. If point- and local-reaction models of duct liners are to be used with confidence, it will be necessary to establish the validity of amplitude dependent impedance expressions derived in this work. Despite the difficulties encountered, the theory we have developed appears to offer the best hope for solving the important and practical problem of high intensity sound absorption in lined ducts.

On the basis of the qualitative and quantitative agreement between the theory and experiment, we conclude that

1)    the resistivity is the dominant mechanism for acoustic loss and distortion in a porous material,

2)    the mathematical form of the resistivit; function is $r = r_1 + r_2 u \operatorname{sgn}(u)$ for static flows and is retained for acoustic flows, and

3)    the value of $r_1$ is indeed the same for ac and dc flows, but

4)    the agreement between the value of $r_2$ for ac and dc flows cannot be determined because solutions are inaccurate for finite-amplitude waves.

Two phenomena were observed which suggest modifications for future theories. Small-signal measurements indicate that the accuracy of the theory would benefit somewhat from a more sophisticated model in which the sound speed were allowed to be frequency dependent, and a structure factor were included. However, there is currently little knowledge available on the variation of these parameters at high intensity. The second phenomenon is the hysteresis loops that were observed in the phase speed versus amplitude data. The nonlinear bistability implies that local stochastic variations of the material resistivity, i.e., material inhomogeneity, may be important at high intensity.

The experiments had two basic shortcomings. First, the static flow test compressed some high porosity samples so much that even our otherwise highly effective compression compensation algorithm could not account for the changes. Use of lower porosity samples solved the first problem but led to the second: the source amplitude was not high enough to observe significant excess attenuation for all the porosities tested. Results of future experiments will be more conclusive if these two problems can be solved.

measurements were attempted. Quantitative agreement ranged from satisfactory to excellent.

(1) Low intensity attenuation and phase speed measurements were in very good quantitative agreement with predictions based on the measured dc value of $r_1$; at low frequency ($< 1500$ Hz) the agreement was excellent. We therefore surmise that the dc and ac values of $r_1$ are the same.

(2) Measurements of sound pressure level versus distance at high intensity showed some excess attenuation, but in general we observed much less than was predicted. The assumptions on which Eq. (3.29) is based were apparently more easily violated than we had expected. It was hoped that this solution could be used to demonstrate the equivalence of $r_2$ for ac and dc flows, but the inaccuracies prevent us from drawing a solid conclusion. Nevertheless, the dc value of $r_2$ seems to be at least approximately correct for use with acoustic signals. The relative phase data deviates from predictions as a result of a process which we suspect is a nonlinear bistability induced by the inhomogeneity of the material. The predicted increase in relative phase (a decrease in phase speed) appears, however, consistently at high intensity.

(3) The existence of cubic distortion is compatible with both a $u^2\text{sgn}(u)$ or $u^3$ nonlinearity. The gross details of the harmonic propagation curves are very adequately predicted; for the most part the predictions are within 5 dB of the measured data.

functions of frequency. Measured attenuations for all samples were of the order of hundreds of dB/m and increased from low values at low frequency towards asymptotic values at high frequency. Phase speeds were substantially reduced at low frequency and increased to near the isothermal sound speed at high frequency. At high intensity, measurements of the SPL of the fundamental with distance showed a small but significant amount of excess attenuation. Because of the limited power-handling capacity of our acoustic source, however, the saturation region was out of reach. The approach to saturation has been much better documented by Kuntz.[1] The relative phase of the fundamental between the signals at two positions was measured as a function of amplitude. An increase in relative phase corresponds to a decrease in the phase speed. The measured relative phase was stable at low intensity, usually decreased slightly as the amplitude was increased, and always finished with a strong increase at the highest SPLs tested. The decrease was not always gradual, but often involved sudden jumps of several degrees for a source level change of 1 dB. In addition, small hysteresis loops were observed in the relative phase data. Finally, the harmonic distortion pattern was indeed observed to be cubic, that is, the first and second harmonic both behaved like "fundamentals"; that is, they decreased monotonically in strength with distance. The third harmonic SPL, by contrast, was observed to routinely exceed the amplitude of the second. The fourth and fifth harmonics often increased initially in strength as well. Such a distortion pattern could not be caused by a hydrodynamic distortion mechanism and is solely attributed to nonlinearity of the porous material resistance.

We now compare the theoretical predictions and experimental observations with a view towards evaluating the validity of the model. Excellent qualitative agreement was obtained for all predicted phenomena for which

summarized in the statement that the mean resistivity increases with the wave amplitude. Finite-amplitude tones are therefore predicted to have higher attenuation rates and impedances and lower phase speeds than small-signal waves of the same frequency. Saturation behavior is predicted at very high intensities; i.e., nonlinear losses determine the maximum pressure amplitude which can be reached at a given point in the wavefield.

Numerical solutions of Eq. (3.29), including all harmonics, are performed by a computer program written for this purpose. Predictions based on this solution lead us to expect a cubic harmonic distortion pattern in which the fundamental energizes the third and higher odd harmonics. The second harmonic is predicted to behave as a fundamental as well and to directly energize every other even harmonic, that is, the sixth, tenth, fourteenth, etc. The fourth harmonic and multiples thereof are products of the interaction between the first and second harmonics.

Several experiments were performed to investigate the propagation of finite-amplitude sound in porous materials. A traveling wave tube filled with a porous sample was fitted with six microphones, a compression driver, and extensive electronic devices for the acoustic measurements. The tube, with the same sample intact, was reconfigured with pressure gages and flow meters for static flow resistivity measurements. The samples were batted Kevlar[R] 29 and had porosities $\Omega=0.94$, 0.96, and 0.98. Small-signal measurements were taken in the frequency range 400-6200 Hz. Finite amplitude measurements were conducted at a frequency of 1 kHz. Sound pressure levels of up to 160 dB (at the reference position) were used.

Experimental results were in general consistent with predictions. Measurements at low intensity showed the attenuation and phase speed were strong

107

completely overshadowed by both the linear and nonlinear resistivity effects and are neglected. The isothermal sound speed is used for all frequencies. We have therefore established the resistivity as the prime mechanism for attenuation and distortion of acoustic signals in porous materials. The apparent lack of sophistication of the model respresents a deliberate retreat from more elaborate theories; the simplified theory has the advantage of being easily extended to include finite amplitude behavior.

A nonlinear wave equation, Eq. (2.23), is derived from the model. The wave equation has a relatively uncomplicated form, but turns out to be very difficult to solve in the general case. Transformation to the frequency domain produces an infinite set of coupled inhomogeneous Helmholtz equations, one for each harmonic.

In the low intensity limit the Helmholtz equations are homogeneous and solutions are easily obtained. Because the propagating acoustic wave is subject to diffusion (see Chapter 2), we expect to observe high attenuation rates, severe dispersion, and low phase speeds.

Solutions for high intensity waves are considerably more difficult to find. An approximate first integral, Eq. (3.29), of the Helmholtz equation was derived because numerical calculations for the solutions of the second order Helmholtz equations (Eq. (2.26)) were unstable. Two different approaches were used to solve Eq. (3.29). In one the higher harmonics were neglected entirely and in the other the higher harmonics are taken into account. Using the first approach we are able to obtain an analytical solution from which expressions for impedance, and the amplitude and phase speed of both the particle velocity and pressure waves are found. All of the many informative results obtained from these solutions may be

# CHAPTER 5

## CONCLUSIONS FOR CHAPTERS 1 THROUGH 4

The propagation of finite amplitude sound in rigid air-filled porous materials has been studied both theoretically and experimentally. In particular we have studied the effects of amplitude dependent resistivity on propagation of acoustic signals. Experiments performed on batted Kevlar®29 are in at least qualitative, and in many cases quantitative, agreement with the theoretical predictions.

The theory is based on the following model of the porous material: the material is rigid, incompressible, and homogeneous and has only two important properties, porosity $\Omega$ and resistivity r. Detailed knowledge of the material geometry is unnecessary for this model. The resistivity has been measured for dc flows and is shown to be the following function of flow velocity u: $r=r_1+r_2 u \operatorname{sgn}(u)$ (see Eq. (2.9)).[†] Previous work by other authors[13,21] shows that the static flow resistivity function may be applied to oscillatory (acoustic) flows. The components of the flow resistivity play two different roles. The "linear resistivity" $r_1$ determines, among other things, the small-signal attenuation, which in a typical porous material is quite severe. The amplitude dependent resistivity leads to strong nonlinear effects, namely excess attenuation and harmonic distortion. The effects of hydrodynamic distortion, which normally give rise to shock formation, are

---

[†]The model of Eq. (2.10), $r=r_1+r_3 u^2$, is far from useless; a discussion of results based on this model is given in Appendix B.

In addition, two results have been obtained which, although not con-clusive, are considered trustworthy and merit further study:

1) the resistivity can be separated into functions of porosity and flow velocity as $r = r_1(\Omega) f(u)$, where the as yet unspecified coefficients in the function $f(u)$ are independent of porosity,

2) an apparent nonlinear bistability has been observed which indicates that the local stochastic variation of the material properties may be of importance at high intensity.

We have not been able to detemine whether the value of $r_2$ is the same for ac and dc flows because of the inaccuracy of our solution.

physical boundary, the material/air interface, which is <u>not</u> located at $x=0$. The nth component at $x=0$ is partly due to energy upshifted while traveling from the physical boundary at the reference position. Since the waves represented by the two parts of the solution travel at different speeds[†] the upshifted signal is occasionally out of phase with the signal represented by the homogeneous solution. Destructive interference takes place, and one and occasionally more spurious cusps may appear in the predicted propagation curve for a harmonic.

E. Summary of Experimental Work

As a test of the validity of our theory, we have performed a series of experiments to examine the behavior of acoustic signals in batted Kevlar 29 at low and high intensity. The following five conclusive results have been obtained .

1) The static flow resistivity depends on the flow speed as $r=r_1+r_2 u\,\mathrm{sgn}(u)$.

2) The value of $r_1$ for oscillatory flows is equivalent, or nearly equivalent, to that for static flows.

3) A finite amplitude tone undergoes excess attenuation which is somewhat less than predicted.

4) A finite-amplitude tone propagates more slowly than its small signal counterpart.

5) The harmonic distortion pattern has cubic character.

Although point (5) admits both the $u^2$ and $\mathrm{sgn}(u)$ resistivity models, the evidence from (1) implies that the $\mathrm{sgn}(u)$ model is correct.

---

[†]Consider that the harmonic tends to travel at $C_{pn}$ while the primaries, whence comes the inhomogenous part, travel at $C_{p1}$ and $C_{p2}$.

of the second harmonic. The upshifted energy from the fundamental skips over the second harmonic and reinforces the third. As a result, the propagation curves for the second and third harmonics may cross. This is a distinguishing mark of the cubic distortion pattern which was discussed in Chapter 3. An ordinary quadratic nonlinearity, such as that for hydrodynamic distortion or that assumed by Kuntz, would cause the second harmonic to behave as a distortion product rather than a primary. A quadratic nonlinearity does not therefore fit the distortion pattern observed here. Data for the fourth and fifth harmonics indicate that both receive significant energy from the primaries. Their behavior, however, neither confirms nor denies a cubic distortion mechanism.

The predicted harmonic propagation curves are in substantial agreement with the data. Predictions of the SPL of the fundamental and second harmonic are *too low because the numerical solution exaggerates the nonlinear effects.* The overshoot phenomenon has a different effect on distortion product predictions. Since the solution exaggerates the nonlinear effects, the approximate solution tends to overestimate the amount of energy received by a distortion product and thus overestimates the SPL as well. The error is balanced somewhat, however, because the approximate solution also underestimates the strength of the primaries which drive the distortion products.

Prediction curves for the higher harmonics, especially those that receive a great deal of upshifted energy, often have cusps (see $n=5$ curve in Fig. 4-11). The cusps are artifacts of the solution procedure. The cause lies in the fact that the differential equation is solved for initial conditions at the reference postion $x=0$. The inhomogeneous part of the solution, representing energy upshifted from the primaries, is set to zero by the computer program at this point. In reality, the upshifted energy is nonzero at the reference position: it is only zero at the true

101
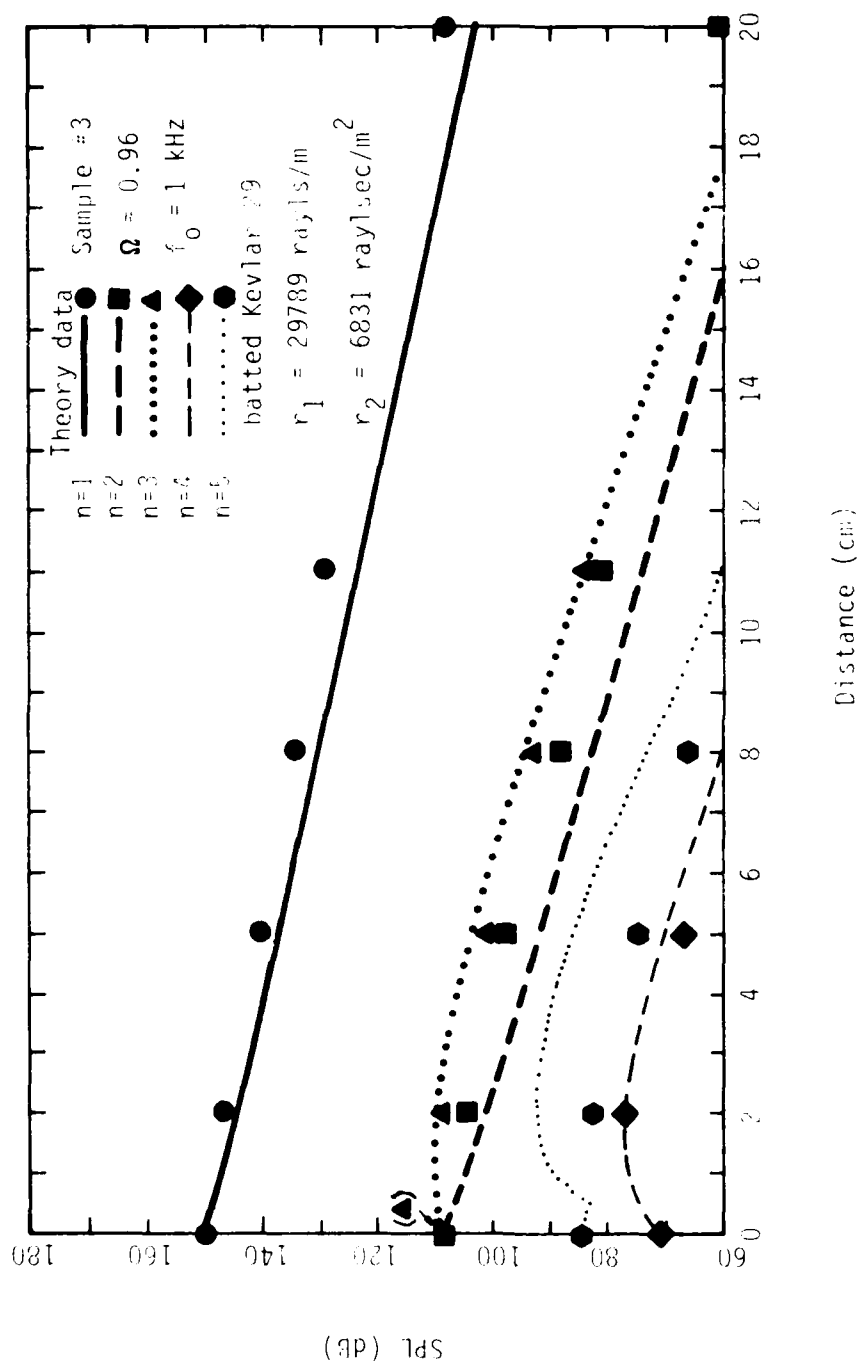
Figure 4-13

Comparison of measured and predicted
harmonic SPL versus distance, sample 3

AS-85-586
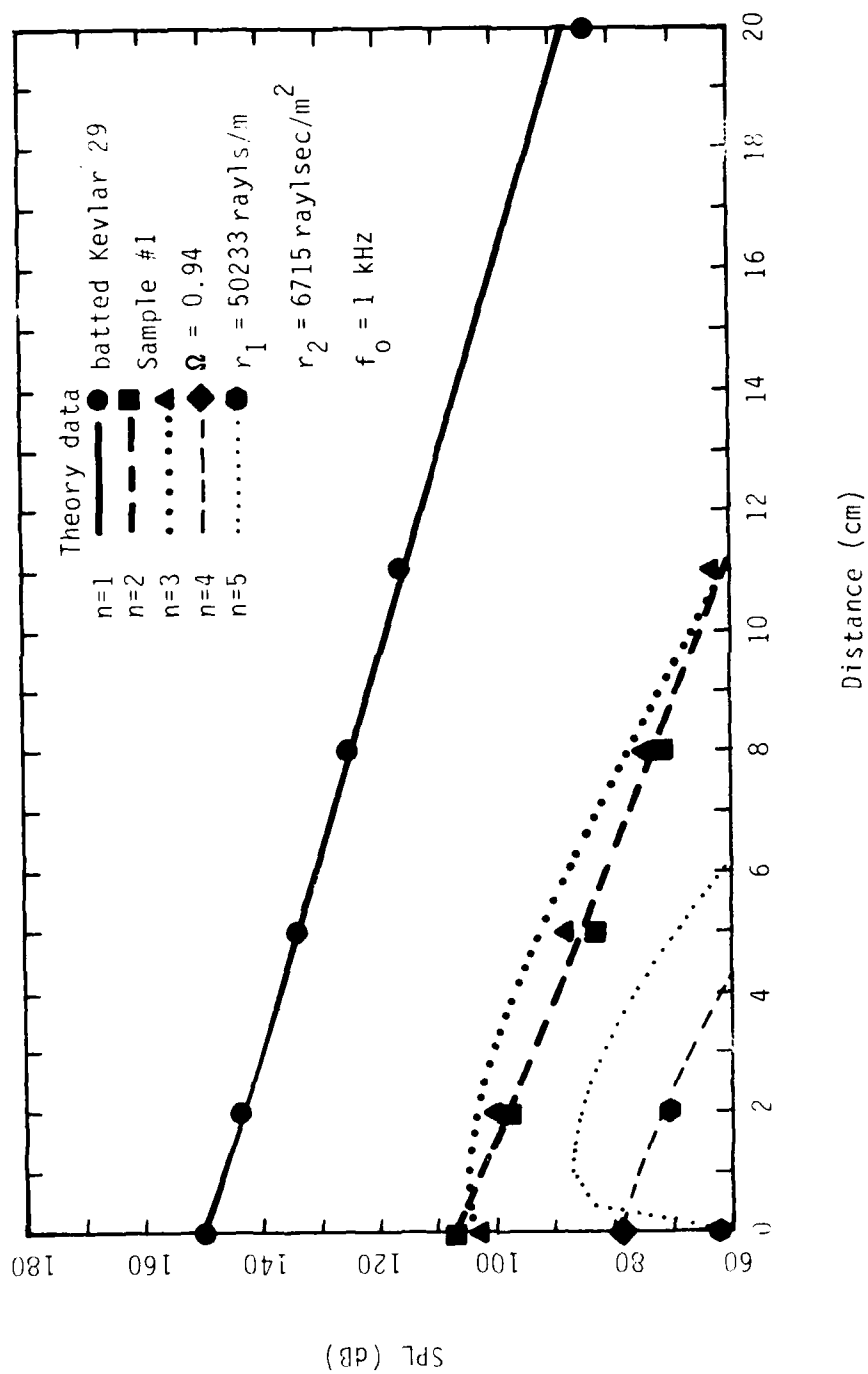
Figure 4-12

Comparison of measured and predicted
harmonic SPL versus distance, sample 1

The frequency domain version of this equation is found by substituting for the potential in the by now familiar manner to give

$$\nabla^2(\nabla^2 + q_n^2)\varphi_n = -jn\Omega R_3 \sum_p \sum_q (\nabla^2\varphi_p + \vec{\nabla}\varphi_p \cdot \vec{\nabla})(\vec{\nabla}\varphi_q \cdot \vec{\nabla}\varphi_{n-p-q}) \quad , \quad (6.7)$$

where

$$\varphi = \sum_n \varphi_n(\hat{x}) \exp(jnt)$$

and

$$\varphi_{-n} = \varphi_n^* \quad .$$

The perturbation solution is prepared by expressing the nth frequency component of the potential field as

$$\varphi_n = \epsilon\varphi_{n1} + \epsilon^3\varphi_{n3} + \ldots, \quad (6.8)$$

where only the first and third orders are represented because the second is homogeneous and therefore redundant with the first. The value of $\xi$ will be specified later. Substitution into Eq. (6.7) and grouping by powers of epsilon gives the following relations:

$$\nabla^2(\nabla^2 + q_n^2)\varphi_{n1} = 0 \quad (6.9)$$

and

$$\nabla^2(\nabla^2 + q_n^2)\varphi_{n3} = -jn\Omega R_3 \sum_p \sum_q (\nabla^2\varphi_{p1} + \vec{\nabla}\varphi_{p1} \cdot \vec{\nabla})(\vec{\nabla}\varphi_{q1} \cdot \vec{\nabla}\varphi_{n-p-q1}) \quad . \quad (6.10)$$

Once the first order field is specified, the third order field can be found by operational integration.

Later we find that the perturbation technique is very awkward for application to the problem of lined ducts because of the enormous complexity of the nonlinear interaction of the wave fields. The perturbation solution nevertheless serves to illuminate several interesting physical processes including

115

reflection of an intense wave from a porous half-space as discussed on the next section.

## C. Reflection from Porous Boundary

### 1. Small-Signal Problem

The problem of the reflection of sound from a porous material is interesting for low intensity sound waves, but the inclusion of the effects of material nonlinearity leads to some surprising phenomena. It turns out that at high intensity the wave reflected from a porous surface does not have the same spectrum as the corresponding incident wave. This prediction relates directly to experimental observations made by Zorumski and Parrot.[27] The following investigation is predominantly theoretical in nature.

The wave equation is very complicated, but still lends itself to a workable, if somewhat tedious, perturbation solution. To begin the problem, we first define two potential fields: $\varphi^A$ in the air and $\varphi^M$ in the material. They of course have the frequency domain manifestations $\varphi_n^A$ and $\varphi_n^M$. These fields are further broken down as

$$\varphi_n^A = \epsilon \varphi_{n1}^A + \epsilon^3 \varphi_{n3}^A + \ldots \tag{6.11a}$$

and

$$\varphi_n^M = \epsilon \varphi_{n1}^M + \epsilon^3 \varphi_{n3}^M + \ldots, \tag{6.11b}$$

where $\epsilon$ is the magnitude of the potential function of the incident wave. Since nonlinear effects in the air are neglected, the Helmholtz equation for the air is homogeneous. We shall see, however, that it is still necessary to retain the third order solution in the air because it represents energy which is radiated from the material surface. The first and third order Helmholtz equations are:

116

$$\left(\nabla^2 + \frac{n}{\gamma}\right)^2 \phi_{n1}^A = 0 \tag{6.12}$$

and

$$\left(\nabla^2 + \frac{n}{\gamma}\right)^2 \phi_{n3}^A = 0 \quad . \tag{6.13}$$

In the material, Eqs. (6.9) and (6.10) apply. To further complicate matters, the wave fields in the air are composed of incident and reflected waves,

$$\phi_{nk}^A = \phi_{nkI}^A + \phi_{nkR}^A \quad . \tag{6.14}$$

The material is assumed to be of semi-infinite extent, so that the wave fields are composed solely of transmitted waves,

$$\phi_{nk}^M = \phi_{nkT}^M \quad . \tag{6.15}$$

The conditions that pressure and mass flux must balance are invoked at the boundary. The pressure boundary condition is written in potential form from the equation of continuity: the substitution of $\vec{\nabla}\phi$ for $\vec{v}$ yields

$$\hat{P}_t + \nabla^2\phi = 0 \tag{6.16}$$

and in the frequency domain this expression becomes

$$jn\hat{P}_n = -\nabla^2\phi_n \quad . \tag{6.17}$$

Equating the pressures on either side of the boundary at $\chi = 0$, we find that

$$\left.\nabla^2\phi_{nk}^A\right|_{\chi=0} = \left.\nabla^2\phi_{nk}^M\right|_{\chi=0} \quad . \tag{6.18}$$

Since the density of the air does not change across the boundary, the boundary condition for the conservation of mass is simply that the volume velocities match. In the air the volume velocity is

$$A \left.\frac{\partial \phi_{nk}^A}{\partial \chi}\right|_{\chi=0}$$

117

and in the material

$$\Omega A \left. \frac{\partial \phi_{nk}^M}{\partial \chi} \right|_{\chi = 0} ,$$

where A is the cross-sectional area of the boundary. The second boundary condition is therefore

$$\left. \frac{\partial \phi_{nk}^A}{\partial \chi} \right|_{\chi = 0} = \Omega \left. \frac{\partial \phi_{nk}^M}{\partial \chi} \right|_{\chi = 0} . \qquad (6.19)$$

The first order wave fields are defined as follows:

$$\phi_{n1I}^A = A_{n1} \exp\left(-j \frac{n}{\sqrt{\gamma}} \left(\cos\theta_n \chi + \sin\theta_n \xi \right)\right) , \qquad (6.20)$$

$$\phi_{n1R}^A = B_{n1} \exp\left(-j \frac{n}{\sqrt{\gamma}} \left(-\cos\theta_n \chi + \sin\theta_n \xi \right)\right) , \qquad (6.21)$$

and

$$\phi_{n1T}^M = C_{n1} \exp\left(-j \left(q_{n\chi} \chi + q_{n\xi} \xi \right)\right) , \qquad (6.22)$$

where $q_{n\chi}^2 + q_{n\xi}^2 = q_n^2$. The situation is depicted in Fig. 6-1, where $\chi$ is the coordinate normal to the surface and $\xi$ is the coordinate parallel. The algebraic manipulations encountered in applying the boundary conditions are tedious and not very informative; hence we simply show the results. The small-signal pressure reflection coefficient $\rho_n(\theta_n)$ is equivalent to $B_{n1}/A_{n1}$, which is

$$\rho_n(\theta_n) = \frac{B_{n1}}{A_{n1}} = \frac{\sqrt{\gamma} \, q_n^2 \cos\theta_n - n q_{n\chi} \Omega}{\sqrt{\gamma} \, q_n^2 \cos\theta_n + n q_{n\chi} \Omega} . \qquad (6.23)$$

The pressure transmission coefficient $t_n(\theta_n)$ is simply equivalent to one plus the reflection coefficient or

118
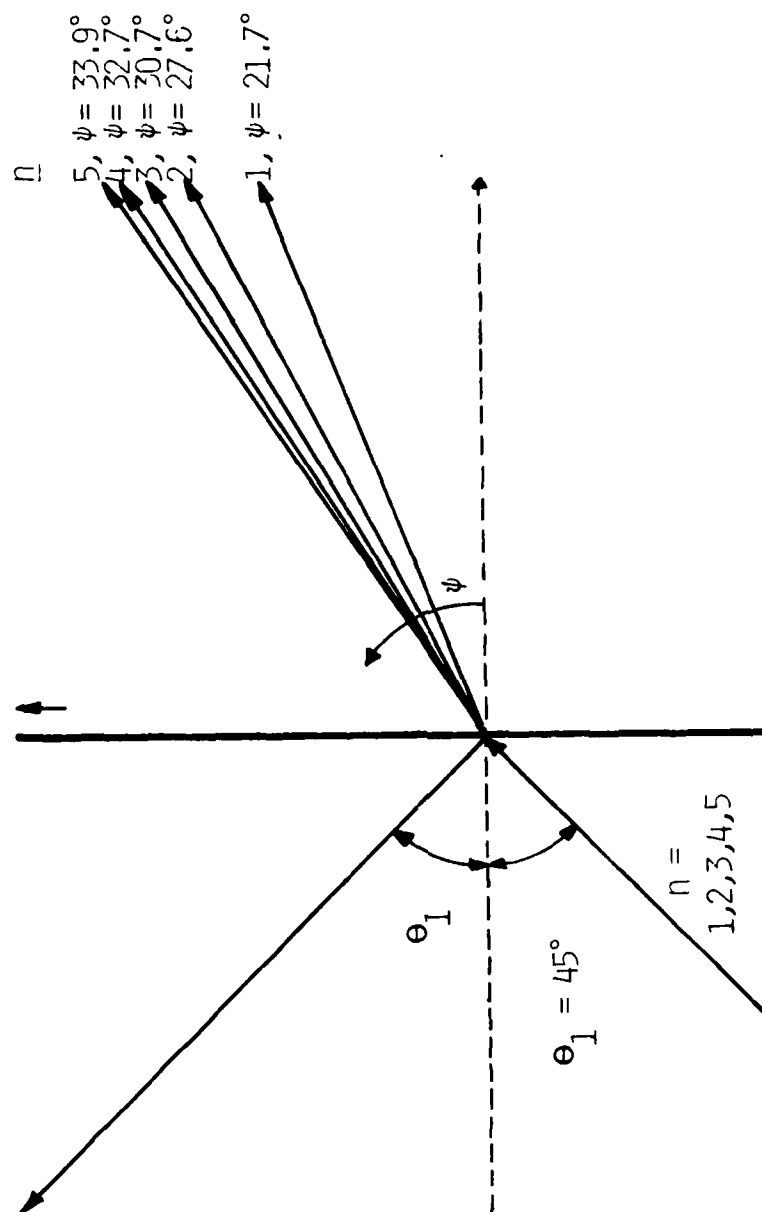
Figure 6-1

Reflection and transmission of
small-signal wave having rich spectrum

AS-85-587

$$t_n(\theta_n) = \frac{2\sqrt{\gamma}\, q_n^2 \cos\theta_n}{\sqrt{\gamma}\, q_n^2 \cos\theta_n + n q_{n\chi}\, \Omega} \quad . \tag{6.24}$$

The value of $C_{n1}/A_{n1}$ is not equal to $t_n(\theta_n)$, however, but

$$\frac{C_{n1}}{A_{n1}} = \frac{\gamma n^2}{\gamma q_n^2}\, t_n(\theta_n) \quad . \tag{6.25}$$

The magnitude of the transmitted waves, whence comes the nonlinear part of the solution, is determined by the value of $C_{n1}/A_{n1}$.

The angle of the phase fronts within the material is defined by

$$\psi_n = \tan^{-1} \frac{\text{Re}\left[q_{n\xi}\right]}{\text{Re}\left[q_{n\chi}\right]} \quad , \tag{6.26}$$

where

$$q_{n\chi} = \sqrt{q_n^2 - n^2/\gamma \, \sin^2\theta_n}$$

and

$$q_{n\xi} = \frac{n}{\sqrt{\gamma}} \sin\theta_n \, . \tag{6.27}$$

It is important to note that the angle of travel within the material is frequency-dependent for all angles of incidence except normal incidence. Since low frequency waves have lower phase speed in the material (see Fig. 4-6), they are refracted strongly. High frequency waves, on the other hand, are refracted less. An incoming signal with a rich spectrum therefore fans out into its respective components as a consequence of the severe dispersion in the material. The complete first order field in both the air and the material can now be defined from the values of $A_{n1}$ and $\theta_n$.

## 2. Nonlinear Reflection and Refraction

In this section we seek practical insights into the problem of reflection of high-intensity sound from porous materials. This work is done in preparation for the solution of the lined duct problem, and to help us understand some of the vagaries of that problem. Here we merely prepare the theoretical tools necessary for explicit solution of reflection problems; we choose to concentrate on explaining qualitative results for instructive cases.

We first define the third order wave fields for the reflected and transmitted waves:

$$\phi^A_{n3I} = 0 \quad , \tag{6.28}$$

$$\phi^A_{n3R} = B_{n3} \exp\left(-j \, n\sqrt{\bar{\gamma}} \, \left(-\cos \theta_{n3} \, \chi + \sin \theta_{n3} \xi \right)\right) \quad , \tag{6.29}$$

and

$$\phi^M_{n3T} = C_{n3} \exp\left(-j \left(q_{n\chi 3} \, \chi + q_{n\xi 3} \xi \right)\right) \quad , \tag{6.30}$$

where, for a nonlinear interaction involving the rth, sth, and n-r-sth harmonic components, the following relations apply:

$$q_{n\chi 3} = q_{r\chi} + q_{s\chi} + q_{n-r-s\chi} \quad , \tag{6.31}$$

$$q_{n\xi 3} = q_{r\xi} + q_{s\xi} + q_{n-r-s\xi} \quad , \tag{6.32}$$

$$\theta_{n3} = \sin^{-1}\left[(1/n) \, (r \sin \theta_r + s \sin \theta_s + (n-r-s) \sin \theta_{n-r-s})\right] \quad , \tag{6.33}$$

and

$$\Psi_{n3} = \tan^{-1}\left(\text{Re}\left[q_{n\xi\,3}\right] / \text{Re}\left[q_{n\chi 3}\right]\right) \ . \tag{6.34}$$

The third order incident wave field is identically zero because the nonlinearity of the air has been neglected. The subscript 3 attached to variables in the following discussion indicates that they apply to the third order solution. In many cases we will study, the travel directions and wave numbers for the third order waves are redundant with those of the first; but in order to be sufficiently general, the explicit expressions are given.

It is clear from Eq. (6.10) that the third order transmitted field is nonzero for at least some harmonic components of an intense wave. Since the same boundary conditions apply for all orders of the solution, it is necessary that a component generated in the material by nonlinear effects must be balanced by a component in the air, which then radiates from the surface. This means that the reflected wave field carries with it the imprint of the nonlinear interaction which takes place inside the material. Observations made by Zorumski and Parrot[27] corroborate this prediction: while studying the reflection and transmission of sound through thin porous sheets, they observed that the reflected wave field for an incident pure tone contained a strong third harmonic.

The first nonlinear case we consider is that of an intense pure tone incident on the material at some angle $\theta_1$, as depicted in Fig. 6-2.[†] The transmitted fundamental follows the angle $\Psi_1$ which is determined from Eq. (6.26). The third order field contains two components: a correction to the fundamental proportional

---

[†] Circled numbers denote intense harmonic components.

122

lines of equal amplitude

lines of equal phase

$\odot_3$

$\odot_3$

$\psi_1 = 21.7°$

$\psi_{3,3} = 21.7°$

$\psi$

$\theta_1 = 45°$
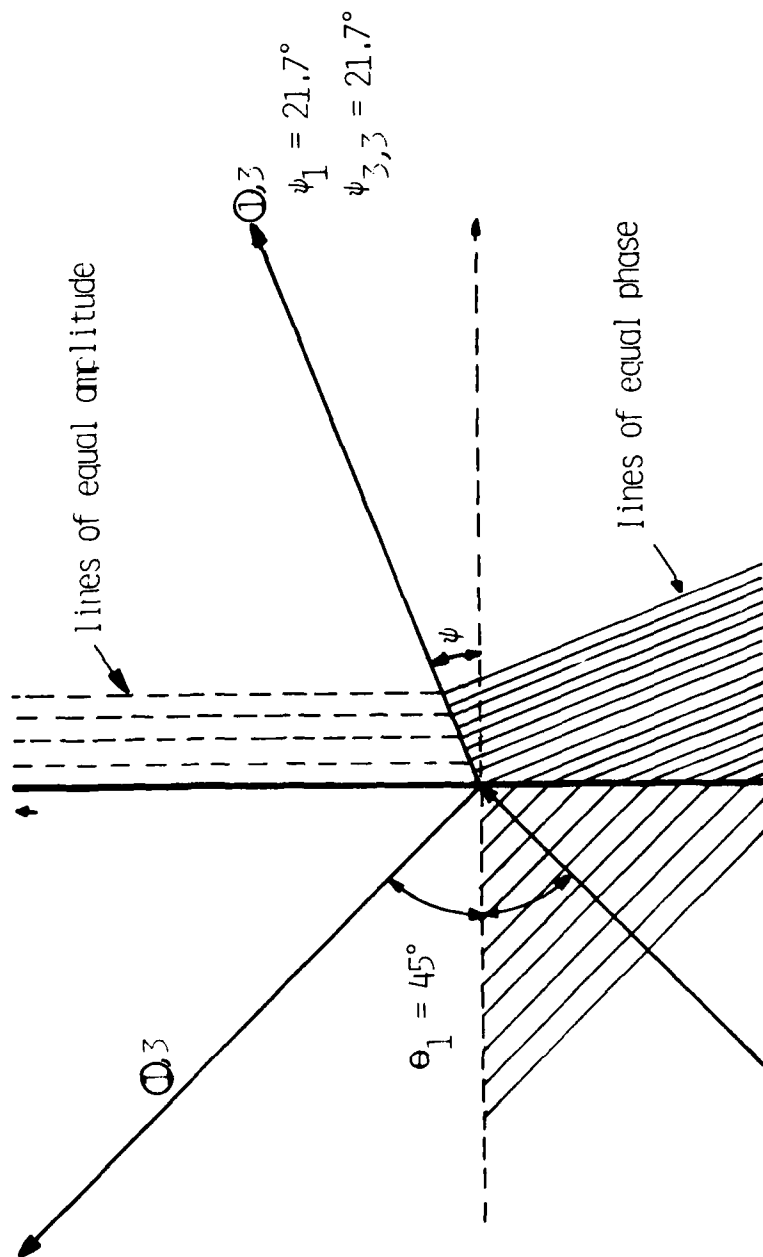
Figure 6-2

Reflection and transmission
of intense pure tone

AS-85-588

to $\varphi_1^2 \varphi_{-1}$ and a third harmonic distortion product which comes from $\varphi_1^3$. Distortion products such as these will be referred to as "products of self-interaction," because the nonlinear interactions by which they are produced involve only one frequency component. It is interesting to note that these distortion products travel in the same direction as the primary (in this case the fundamental) from which they originated. It is easily shown that

$$q_{3 \chi 3} = {}^3 q_1 \quad \text{and } q_{3 \xi 3} = {}^3 q_1 \quad \text{and therefore } \Psi_{33} = \Psi_1$$

and

$$q_{1 \chi 3} = q_1 \quad \text{and } q_{1 \xi 3} = q_1 \quad \text{and therefore } \Psi_{13} = \Psi_1 \, .$$

This leads to a second observation: products of self-interaction travel collinearly in the material with the primary from which they are generated. It is also of interest to note that the angle $\Psi_{33} \neq \Psi_3$. In other words, the nonlinearly produced third harmonic travels in a different direction from one that originates outside the material. Furthermore, the angle which the distortion products take on emerging from the material is equivalent to that for the emerging primary which energized them. This is easily seen from Eq. (6.33). If the solution were carried to higher order, all of the odd harmonics would be represented in the transmitted and reflected waves, and all would be collinear within and without the material.

The reflection coefficient of the fundamental is affected strongly by the material nonlinearity. In Eq. (3.41b) the predicted dependence of impedance magnitude on amplitude is given. Figure 6-3 shows the predictions of this equation and data obtained from Kuntz,[1] where the value of K has been selected to best fit the data. Our predictions are qualitatively borne out. With this in mind, we use Eq. (3.40b) using the fitted value of K to determine the normal incidence energy absorption coefficient as a function of SPL. Figure 6-4 is an illustration of the
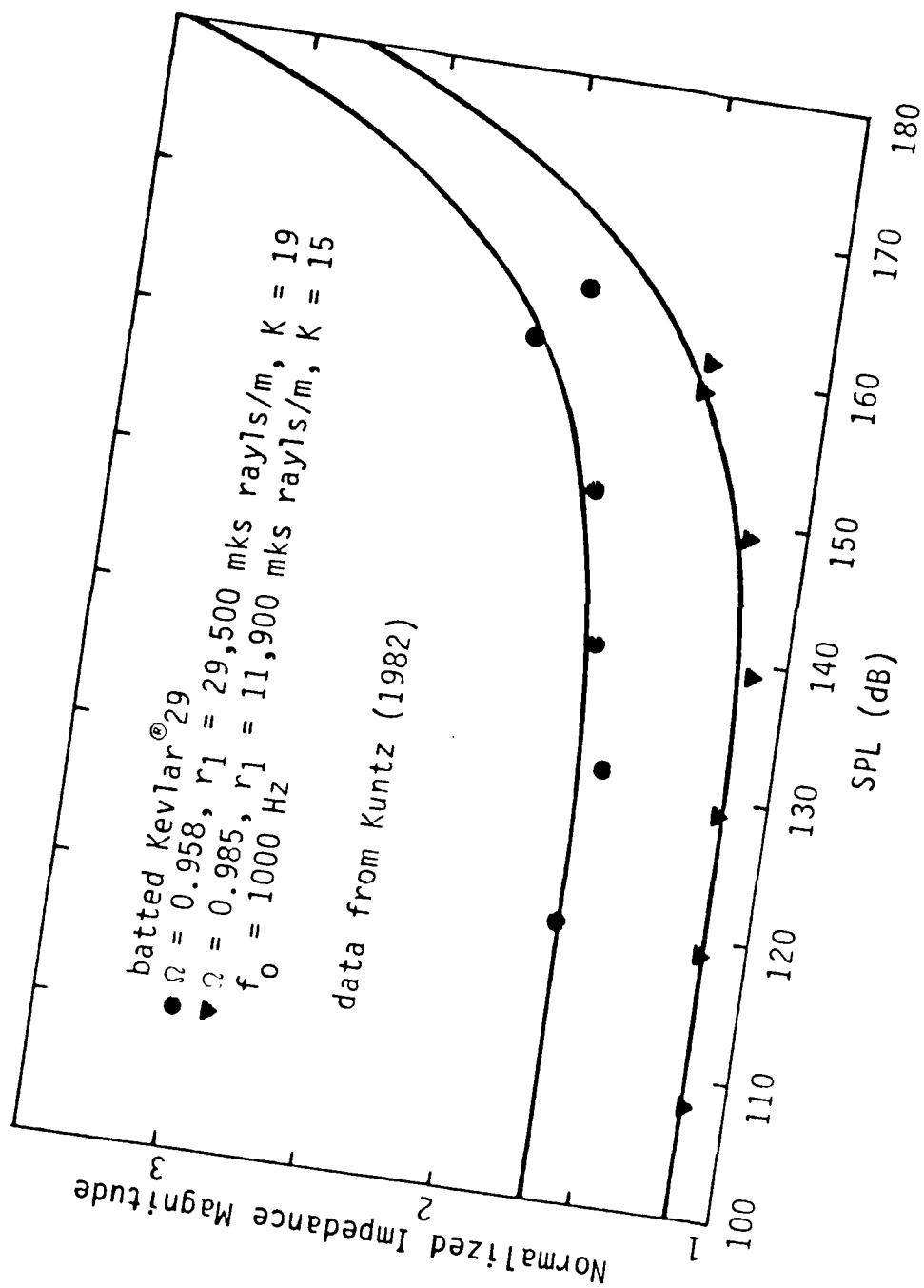
Figure 6-3

Impedance magnitude versus sound pressure level

batted Kevlar®29
● Ω = 0.958, $r_1$ = 29,500 mks rayls/m, K = 19
▼ Ω = 0.985, $r_1$ = 11,900 mks rayls/m, K = 15
$f_o$ = 1000 Hz

data from Kuntz (1982)

125
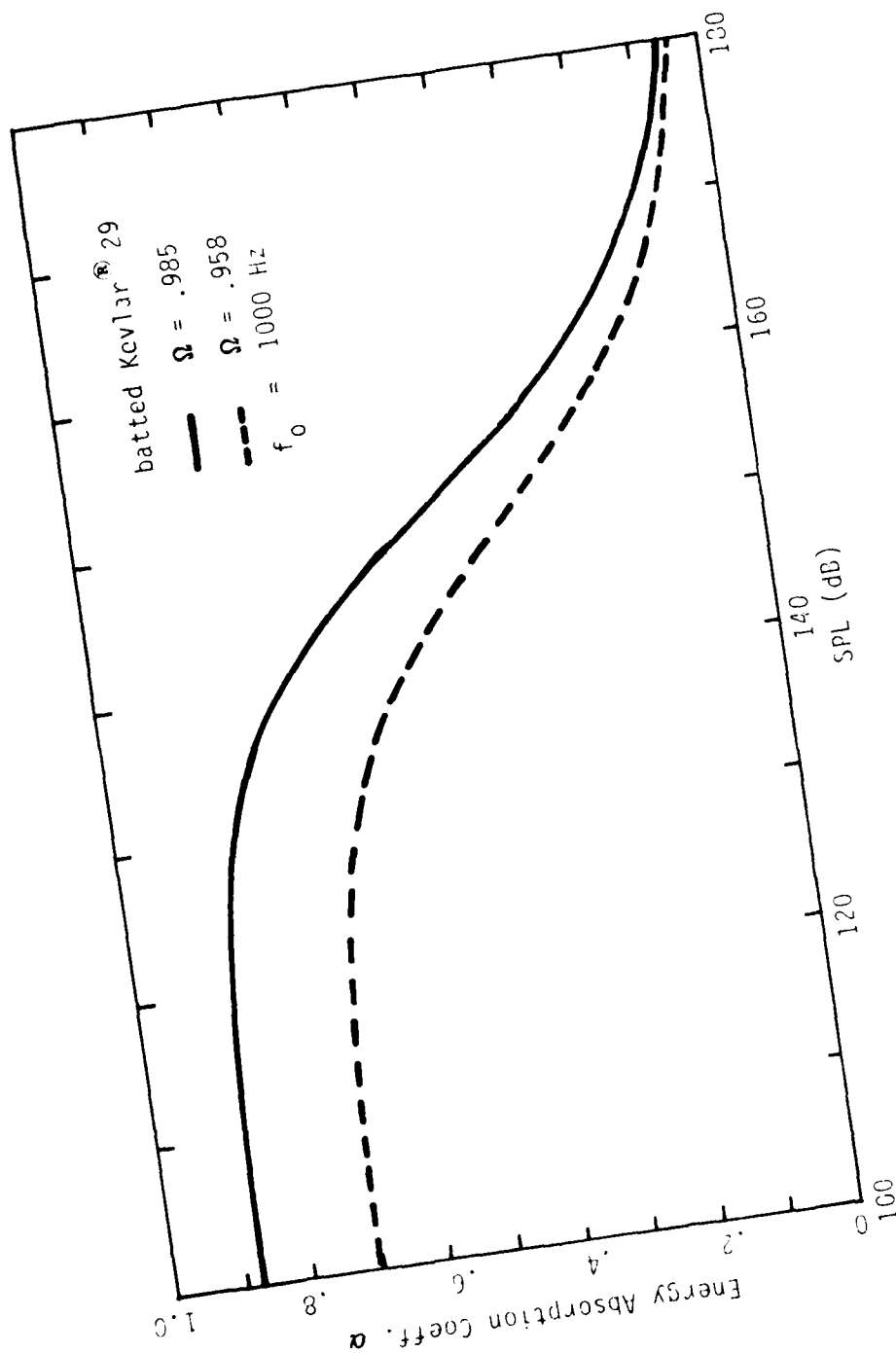
Figure 6-4
Normal incidence energy SPL
absorption coefficient versus SPL

severe deterioration of the absorber efficiency as the signal strength increases.

The second nonlinear case we discuss is that of an incident wave made up of two intense components (primaries): the fundamental and the second harmonic. Once again, these primaries travel into the material in the directions designated for linear behavior (see Fig. 6-5). This time, however, there are six components in the third order field. Each of the first six harmonic components is represented. The first and third qualify as products of self-interaction, and travel collinearly with the fundamental. Likewise, the second and sixth harmonics are direct products of the second harmonic, and travel collinearly with the second. The fourth and fifth harmonics, as products of a mutual interaction, do not travel either of these two paths; they travel instead in intermediate directions. These directions can be calculated rather easily. The fourth harmonic is a result of the product $\phi_1^2 \phi_2$, and has the wave numbers

$$q_{4\chi 3} = 2q_{1\chi} + q_{2\chi}$$

and

$$q_{4\xi 3} = 2q_{1\xi} + q_{2\xi} = \frac{4}{\sqrt{\gamma}} \sin \theta_1 \quad ,$$

which gives the propagation direction

$$\Psi_{43} = \tan^{-1}\left(\frac{(4/\sqrt{\gamma})\sin \theta_1}{\text{Re}[q_{4\chi 3}]}\right) \quad .$$

Likewise, the fifth harmonic is a result of the product $\phi_2^2 \phi_1$, and has these wave numbers and propagation directions

$$q_{5\chi 3} = q_{1\chi} + 2q_{2\chi}$$

$$q_{5\xi 3} = q_{1\xi} + 2q_{2\xi} = 5/\sqrt{\gamma}\sin \theta_1$$
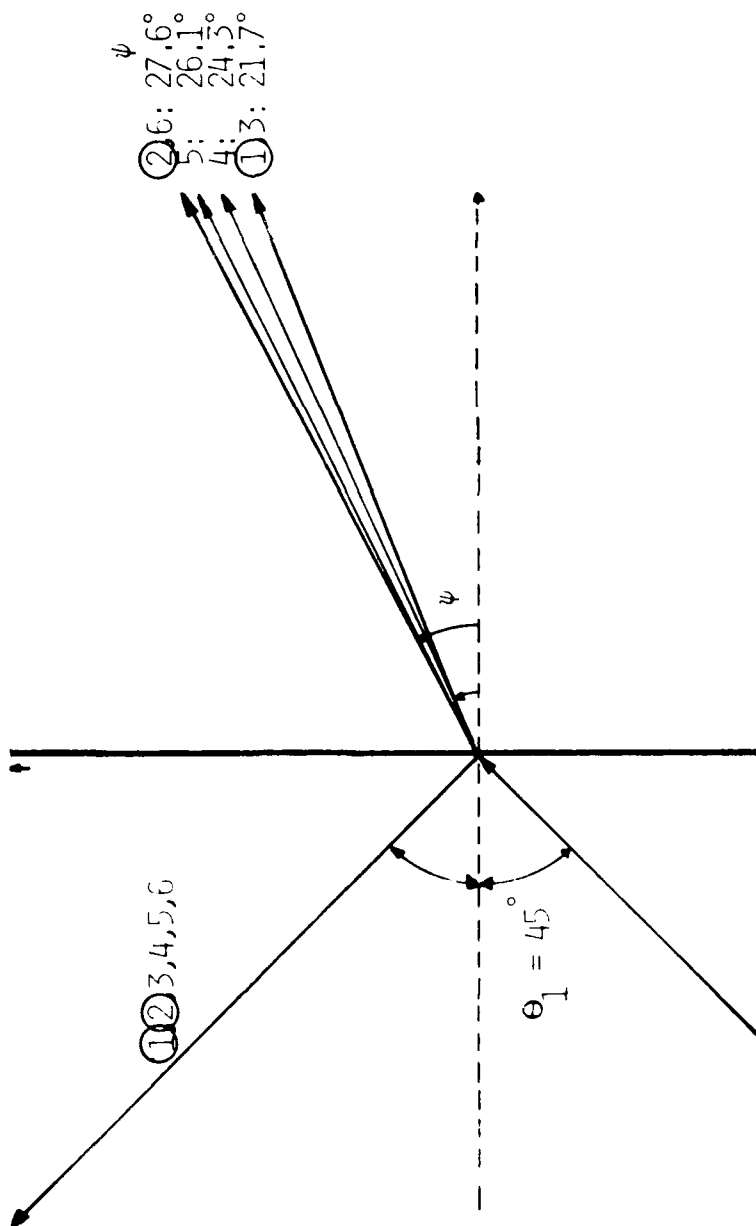
Figure 6-5

Reflection and transmission of
intense first and second harmonic

$\psi$

2 6: 27.6°
5: 26.1°
4: 24.5°
1 3: 21.7°

$\theta_1 = 45°$

1 2 3,4,5,6

AS-85-591

# APPENDIX A

## THERMAL EFFECTS ON SOUND SPEED

This Appendix contains an investigation of the frequency dependent effects on sound speed caused by heat conduction between the air and fibers. The bulk of this discussion parallels that given by Kuntz[1] in an appendix to his Ph. D. dissertation. Two assumptions are made: the wavelength is much larger than the fiber diameter, and the fluid flow around the cylinder is laminar. The wavelength assumption applies well beyond the range of audio frequencies and means that the pressure forcing function is uniform throughout the region of interest. The laminar flow assumption breaks down between 125 dB for $\Omega=.98$ and 135 dB for $\Omega=.94$ batted Kevlar[R] 29. Above this level the flow becomes turbulent and the primary mode of heat transfer is convection rather than conduction. In a turbulent flow the prevailing thermodynamic conditions are expected to be more isothermal than predicted for a laminar flow model.

The flow of heat to and from an individual cylindrical fiber is governed by the radial heat conduction equation

$$\frac{\partial^2 T}{\partial r^2} + \frac{1}{r}\frac{\partial T}{\partial r} - \frac{1}{\alpha}\frac{\partial T}{\partial t} = -\frac{dp/dt}{k}\exp(j\omega t) \quad , \tag{A.1}$$

diffusivities. The subscript f refers to quantities pertaining to the fiber, while the lack of a subscript indicates a quantity for air. Since the fiber is considered incompressible and the wavelength large the total pressure is independent of range and can be expressed as $\underline{p}=p\exp(j\omega t)+p_o$. In this case the radial heat equation is solved by

143

## E. Conclusions

Calculation of the dispersion and nonlinear effects caused by the material are complicated in vector notation, but addition of the inherent dispersion of a waveguide makes a perturbation solution extremely tedious. We have, however, managed to salvage an understanding of the gross effects of the nonlinearity on the absorptive power of the liner. Further study is recommended into solution of the modal wave number equations, and computational perturbation or finite-difference solution of the nonlinear problem.

value is determined by the initial intensity of the wave and the length of the duct, so that the absorption hovers in the vicinity of the maximum. An algorithm is therefore needed which integrates the total attenuation over a given length of lined ducting (since the absorptive power of the duct changes in space because of the decaying wave). We suggest a procedure which calculates the wave amplitude and corresponding liner impedance for successive small steps through the waveguide, and integrates the corresponding infinitesimal attenuations. The optimal valve would then have to be found on a trial and error basis, since no closed form optimization formula has been obtained thus far.
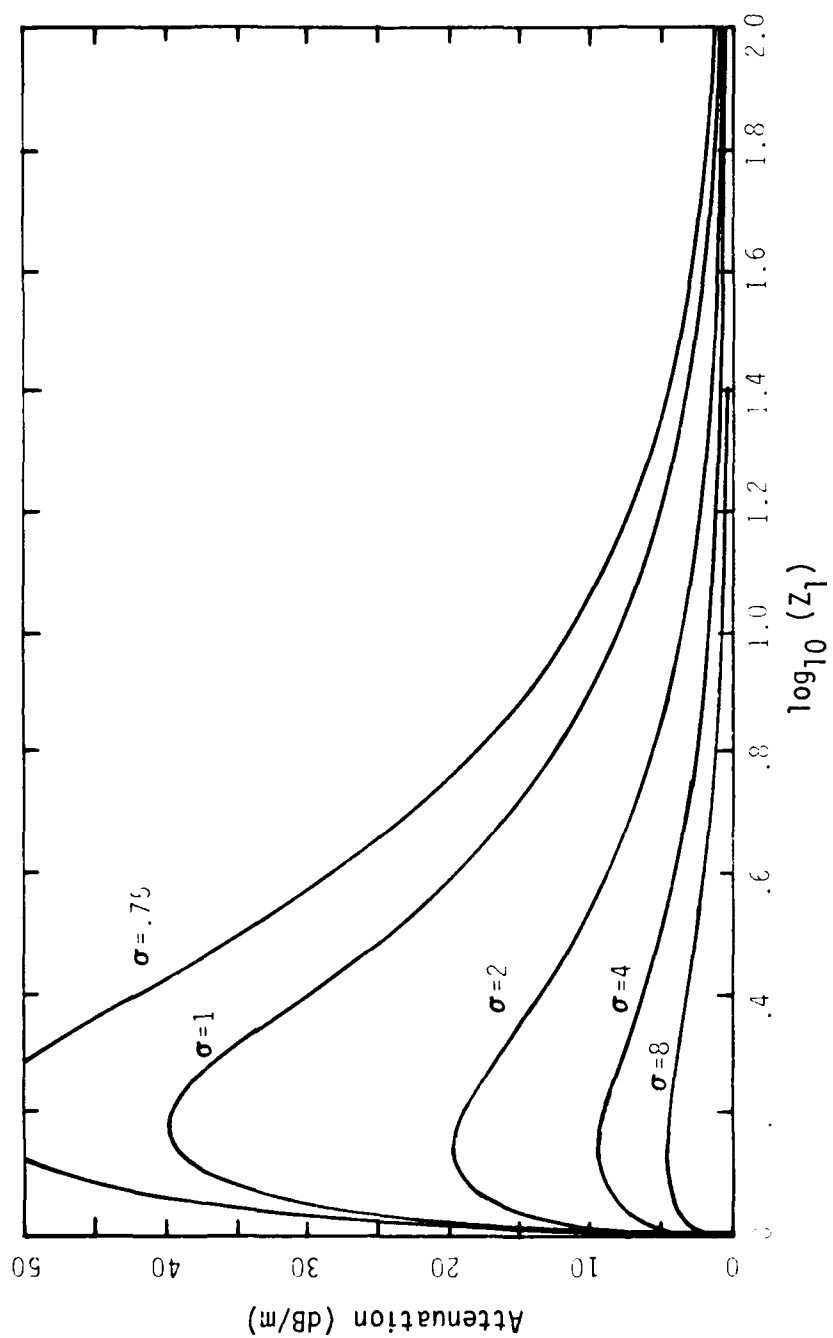
Figure 6-9

Attenuation versus liner impedance

AS-85-595

$$-\text{Im}(b) = \sqrt{\frac{(n^2/\gamma)(1+\sigma)\left((n^4/\gamma\,\Omega + \sigma|q_n|^4)\right)}{2\left(n^4/\gamma^2 + \sigma^2|q_n|^2\right)}\left(-1 + \sqrt{1 + \frac{\left((n^3/\gamma)\right)R_1\,\Omega}{n^4\,\Omega/\gamma + \sigma|q_n|^4}}\right)} \quad . \quad (6.49)$$

Figure 6-9 is a graph of the attenuation in dB/m which is plotted against the common logarithm of the normalized liner impedance. The graphs are parameterized against the fill ratio $\sigma$ . There is clearly an optimum liner impedance for a given fill ratio which yields the maximum absorption in the duct.

The magnitude of the characteristic impedance of the material has been shown to increase for an intense wave. We can get an idea of the resulting effect on attenuation by considering the pure tone expression for the characteristic impedance of the material, Eq. (3.41a), where K is based on $R_2$. An alternate expression of this is Eq. (B.11a) where the quadratic resistivity model is used. An approximation of the attenuation rate in the duct at a given point can be found by using the particle velocity magnitude in either of the above equations and reading the attenuation rate corresponding to this impedance value in Fig. 6-9.

It can be seen that increasing the amplitude of the wave does not always increase the absorption in the duct. In cases where the small-signal impedance is below the optimum, a high intensity wave generally is attenuated more rapidly than its linear counterpart. On the other hand, if the small-signal impedance is already too large, an increase in the amplitude of the wave simply brings a further deterioration in duct performance. Although this method of determining the attenuation of a duct is not highly accurate, it gives a useful mnemonic for the designer.

A duct should therefore be designed so that the small-signal impedance is below the optimum for a given fill ratio (which is usually determined by other physical constraints). The degree to which the impedance lies below the optimal

138

consider the nearly-plane wave mode where $a_{mn}L_A$ and $c_{mn}L_M$ are both much less than unity. In this case, the tangents in Eq. (6.39) can be replaced by their arguments to give

$$a^2 \approx \frac{-n^2}{\sigma \gamma q_n^2} c^2 \qquad (6.45)$$

where $\sigma = \dfrac{L_A}{\Omega L_M}$ is the fill ratio.

It is now possible to solve explicitly for a, b, c, and d, where the lack of a subscript denotes the nearly-plane wave mode. In essence we have assumed the duct to be acoustically narrow, and we must therefore keep in mind at all times the restriction to long wavelengths which we have imposed. If used for wider ducts, the calculations give attenuations which are much too large, since we have effectively neglected beaming. The expressions for the wave numbers are:

$$a^2 = \frac{n^2/\gamma \, (n^2/\gamma - q_n^2)}{n^2/\gamma + \sigma q_n^2} \quad , \qquad (6.46)$$

$$b^2 = d^2 = \frac{n^2/\gamma \, q_n^2 \, (1 + \sigma)}{n^2/\gamma + \sigma q_n^2} \quad , \qquad (6.47)$$

and

$$c^2 = \frac{\sigma q_n^2 \, (n^2/\gamma - q_n^2)}{n^2/\gamma + \sigma q_n^2} \quad . \qquad (6.48)$$

We are particularly interested in the value of $-\text{Im}(b)$, because it represents the attenuation of the wave as it travels down the duct:

$$\varphi_{mn3p}^{M} = \left( G_{m3p}^{M} \exp(-jc_{m3} \chi) + G_{m3p}^{M} \exp(jc_{m3} \chi) \right) \exp(-jd_{mn3} \xi) \qquad (6.43)$$

$$\varphi_{mn3H}^{M} = \left( G_{m3H}^{M} \exp(-jc_{mn3} \chi) + G_{m3H}^{M} \exp(jc_{mn3} \chi) \right) \exp(-jd_{mn} \xi) \qquad (6.44)$$

where the two homogeneous fields $(\varphi_{mn3H})$ exist for the purpose of satisfying the boundary conditions at $\xi = 0$. The wave numbers of the waves radiated into the air space are not generally those which fit the modes of the guide, hence this set of homogeneous modes is needed to balance the nonlinearly induced ones.

The harmonic interactions are calculated from Eq. (6.10), and expressions for the wave numbers and mode strengths are found by applying the boundary conditions. The number of calculations is potentially large: there will be $9M^2N^2$ interactions, where M is the number of modes considered and N the number of frequency components. Moreover, for each interaction a wave is produced which does not "fit" the guide and requires balancing at $\xi = 0$ by a homogeneous field which in general contains a full complement of M modes. The total number of contributions to the wave field is therefore $9M^3N^2$. This is truly forbidding, since the use of at least a few frequencies and several modes is essential to a realistic investigation of a wave propagating in a lined waveguide. For example, two frequency components with two modes apiece would require calculation of no less than 288 contributions. Nevertheless, we are only prevented from achieving this solution by the prodigious time and effort involved. As a research project in and of itself this calculation is well within the realm of possibility. However, the problem might be better solved using finite element techniques.

We are now forced to resort to bold approximations if we want to convey any information about the effects of the liner's nonlinearity on attenuation. We

136

$$\frac{\partial \varphi_{mn}^{M}}{\partial x}\bigg|_{x = L_M} = 0 . \tag{6.38}$$

The two new conditions represent the requirement that there be no normal velocity component at the walls. Upon applying the boundary conditions, we find the following equation for the wave numbers

$$a_{mn} \tan(a_{mn} L_A) = \frac{-\Omega n^2}{\gamma q_n^2} \; c_{mn} \; \tan(c_{mn} L_M) \quad , \tag{6.39}$$

where

$$a_{mn}^2 - c_{mn}^2 = \frac{n^2}{\gamma} - q_n^2 \tag{6.40}$$

and $b_{mn} = d_{mn}$. A major complication arises at this point because of three factors: tangents occur on both sides of Eq. (6.39), and the wave numbers are both complex and hyperbolically related. To our knowledge, the problem of determining the wave numbers has not been solved satisfactorily because numerical solutions of these simultaneous equations are extremely unstable. Standard practice seems to be to assume something about the duct liner, for instance, that it is locally reacting (see Cremer[29]). This simplifies the mathematics considerably. It becomes necessary at a later stage for us to make approximations as well, but for the moment we assume that the wave numbers can be found, and proceed with a third order solution for the duct. The following four wave fields are defined:

$$\varphi_{mn3p}^{A} = \left( G_{m3p}^{A} \exp(-ja_{m3} x) + H_{m3p}^{A} \exp(ja_{m3} x) \right) \exp(-jb_{mn3} \xi) \tag{6.41}$$

$$\varphi_{mn3H}^{A} = \left( G_{m3H}^{A} \exp(-ja_{m3} x) + H_{m3H}^{A} \exp(ja_{m3} x) \right) \exp(-jb_{mn} \xi) \tag{6.42}$$

135
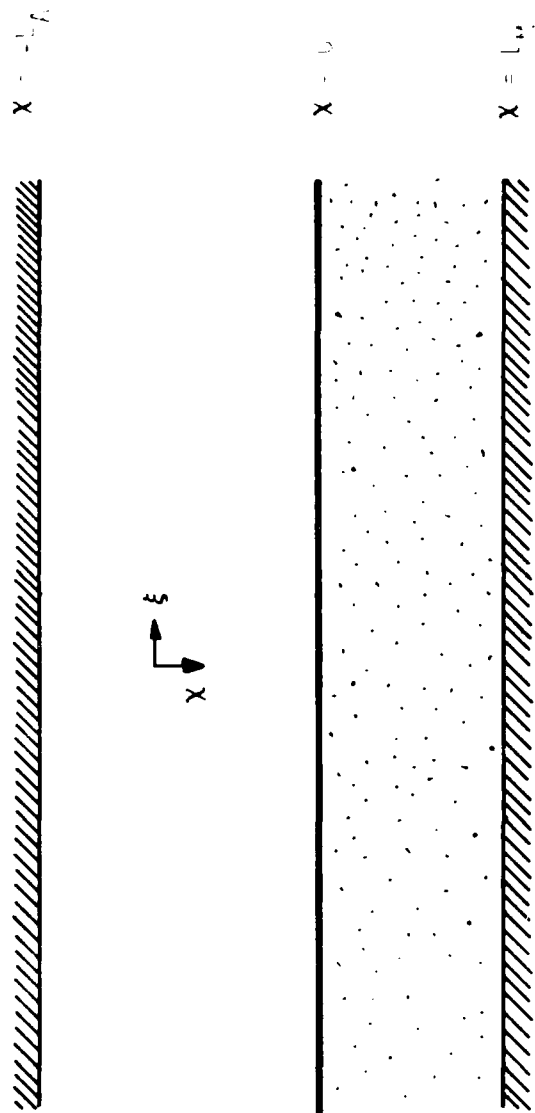
Figure 6-8
Two-dimensional waveguide geometry

the duct liner, and lastly to include the nonlinearity of the air as well. Unfortunately, this plan had to be curtailed considerably in the middle of the first phase: it is difficult or impossible to obtain general solutions for the modal wave numbers. After making some approximations, we arrive at an ad hoc model for calculating attenuation of a nearly-plane wave having wavelength much larger than the duct dimensions. A computational scheme is proposed to visualize the effects of liner nonlinearity on the absorptive efficiency of the duct. A computer algorithm is also suggested to calculate the optimal duct liner configuration.

We first define the waveguide geometry. The reader will recognize in Fig. 6-8 the axes from the reflection problem. The following derivation conforms roughly to those performed by Kurze and Ver[28] or Scott.[8] We define two wavefields, consisting of a wave traveling in each direction in both the air and material:

$$\phi^A_{mn} = \left(G^A_{mn} \exp(-ja_{mn}\chi) + H^A_{mn} \exp(ja_{mn}\chi)\right) \exp(-jb_{mn}\xi) \qquad (6.35)$$

and

$$\phi^M_{mn} = \left(G^M_{mn} \exp(-jc_{mn}\chi) + H^M_{mn} \exp(jc_{mn}\chi)\right) \exp(-jd_{mn}\xi) \quad , \qquad (6.36)$$

where

$$\phi = \sum \phi\, mn(\chi) \quad .$$

The wave numbers and modal solution will be defined by the previous two boundary conditions, Eqs. (6.18) and (6.19), plus

$$\left.\frac{\partial \phi^A_{mn}}{\partial \chi}\right|_{\chi=-L_A} = 0 \qquad (6.37)$$

and

133

The emergence angles are therefore equal to

$$\theta_{43} = \sin^{-1} \left( \frac{\sin \theta_1 + \sin \theta_2}{2} \right)$$

and

$$\theta_{53} = \sin^{-1} \left( \frac{\sin \theta_1 + 4 \sin \theta_2}{5} \right) .$$

We see that if noncollinear incident components interact within the material, the products of their mutual interaction in the reflected field will not propagate in either of the primary directions, but will adopt instead some intermediate direction.

The purpose of this discussion has been to understand in a practical way the nonlinear interaction in the material, and its effect on the wave fields inside and outside the material. In particular we have been interested in the wave numbers and propagation directions of the nonlinearly induced distortion products. The fact that signals can arrive from and depart in any direction from the material creates no difficulties in the reflection study. Difficulties arise, however, in the lined duct problem because wave numbers and propagation directions are rigidly linked by the waveguide. The nonlinearly induced waves in the waveguide guarantee that there is a certain amount of mode conversion. The resulting algebraic tedium of the perturbation solution of the lined duct problem renders it nearly useless.

## D. Lined Duct Problem

Our original plans to solve the lined duct problem by perturbation were very ambitious. We first intended to solve the small-signal problem of a nonlocally reacting liner. The theory was then to be expanded to include the nonlinearity of

132
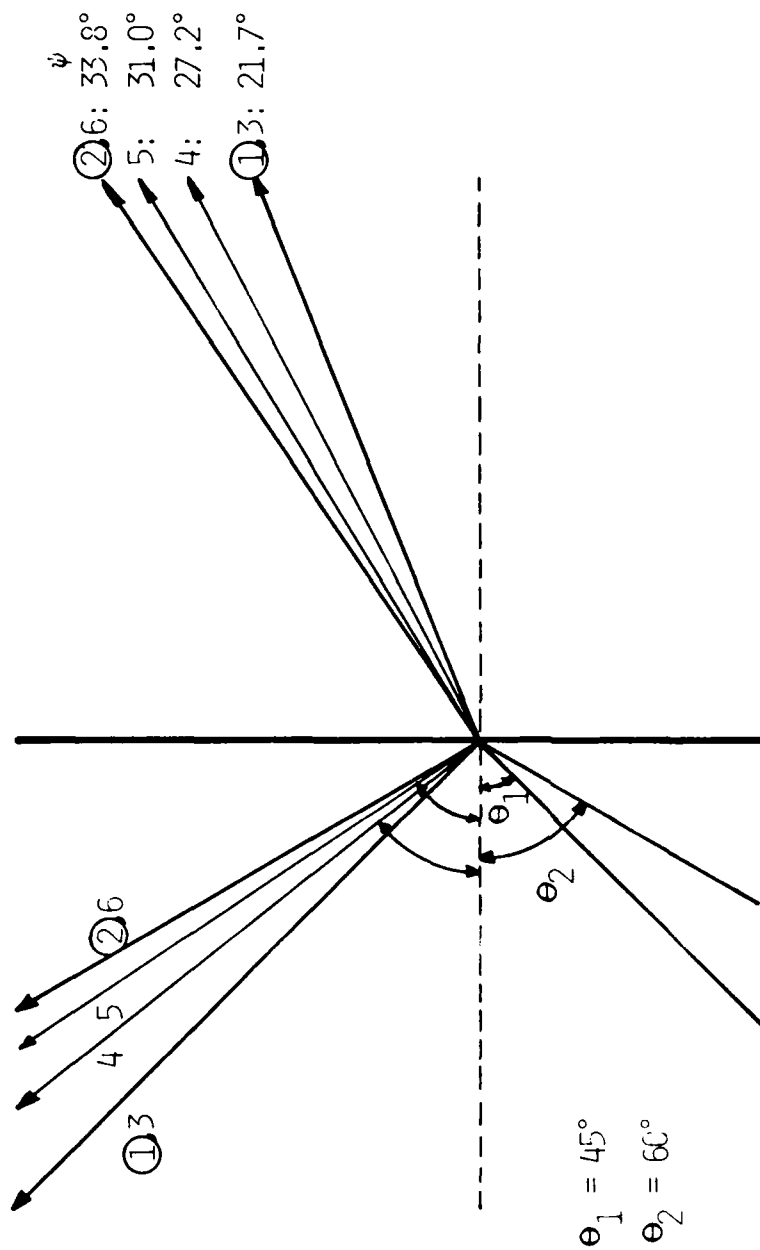
Figure 6-7

Reflection and transmission of
intense noncollinear first and second harmonic

AS-85-593
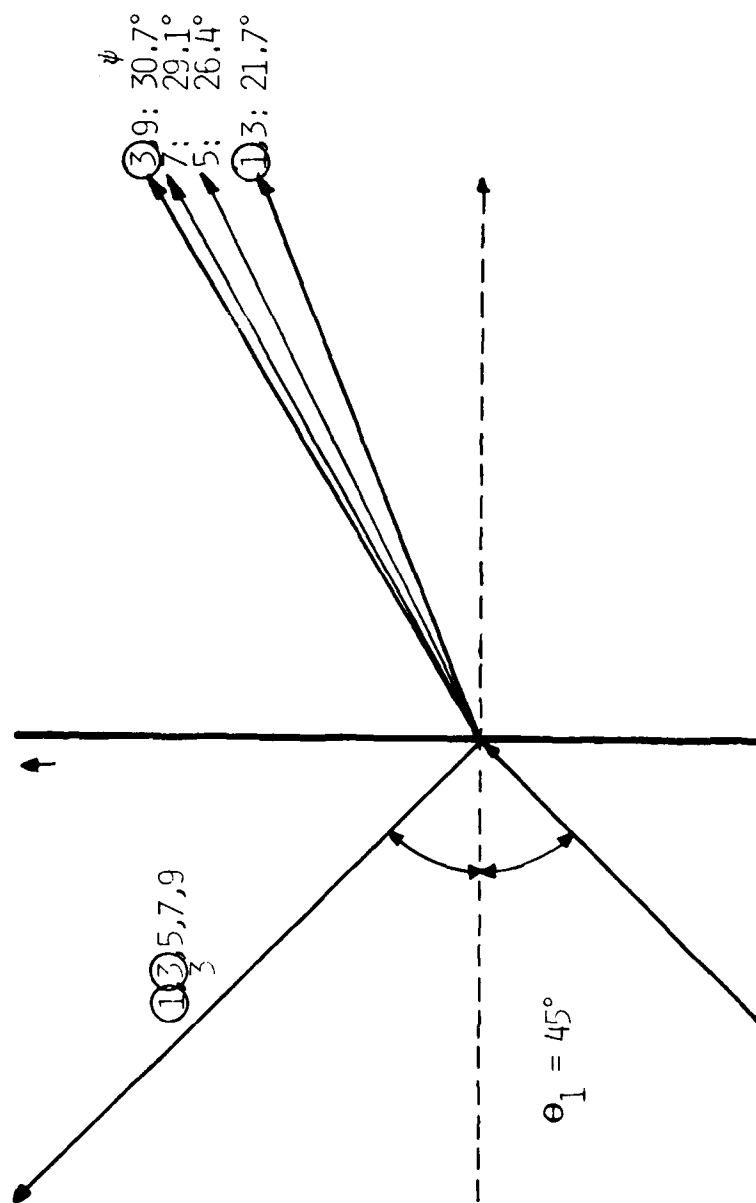
Figure 6-6

Reflection and transmission of
intense first and third harmonic

$\theta_1 = 45°$

| | $\psi$ |
|---|---|
| 9: | 30.7° |
| 7: | 29.1° |
| 5: | 26.4° |
| 3: | 21.7° |

AS-85-592

$$\Psi_{53} = \tan^{-1}\left(\frac{5/\sqrt{\gamma}\,\sin\theta_1}{\mathrm{Re}[q_{5X3}]}\right) .$$

Perhaps the most interesting point to note here is that despite the unusual direction of travel for the harmonics (relative to their linear paths) their reflected wave counterparts are still collinear with the first order reflected wave. This is easily verified from Eq. (6.33). This brings us to another principle: if the incident signal is collinear in the air, then neither the frequency-dependent refraction nor the nonlinear interaction between the noncollinear elements in the material prevents the reflected wave field from emerging in a collinear fashion.

A similar example is given in Fig. 6-6, where the case of an intense first and third harmonic incident on the material is shown. Qualitatively, this case is no different from the previous one, except that the third harmonic distortion product travels in a different direction from the incident third harmonic. The result is spatial interference patterns resembling Moire patterns.

The final example we consider is that of an intense first and second harmonic incident on the material, but this time at different angles $\theta_1$ and $\theta_2$. By all appearances Fig. 6-7 is no different qualitatively from the case in Fig. 6-5, but an important distinction appears in the reflected wave field: some of the wave components are no longer collinear with the incident primaries in the reflected wave. The reason for this is not difficult to show. The $\xi$-direction wave numbers for the fourth and fifth harmonics are

$$q_{4\xi 3} = \left(2/\sqrt{\gamma}\right)(\sin\theta_1 + \sin\theta_2)$$

and

$$q_{5\xi 3} = \left(1/\sqrt{\gamma}\right)(\sin\theta_1 + 4\sin\theta_2) .$$

129

$$\underline{T} = ( \, A \, I_0(r\xi) + B \, K_0(r\xi) - p/\rho_o c_p) \, \exp(j\omega t) + T_o \quad , \tag{A.2}$$

where $K_0$ and $I_0$ are modified Bessel functions of the first and second kinds, respectively, and $\xi = \sqrt{j\omega/\alpha}$. The specific heat $c_p$ should not be confused with the phase speed presented in Chapter 3. Since the thermal properties of the air and fiber are different we define two temperature functions, $\underline{T} = T \exp(j\omega t) + T_o$ for the air and $\underline{T}_f = T_f \exp(j\omega t) + T_o$ for the fiber. The subscript f will henceforth indicate a quantity appropriate for the fiber, while the lack of a subscript indicates a quantity for air. The temperature and heat flux are balanced at the wall of the fiber, $r=a$, and the following temperature distributions are found,

$$\underline{T} = \frac{p}{\rho_o c_p} \left( 1 - \frac{K_0(r\xi)}{D} \, \exp(j\omega t) \right) + T_o \quad , \tag{A.3}$$

$$r \geq a$$

where $D = K_0(a\xi) - \frac{k\xi}{k_f \xi_f} \left( \frac{K_0'(r\xi)}{K_0'(a\xi_f)} \right) I_0(a\xi_f)$ ,

and

$$\underline{T}_f = \frac{-p}{\rho_o c_p} \left( \frac{\dfrac{k\xi}{k_f \xi_f} \dfrac{K_0'(a\xi)}{I_0'(a\xi_f)} \, I_0(r\xi_f)}{D} \right) \exp(j\omega t) + T_o \quad , \tag{A.4}$$

$$r \leq a$$

The value of $K_0$ decays at large ranges, and $I_0$ decays as the range is reduced to zero. Temperature fluctuations are therefore largest far away from the fiber and are usually near zero at the center of the fiber. The region in between these ranges

144

contains two thermal boundary layers inside which the transition is accomplished and the thermal losses take place. The boundary layer outside the fiber has a thickness $\delta = \sqrt{2\alpha/\omega}$ and the layer inside the fiber, $\delta_f = \sqrt{2\alpha_f/\omega}$. The internal boundary layer is much thinner than the external one and can usually be neglected. It turns out that the thickness of the external boundary layer plays an important role in determining the sound speed because it influences the overall thermodynamic state of the fluid in the pores.

We now evaluate the average temperature fluctuation throughout a representative region of a fluid which is filled with a multitude of individual fibers. For this analysis we need only assume that the fibers are cylindrical and parallel. A spatial average of the value of T is taken over differential concentric circles between the fiber wall and some as yet unspecified integration radius $r_o$,

$$<T> = \frac{p}{\rho_o c_p} (1 - <F>) \quad , \tag{A.5}$$

where $F = \dfrac{K_o(r\zeta)}{D}$ and

$$<F> = \frac{1}{\pi(r_o^2 - a^2)} \int_a^{r_o} \frac{2\pi r K_o(r\zeta) dr}{D} \quad . \tag{A.6}$$

The result of the integral is

$$<F> = \frac{2}{\zeta(r_o^2 - a^2)} \left( \frac{r_o K_1(r_o\zeta) - a K_1(a\zeta)}{D} \right) \quad . \tag{A.7}$$

The average value of F is an indication of the overall thermodynamic state of the fluid in the pores. When $<F>=1$, conditions are isothermal and the temperature

145

fluctuations are very small. When $<F>$ is near zero, adiabatic conditions prevail and the effect of the fiber is negligible.

The integration distance is chosen so that the total integrated volume around all of the fibers is equivalent to the volume of fluid in the pores. It was found in Chapter 2 that the volume and area porosities are equivalent; the expression for the porosity can be written as

$$\Omega = 1 - C\pi a^2 \quad , \tag{A.8}$$

where C is the number of fibers per unit area and $\pi a^2$ the area of a cylindrical fiber. A circle of radius $r_o$ is centered on each fiber, so the percentage of the material volume falling within the integration radius is $C\pi r_o^2$. Upon eliminating C between the two equations, one finds that

$$\frac{r_o}{a} = \sqrt{\frac{\Omega}{1 - \Omega}} \quad . \tag{A.9}$$

Although not all of the fluid parcels are counted, a number of parcels are counted more than once to make up the difference. The resulting volume is presumed to be a good representative of the fluid.

The value of $<F>$ is now used to determine the average sound speed in the pores. The ideal gas law is written in modified form using spatial average values as

$$<\underline{p}> = <\underline{\rho}>R<\underline{T}> \quad , \tag{A.10}$$

where R is the difference of specific heats $c_p - c_v$. This equation can be written as

$$P_o + <p>\exp(j\omega t) = \left(\rho_o + <\rho>_1 \exp(j\omega t)\right) R \left(T_o + <T>\exp(j\omega t)\right) \quad , \tag{A.11}$$

146

where the total density has been expanded as were the total pressure and temperature. The "ambient" terms cancel out $(p_o = \rho_o R T_o)$ and we neglect the second order term. The result is

$$<p> = R(<\rho> T_o + \rho_o <T>) \quad . \tag{A.12}$$

Since the expression for $<T>$ is already known, we substitute it into Eq. (A.12) to find

$$<P> = \frac{R T_o}{1 + R/c_p (1 - <F>)} \quad . \tag{A.13}$$

We define the average sound speed $<c>$ as $\sqrt{d<p>/d<\rho>}$. Since the term in brackets in Eq. (A.12) is simply a constant, the differentiation is simple and $<c>$ is clearly

$$<c> = \frac{c_o}{\sqrt{1 + (\gamma - 1)<F>}} \quad , \tag{A.14}$$

where $\gamma = 1.4$ (for air) is the ratio of specific heats $c_p/c_v$. This is nearly the result obtained by Kuntz;[1] the only difference is the choice of integration radius. A general discussion of the results of this equation has already been given in Chapter 2, B.4.

In this analysis it is assumed that the external boundary layers of adjacent fibers do not interact. At very low frequencies, however, the boundary layers become very large. In this case the temperature solution, on which the calculation for $<c>$ is based, is no longer valid. We define a criterion frequency, below which the calculated value from Eq. (A.14) cannot be trusted, as the frequency at which the boundary layers of the fibers are predicted to intersect the centers of adjacent

147

fibers. The fiber radius a is usually known for a given material; for Kevlar it is $6 \cdot 10^{-6}$ m. The expression for $\delta$ has been given previously and is $\sqrt{2\alpha/\omega}$ where $\alpha = 2.2 \cdot 10^{-5}$ m$^2$/sec is the thermal diffusivity of air under standard conditions. To find the inter-fiber spacing, we return to Eq. (A.8), where the average number of fibers per unit area, $\sqrt{C}$, is defined. The inter-fiber spacing is simply $1/\sqrt{C}$, the "distance per fiber",

$$s = a\sqrt{\frac{\pi}{1 - \Omega}} \; . \tag{A.15}$$

Our criterion can be written as $s = a + \delta$. We first solve for the critical $\delta$ at which the criterion is reached,

$$\delta = \left( a\sqrt{\frac{\pi}{1 - \Omega}} - 1 \right) \quad . \tag{A.16}$$

We then solve for the angular frequency

$$\omega = \frac{2\alpha}{a^2 \left( \sqrt{\frac{\pi}{1 - \Omega}} - 1 \right)^2}$$

and the physical frequency $f_{th}$ below which the solution is inaccurate,

$$f_{th} = \frac{\alpha}{\pi a^2 \left( \sqrt{\frac{\pi}{1 - \Omega}} - 1 \right)^2} \; . \tag{A.17}$$

The actual sound speed in the pores is expected to be closer to isothermal than would be calculated from Eq. (A.13) for frequencies below $f_{th}$. For the three porosities of Kevlar used in our experiments, the frequencies are

$$\Omega = .98 \qquad 1462 \, Hz \quad,$$

$$\Omega = .96 \qquad 3147 \, Hz \quad, and$$

$$\Omega = .94 \qquad 5002 \, Hz \quad.$$

Figure A-1 is included for the reader's convenience and is merely a reprint of Fig. 2-2. It shows that the sound speed tends towards the isothermal value in the middle of the audio band. The actual sound speed value is, however, closer to the isothermal value than predicted by Eq. (A.14) for frequencies below $f_{th}$. Moreover, at high intensity the sound speed is closer to isothermal for all frequencies because of turbulent mixing in the fluid. Since we are most interested in measurements taken below $f_{th}$ and above 135 dB, we are justified in assuming the sound speed to have the isothermal value.
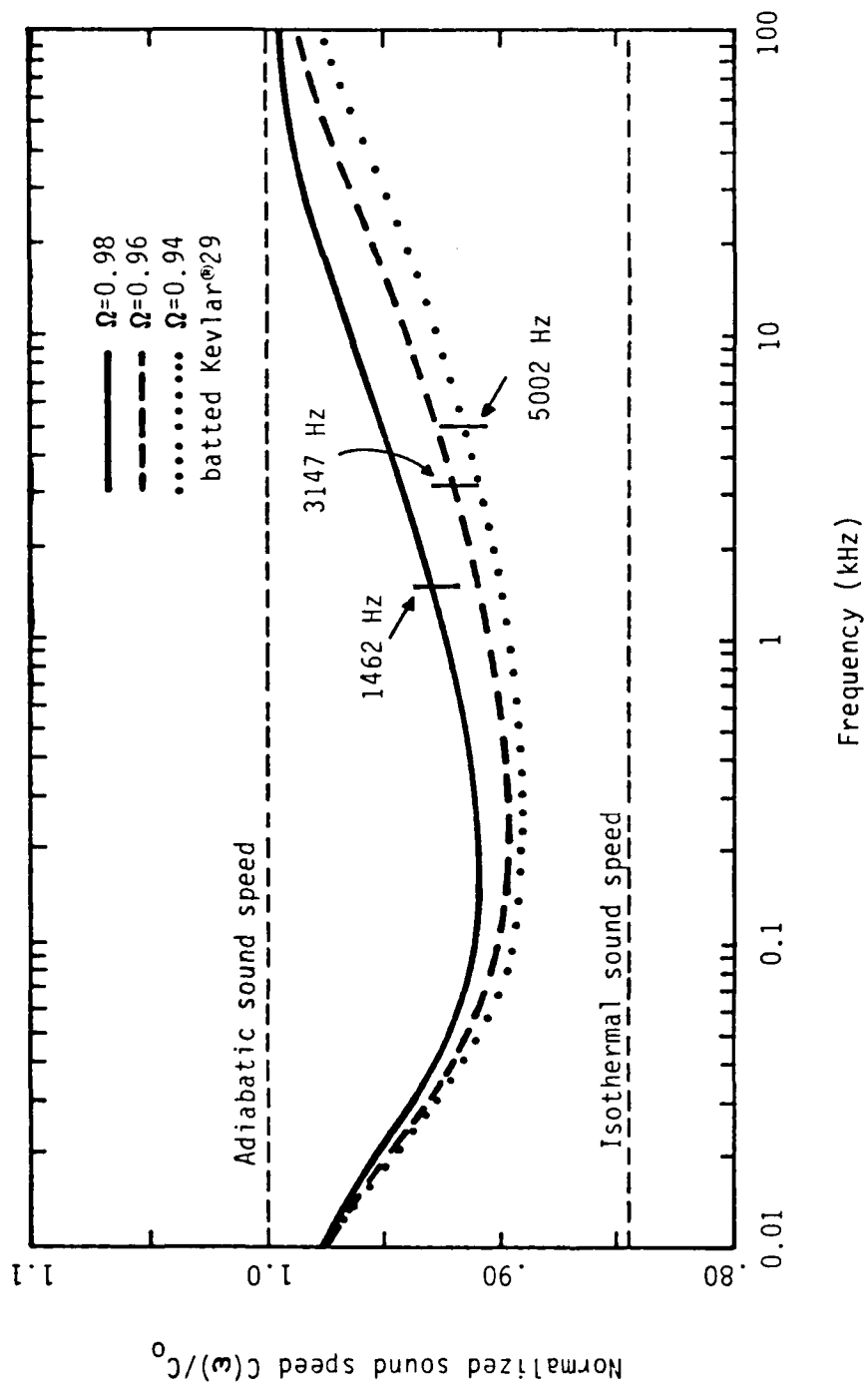
Figure A-1

Frequency-dependent sound speed

AS-85-596

## Appendix B

## RELATIONS FOR QUADRATIC RESISTIVITY

The quadratic resistivity function $r=r_1+r_3u^2$ was not used in the bulk of this investigation because the $r_1+r_2u\,sgn(u)$ model was observed to fit the static flow resistivity data better. The two models, however, closely approximate one another for most of the flow velocities used in the static flow resistivity measurements. This is to be expected, since both curves are intended to mimic the same set of data. Figure B-1 shows corrected measured resistivity data and the fitted curves for the two resistivity models. This figure is the same as Fig. 2-1 and is presented here for the convenience of the reader. The values of the two resistivity functions are close over the measured range. However, the two curves rapidly diverge above this range. Table B-1 gives the fitted values of $r_1$ and $r_3$ and the ratio of the mean-squared errors for the seven samples tested in this study.

Table B-1

| Sample | $\Omega$ | $r_1$ (rayl/m) | $r_3$ (raylsec$^2$/m$^3$) | MSE ratio |
|--------|------|---------|-------------|-----------|
| 1 | 0.94 | 51007 | 4260 | 1.04 |
| 2 | 0.98 | 11214 | 1302 | 1.86 |
| 3 | 0.96 | 30700 | 4195 | 1.18 |
| 4 | 0.94 | 53031 | 8839 | 1.42 |
| 5 | 0.96 | 29497 | 4291 | 1.38 |
| 6 | 0.94 | 54394 | 6995 | 1.40 |
| 7 | 0.96 | 29727 | 3393 | 1.70 |
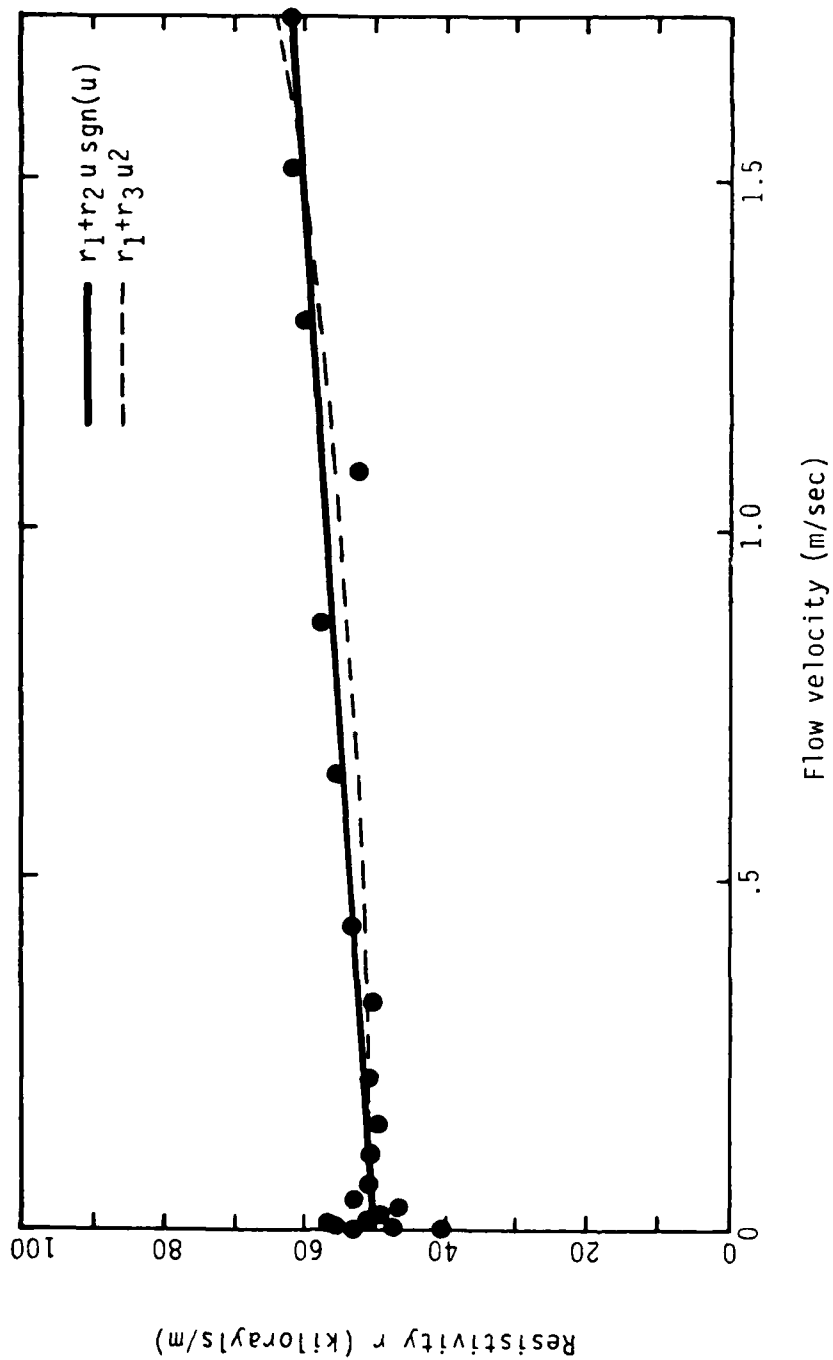
Figure B-1

Measured static flow resistivity data
and empirically fitted curves

AS-85-597

The quadratic resistivity model has one definite advantage: the resulting cubic nonlinear term in the wave equation lends itself more readily to analytical study than the corresponding $u^2 \text{sgn}(u)$ term. We therefore present the following results in preparation for a planned perturbation solution for a high intensity sound field in a lined duct.

The Helmholtz relations based on the quadratic resistivity model have the cubic nonlinearity form

$$V'_n + jq_n V_n = \frac{-n\Omega R_3}{2q_n} \sum_p \sum_q V_p V_q V_{n-p-q} \quad , \tag{B.1}$$

where $R_3 = r_3 c_i^2 / \rho_o \omega_o \Omega$. If the harmonics of the signal are assumed to have a negligible effect on the fundamental, we assume that only $V_1$ and $V_1{}^*$ are important terms in the convolution. Equation (B.1) becomes

$$V'_1 + jq_1 V_1 = - \frac{\Omega R_3}{2q_1} V_1(V_1 V_1^* + V_1^* V_1) + V_1^*(V_1 V_1) \quad , \tag{B.2.a}$$

which reduces to

$$V'_1 + jq_1 V_1 = - \frac{3\Omega R_3}{2q_1} V_1 V_1 V_1^* \quad . \tag{B.2.b}$$

This equation can be written in A, $\phi$ notation (see Chapter 3) as

$$A'_1 + j(q_1 - \phi'_{v1})A_1 = - \frac{3\Omega R_3}{2q_1} \frac{A_1^3}{4} \quad . \tag{B.3}$$

153

Once again the real and imaginary parts separate to give

$$A'_1 + q_{1i}A_1 = -K_3 q_{ir} A_1^3 \quad , \tag{B.4}$$

and

$$q_{1r} - \phi'_{v1} = -K_3 q_{1i} A_1^2 \quad , \tag{B.5}$$

where

$$K_3 = \frac{3R_3}{8\sqrt{1 + R_1^2}} \quad . \tag{B.6}$$

The solutions of this equation are similar in form to the ones generated for the other model in Chapter 3.

$$A_1(X) = \frac{A_1(0) \exp(-q_{1i}X)}{\sqrt{1 + \Gamma_3 \left(1 - \exp(-2q_{1i}X)\right)}} \quad , \tag{B.7}$$

$$\text{where } \Gamma_3 = \frac{K_3 A_1^2(0)}{Q_1}$$

$$C_{v1} = \left(q_{ir} + K_3 q_{1i} A_1^2\right)^{-1} \quad , \tag{B.8}$$

$$Z_1 = q_1 - jK_3 A_1^2 q_1^* \quad , \tag{B.9}$$

$$\phi_{z1} = \tan^{-1}\left(\frac{q_{1i} + K_3 q_{1r} A_1^2}{q_{1r} + K_3 q_{1i} A_1^2}\right) \quad , \tag{B.10}$$

$$|Z_1| = \left(|q_1|^2(1 + K_3^2 A_1^4) + 2R_1 K_3 A_1^2\right)^{1/2} \quad , \tag{B.11a}$$

154

which can be approximated by

$$|z_1| \simeq |q_1|(1 + K_3 A_1^2) \quad , \tag{B.11b}$$

where

$$C_{p1} = \left[ q_{1r} + K_3 q_{1i} A_1^2 - \frac{2q_{1i} Q_1 C_3 \exp(-2q_{1i}x)}{Q_1 2 + \left(1 - C_3 \exp(-2q_{1i}x)\right)^2} \right]^{-1} \tag{B.12}$$

$$C_3 = \frac{(1 - Q_1^2)\Gamma_3}{1 + \Gamma_3} \quad .$$

There is very little quantitative difference between the solutions of these expressions and those derived in Chapter 3 if the particle velocity amplitude lies in a range where the resistivity functions have similar values. As an example, the velocity at which the two curves cross in Fig. B-1 is 1.45 m/sec. Above this velocity the value of the resistivity function for the quadratic model exceeds that for the sgn(u) model, and the resistivity curves rapidly diverge for high velocities. For a 1 kHz tone in $\Omega = 0.96$ batted Kevlar[R] 29, a 1.45 m/sec particle velocity corresponds to an SPL of 153.9 dB. Solutions of these equations for signals weaker than 153.9 dB (in this particular case) are therefore expected to be nearly equivalent to those in Chapter 3.

The numerical solution of Eq. (B.1) involves a mere two line code change in the existing computer program (see Appendix C). The successive approximation for the harmonic impedances is less stable in the quadratic resistivity case because of the higher power of u involved. The successive approximation algorithm may be unable to converge for high intensity signals, in which case the propagation curves are never generated. It turns out, however, that the algorithm is stable for virtually

all boundary conditions that do not exceed the aforementioned amplitude limit. Figure B-2 contains a comparison of predicted and measured harmonic amplitudes. The data plotted here are the same as contained in Fig. 4-12. Since the solutions for the two models are nearly equivalent we have no qualms about using $r_3 u^2$ in place of $r_2 u \, \text{sgn}(u)$ within the stated restrictions on amplitude.
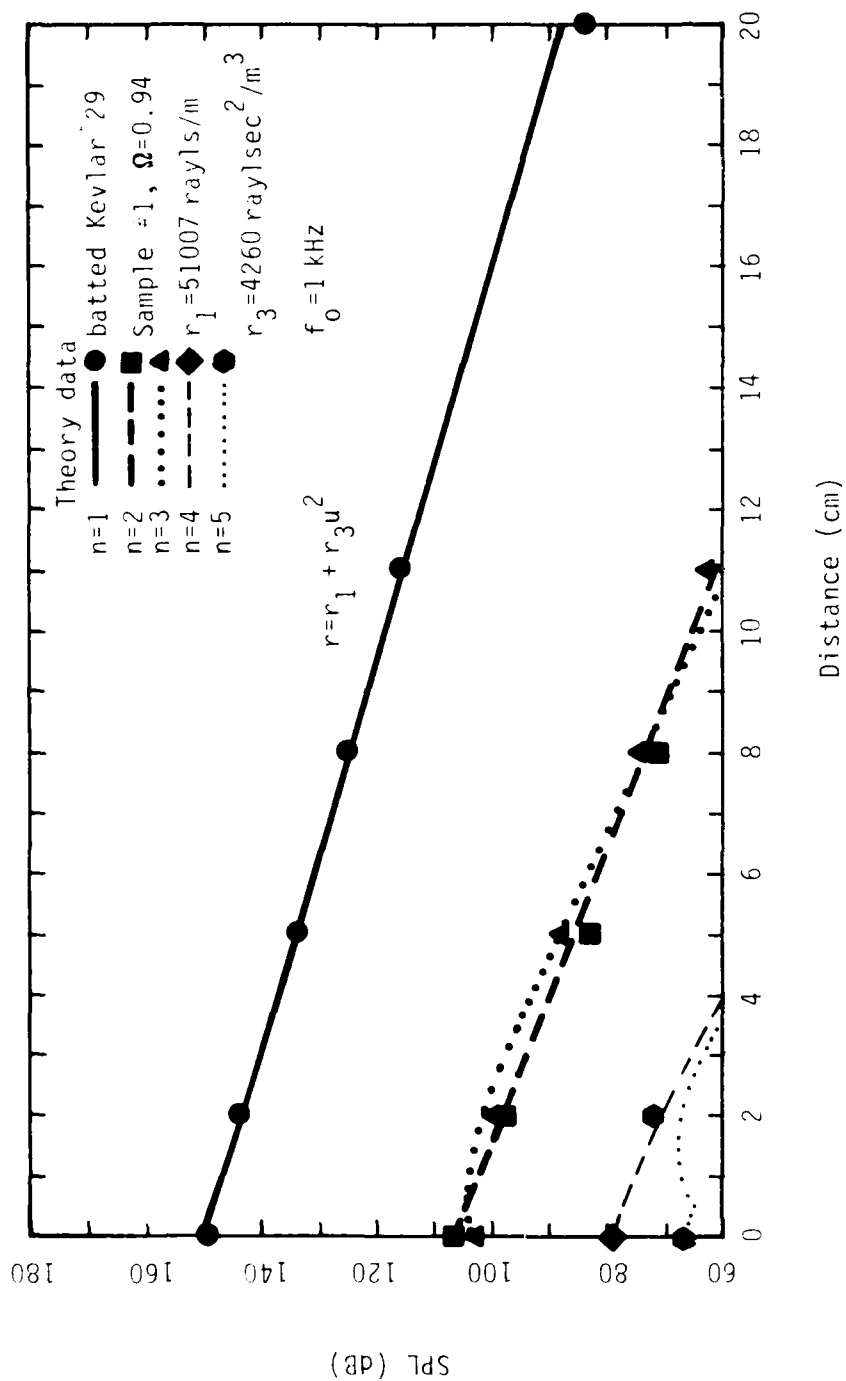
Figure B-2

Comparison of measured and predicted harmonic SPL versus distance for the quadratic resistivity model, sample 1

AS-85-598

DISTRIBUTION LIST

Copy No.

NASA Lewis Research Center
21000 Brookpark Road
Cleveland, OH 44135
1 - 3  Attn:  E. J. Rice, Mail Stop 5-7
4          K. J. Baumeister, Mail Stop 5-7
5          J. A. Saggio, Mail Stop 500-313
6          Report Control Office, Mail Stop 60-1
7 - 8      Library, Mail Stop 60-3

NASA Scientific and Technical Information
 Facility
P. O. Box 3757
Baltimore/Washington International Airport
Baltimore, MD 21240
9 - 13  Attn:  Accessioning Department

NASA Langley Research Center
Acoustics and Noise Reduction Division
Hampton, VA 23145
14 - 20  Attn:  W. E. Zorumski, Mail Stop 460
          W. Watson, Mail Stop 460
          W. L. Willshire, Mail Stop 460
          T. L. Parrott, Mail Stop 460
          H. Lester, Mail Stop 463
          David Chesnut, Mail Stop 460A
          J. C. Yu, Mail Stop 460

NASA Ames Research Center
Mail Stop 247-1
Moffett Field, CA 94035
21 - 22  Attn:  Cahit Kitaplioglu
          Marianne Mosher

Commanding Officer
Office of Naval Research
Arlington, VA 22217
23      Attn:  L. Hargrove (Code 412)

24 - 36  Defense Technical Information Center
Cameron Station
Alexandria, VA 22314

ASAPL-DO
Wright-Patterson AFB, OH 45433
37      Attn: E. E. Bailey

Aeroacoustics Group
AFWAL/FIBGD
Wright-Patterson AFB, OH 45433-6553
38      Attn: R. Shimovetz

U. S. Army Construction Engineering
 Research Laboratory
Box 4005
Champaign, IL 61820
39      Attn:  R. Raspet

Wesen-B
USAE Waterways Expt. Station
Vicksburg, MS 39180
40      Attn:  K. Attenborough

New London Laboratory
Naval Underwater Systems Center
New London, CT 06320
41      Attn:  M. B. Moffett

Jet Propulsion Laboratory
4800 Oak Grove
Pasadena, CA 91103
42      Attn:  T. G. Wang

Lockheed-Georgia Company
B/72-74 Z/403
86 South Cobb Drive
Marietta, GA 30063
43      Attn: Krish Ahuja

Continuum Dynamics, Inc.
P. O. Box 3073
Princeton, NJ 08540
44      Attn: Donald Bliss

Copy No.

General Electric Company
Aircraft Engine Business Group
Mail Drop G-43
1 Neumann Way
Box 156301
Cincinnati, OH 45215-6301
45      Attn  Patrick Y. Ho

Boeing Commercial Airplane Company
Mail Stop 9W-65
P. O. Box 3707
Seattle, WA 98124
46      Attn:  C. G. Hodge

McDonnell Douglas Research Labs
Dept. 22, Bldg. 110, MS-4
P. O. Box 516
St. Louis, MO 63166
47      Attn: Valdiz Kibens

Lockheed Missiles and Space Company
111 Lockheed Way, Bldg. 104
Org. 62-62
Sunnyvale, CA 94086
48      Attn  Y. A. Lee

Hamilton Standard Division
United Technologies Corporation
MS 1A-3-6
Windsor Locks, CT 06096
49      Attn:  Bernard Magliozzi

Pratt and Whitney Aircraft
Mail Stop 116-01
400 Main Street
East Hartford, CT 06108
50      Attn: Douglas C. Mathews

Wyle Labs
128 Maryland St.
El Segundo, CA 90245
51      Attn:  Louis C. Sutherland

Sikorsky Aircraft Division
Sept. 4045 Aeromechanics Branch
North Main Street
Stratford, CT 06602
52      Attn  R. K. Shenoy

Southwest Research Institute
P. O. Drawer 28510
San Antonio, TX 78284
53      Attn:  James F. Unruh

Northrop Corporation, ASD
8900 East Washington Boulevard
Pico Rivera, CA 90660-3737
54      Attn  R. E. Kraft (E122/3E)

Hersh Acoustical Engineering
9545 Cozycroft Ave.
Chatsworth, CA 91311
55      Attn:  A. S. Hersh

Hoover Keith and Bruce Inc.
11381 Meadowglen, Suite 1
Houston, TX 77082
56      Attn:  H. L. Kuntz

Nelson Industries
Box 428
Stoughton, WI 53589
57      Attn:  P. Thawani

Tracoustics, Inc.
P. O. Box 3610
Austin, TX 78764
58      Attn:  J. Schmitt

Embry-Riddle Aeronautical University
Regional Airport
Daytona Beach, FL 32014
59      Attn  Howard V. L. Patrick

!9.     L. Cremer, "Nachhallzeit und Daumpfungmass bei streifendem Einfall," Akustiche Zeitschrift 5, 57-76 (1940).

14. A. S. Hersh and B. Walker, "Acoustic behavior of fibrous bulk materials," presented at the AIAA 6th Aeroacoustics Conference, Hartford, CT, Paper #80-0986 (1980).

15. M. A. Biot, "Generalized theory of acoustic propagation in porous dissipative media," J. Acoust. Soc. Am. 34, 1254-1264 (1962).

16. R. F. Lambert, "Propagation of sound in highly porous open-cell elastic foams," J. Acoust. Soc. Am. 73, 1131-1138 (1983).

17. P. C. Carman, Flow of Gases through Porous Media (Academic Press, New York, 1956).

18. D. T. Blackstock, "Propagation of plane sound waves of finite amplitude in nondissipative fluids," J. Acoust. Soc. Am. 34, 9-30 (1962).

19. D. T. Blackstock, "Thermoviscous attenuation of plane, periodic, finite-amplitude sound waves," J. Acoust. Soc. Am. 36, 534-542 (1964).

20. D. T. Blackstock, "Connection between the Fay and Fubini solutions for plane sound waves of finite amplitude," J. Acoust. Soc. Am. 39, 1019-1026 (1966).

21. A. L. Thuras, R. T. Jenkins, and H. T. O'Neil, "Extraneous frequencies generated in air carrying intense sound waves," J. Acoust. Soc. Am. 6, 173-183 (1935).

22. R. F. Lambert, "The acoustical structure of highly porous open-cell foams," J. Acoust. Soc. Am. 72, 879-887 (1982).

23. F. H. Fenlon, "A recursive procedure for computing the nonlinear spectral interactions of progressive finite-amplitude waves in dispersive fluids," J. Acoust. Soc. Am. 50, 1299-1312 (1971).

24. A. Korpel, "Frequency approach to nonlinear dispersive waves," J. Acoust. Soc. Am. 67, 1954-1958 (1980).

25. D. A. Webster and D. T. Blackstock, "Finite-amplitude saturation of plane sound waves in air," J. Acoust. Soc. Am. 62, 518-523 (1977).

26. T. L. Foreman, "Ray modeling methods for range dependent ocean environments," Applied Research Laboratories Report, ARL-TR-83-41, (Master's Thesis) (1983).

27. W. E. Zorunski and T. L. Parrot, "Nonlinear acoustic theory for thin porous sheets," NASA SP-189, 17-27 (1968).

28. U. J. Kurze and I. L. Ver, "Sound attenuation in ducts lined with non-isotropic material," J. Sound Vib. 24, (2) 177-187 (1972).

# REFERENCES

1. H. L. Kuntz, II, "High-intensity sound in air saturated fibrous bulk porous materials," Applied Research Laboratories Report, ARL-TR-82-54, NASA CR-167979, ADA 121450 (Ph. D. dissertation) (1982).

2. W. E. Zorumski and T. L. Parrot, "Nonlinear acoustic theory for rigid porous materials," NASA TN-6196 (1971).

3. Lord Rayleigh, J. W. S., Theory of Sound, Vol. II, 2nd ed. (The Macmillan Company, New York, 1945).

4. G. Kirchhoff, "Uber den Einfluss der Warmeleitung in einem Gase auf die Schall bewegung, "Annalen der Physik und Chemie (Poggendorff's Annalen), 134, 177-193 (1868) (Concerning the influence of heat conduction in a gas on sound propagation).

5. L. L. Beranek, "Acoustic impedance of porous materials," J. Acoust. Soc. Am. 13, 248-260 (1942).

6. L. L. Beranek, "Acoustical properties of homogeneous, isotropic rigid tiles and flexible blankets," J. Acoust. Soc. Am. 19, 556-568 (1947).

7. R. F. Lambert and J. S. Tesar, "Acoustic structure and propagation in highly porous, layered, fibrous materials," J. Acoust. Soc. Am. 76, 1231-1237 (1984).

8. R. A. Scott, "The propagation of sound between walls of porous material," 1946 Proceedings of the Physical Society, 58, 358-368.

9. R. A. Scott, "The absorption of sound in a homogeneous medium," 1946 Proceedings of the Physical Society, 58, 165-183.

10. E. Zwikker and C. W. Kosten, Sound Absorbing Materials (Elsevier Publishing Company, Inc., New York, 1949).

11. R. F. Lambert, "Acoustical properties of highly porous fibrous materials," NASA Technical Memorandum 80135, Langley Research Center (1977).

12. V. Kuhl and E. Meyer, "Untersuchungen uber die Winkel-und Frequenzabhangigkeit der Schallschluckung von porosen Stoffen," Akademie der Wissenachaptern, Berlin, Mathematisch-Naturwissen-Schaftliche Klasse, Sitzungsberichte der Physikalische-Mathematisch Klasse, 26, 416-435 (1932) (Investigation of the Angular- and Frequency-dependence of the Sound Absorption of Porous Materials).

13. A. S. Hersh and B. Walker, "Acoustic behavior of fibrous bulk materials," presented at the AIAA 5th Aeroacoustics Conference, Seattle, WA, Paper #79-0599 (1979).

```fortran
      IF(IPRINT.NE.111)GOTO 9998
      READ(4,1101)ISET
1101  FORMAT(I2)
      DO 1200 I=1,ISET
      READ(4,1102)NDP,NSYM
1102  FORMAT(2I2)
      DO 1201 IJ=1,NDP
      READ(4,1103)DATX(IJ),DATY(IJ)
1103  FORMAT(F5.2,F6.2)
1201  CONTINUE
      CALL PLTDATA(DATX,DATY,NDP,-1,NSYM,0.,DX,60.,DY,.08,3)
1200  CONTINUE
9998  CALL PLTEND
9999  STOP
      END
C
C
C     THE FOLLOWING IS A DUMMY SUBROUTINE FOR DGEAR
C
      SUBROUTINE FCN(N,X,Y,YPRIME)
      DIMENSION Y(64),YPRIME(64)
      INTEGER N
      CALL CFCN(N,Y,YPRIME)
      RETURN
      END
C
C
C     THIS ROUTINE CALCULATES THE VALUE OF VN-PRIME
C     FROM KNOWN VALUES OF VN.
C
C     IT IS CALLED BY DGEAR
C
      SUBROUTINE CFCN(N,V,VP)
      COMPLEX A,J,SUM(32),V(32),VP(32)
      COMMON A(32),J,IFFT,OMEGA,R2,VDC
      CALL RHS(V,SUM,N)
      N2=N/2
      DO 10 IN=1,N2
      VP(IN)=-IN*OMEGA*R2/2./A(IN)*SUM(IN)-J*A(IN)*V(IN)
10    CONTINUE
      RETURN
      END
C
C
```

168

```
C     THIS ROUTINE FINDS THE HARMONIC DISTORTION SPECTRUM
C     SUM( V(P)*W(N-P) ) FOR ALL N.
C
      SUBROUTINE RHS(V,SUM,N)
      COMPLEX A,V(32),J,SUM(32),W(0:63)
      COMMON A(32),J,IFFT,OMEGA,R2,VDC
      NMAX=2**IFFT
      NO=N/2
      N1=NO+1
      N2=NMAX-NO-1
      N3=N2+1
      N4=NMAX-1
      W(0)=VDC
      DO 601 IW=1,NO
 601  W(IW)=V(IW)
      DO 6015 IW=N1,N2
6015  W(IW)=CMPLX(0.,0.)
      DO 602 IW=N3,N4
 602  W(IW)=CONJG(V(NMAX-IW))
C
C     CAUTION: THESE COMPLEX FFT'S ARE ARL ROUTINES.  THESE MUST BE ATTACHED
C              FROM A LIBRARY.
C
      CALL FFTH(W,IFFT,1.)
      DO 603 IW=0,N4
 603  W(IW)=W(IW)*CABS(W(IW))
      CALL FFTG(W,IFFT,1.)
      DO 605 IW=1,NO
 605  SUM(IW)=W(IW)
      RETURN
      END
C
C     ANOTHER DUMMY ROUTINE
C
      SUBROUTINE FCNJ(N,X,Y,PD)
      INTEGER N
      REAL Y(N),PD(N,N),X
      RETURN
      END
```

167

```fortran
      AXLEN=8.5
      AYLEN=5.0
      DX=20./AXLEN
      DY=120./AYLEN
      DATA LABX/"DISTANCE"/,LABY/"AMPLITUDE"/
      GOTO 100
C
C     RIPCORD STATEMENT IF DGEAR IS IN TROUBLE
C
  500 PRINT*,IER,XEND,X,H,TOL
      GOTO 9999
C
C     BACK TO PLOTTING
C
  100 CONTINUE
      CALL PLTLFN(L"PLOT")
      CALL PLTDIM(11.0,8.5,1,4.0)
      CALL PLTORG(XORG,YORG)
      CALL PLTAXIS(0.0,0.0,AXLEN,0.0,0.0,20.,1.,LABX,-8,2,-.1,-.1)
      CALL PLTAXIS(0.0,0.0,AYLEN,90.0,60.,180.,10.,LABY,9,2,-.1,-.1)
      CALL PLTAXIS(0.,AYLEN,AXLEN,0.0,.20,.1,LABX,0.0,-.1,-.1)
      CALL PLTAXIS(AXLEN,0.,AYLEN,90.,60.,180.,10.,LABY,0,0,.1,.1)
      CALL PLTDATA(ZRAY,C1,IZNUM,0,0,0,DX,60.,DY,0,.2)
      CALL PLTDATA(ZRAY,C2,IZNUM,0,0,0,DX,60.,DY,0,.8)
      CALL PLTDATA(ZRAY,C3,IZNUM,0,0,0,DX,60.,DY,0,.9)
      CALL PLTDATA(ZRAY,C4,IZNUM,0,0,0,DX,60.,DY,0,.4)
      CALL PLTDATA(ZRAY,C5,IZNUM,0,0,0,DX,60.,DY,0,.5)
C
C     MEASURED DATA CAN BE OVERLAID ON THE PLOTTED CURVES FOR
C     COMPARISON WITH DATA  THE USER MUST PREPARE THE DATA FILE
C     "PROPDAT" ACCORDING TO THE FORMAT ABOVE.
C     NDP = NO. OF DATA POINTS
C     NSYM = SYMBOL FONT NO.
C     DATX = DISTANCE IN CENTIMETERS
C     DATY = LEVEL IN DB
C
      WRITE(5,1100)
 1100 FORMAT(20H PLOT DATA?, YES=111)
      READ*, IPRINT
```

166

```
        CALL RHS(V,SUM,N)

C
C       CALCULATION OF RELATIVE ERROR LEVELS
C          NOT IMPORTANT
C
C
        DO 800 IS=1,5
        IF(CABS(SUM(IS)).EQ.0.)GOTO 800
        IF(CABS(SNOLD(IS)).EQ.0.)GOTO 800
        SNOUT=CABS(.5+CLOG(SUM(IS)/SNOLD(IS))/2./J/A(IS)/DZ)
        ISN(IS)=INT(SNOUT*100.)
800     CONTINUE
        DO 850 IS=1,5
        SNOLD(IS)=SUM(IS)
850     CONTINUE

C
C       CALCULATION AND OUTPUT OF FIRST FIVE HARMONIC AMPLITUDES
C
C
860     DO 700 IN=1,5
        VOUT(IN)=A(IN)/IN*V(IN)-J*OMEGA*R2/2./A(IN)*SUM(IN)
        VOUT(IN)=VOUT(IN)/REF
        IF(CABS(VOUT(IN)).EQ.0.)VOUT(IN)=1.E-20
        C(IZ,IN)=CABS(VOUT(IN))
        C(IZ,IN)=20.*ALOG10(C(IZ,IN))+SPL1
        IF(C(IZ,IN).LT.60.)C(IZ,IN)=60.
700     CONTINUE

C
C
C       OUTPUT OF HARMONIC AMPLITUDES AND ERROR LEVELS
C
C
        XCM=XEND/KO*100
        WRITE(6,450)XCM,((C(IZ,IQ),IQ=1,5),(ISN(IT),IT=1,5)
450     FORMAT(1H ,F6.1,5(2X,F6.1),3X,5(1X,I3))

C
C       PLOTTING ROUTINES
C       THESE ARE ARL ROUTINES
C
C
        XORG=1.0
        YORG=2.0
```

165

```
         DO 214 IM=1,5
         VO(IM)=V(IM)
  214 CONTINUE
C
C
CCCCC OUTPUT OF NONDIMENSIONALIZED NORMALIZED IMPEDANCE CCCCCC
C
C
         DO 75 IN=1,6
         ISN(IN)=0
         SNOLD(IN)=SUM(IN)
         IF(CABS(V(IN)).EQ.0.)GOTO 75
         Z=CABS(-VPRIME(IN)/V(IN)/J/IN)/SQRT(1.4)
         WRITE(6,480)IN,Z
  480 FORMAT(3H Z(,I2,4H) = ,F9.6)
   75 CONTINUE
C
C
C     PREPARATION FOR DIFF EQ SOLUTION BY DGEAR SUBROUTINE
C
C     DGEAR IS AN IMSL ROUTINE AND MUST BE ATTACHED AS A LIBRARY
C
C
C
         METH=1
         MITER=0
         TOL=.00001
         H=.00001
         INDEX=1
         IER=0
         X=0.
         ZSTOP=ZMAX+DZ
C
CC
C     DGEAR TO THE RESCUE
C
C
         DO 100 XEND=0.,ZSTOP,DZ
         IZ=IFIX(XEND/DZ+.5)
         IF(XEND.EQ.0.)GOTO 860
         PRINT*,XEND,IZ
         CALL DGEAR(N,FCN,FCNJ,X,H,Y,XEND,TOL,METH,MITER,INDEX,IWK,WK,IER)
         PRINT*,XEND,X
         IF(IER.GT.128)GOTO 500
         IF(IER.NE.0)PRINT*,IER
```

164

```fortran
      XMAG=10**(SPL/20. )*1.38E-10
      XCOMP=CMPLX(COSD(PHASE)*XMAG,SIND(PHASE)*XMAG)
      IF(IN.EQ.0)GOTO 77
      VPRIME(IN)=-J*IN*XCOMP
      V(IN)=XCOMP*IN/A(IN)
   77 IF(IN.EQ.0)VDC=XMAG
      IF(IN.EQ.1)SPL1=SPL
      IF(IN.EQ.1)REF=XCOMP
      GOTO 10
   11 CONTINUE
      WRITE(5,425)
C
C     IF YOU WANT TO START ALL OVER AGAIN, SIMPLY TYPE 111 HERE
C     IF NOT, TYPE SOMETHING ELSE LIKE 1234 OR 1776 OR 1492 OR 2001
C
  425 FORMAT(37H IF THE COMPUTER SCREWED UP, TYPE 111)
      READ*,IESC
      IF(IESC.EQ.111)GOTO 1
C
C     PREPARATION FOR FFT
C
      XK=ALOG(FLOAT(N))/ALOG(2. )
      IFFT=INT(XK)+1
      IF(AMOD(XK,1. ).EQ.0. )IFFT=IFFT-1
C
CCCCCC ITERATION TO FIND VN FROM VPRIME
CCCCCC       MAY BE UNSTABLE FOR CUBIC NONLIN. MODEL
CCCCCC       IF INITIAL VALUES ARE LARGE
C
   61 ICOUNT=0
      DO 70 IN=1,6
      VNOLD(IN)=V(IN)
      CALL RHS(V,SUM,N)
      V(IN)=J/A(IN)*(IN*OMEGA*R2/2. /A(IN)*SUM(IN)+VPRIME(IN))
      IF(CABS(V(IN)).EQ.0.)GOTO 69
      IF(ABS((VNOLD(IN)-V(IN))/V(IN)).LT..01)GOTO 69
      GOTO 70
   69 ICOUNT=ICOUNT+1
   70 CONTINUE
      PRINT*,ICOUNT
      IF(ICOUNT.NE.6)GOTO 61
```

163

```
         R2=R2*38.3/OMEGA/FREQ

C
C   FOR CUBIC NONLINEARITY CASE, ADD LINE R2=R2*290.7
C
C
         DO 50 IJ=1,32
   50    A(IJ)=IJ*CSQRT(OMEGA*(1.-J*R1/IJ))
         WRITE(6,402)R1,R2,FREQ,OMEGA
  402    FORMAT(4H R1=,F10.3,3X,3HR2=,F10.2,3X,5HFREQ=,F8.2,
        *3X,10HPOROSITY =,F5.3)
         KO=FREQ/46.27
         ZMAX=.2*KO
         DZ=.005*KO
         IZNUM=IFIX(ZMAX/DZ+.5)+1
         PRINT*,IZNUM
         IZNAM=IZNUM-1
         DO 98 IZN=0,IZNAM
         ZRAY(IZN)=IZN*.5
   98    CONTINUE
         VDC=0.
         DO 51 IJ=1,32
         VPRIME(IJ)=CMPLX(0.,0.)
   51    V(IJ)=CMPLX(0.,0.)
   10    WRITE(5,423)
C
C   ENTER THE HARMONIC NUMBER.
C
  423    FORMAT(16H HARMONIC NUMBER)
         READ*,IN
         IF(IN.GT.32)GOTO 11
         WRITE(5,424)IN
  424    FORMAT(27H SPL AND PHASE OF HARMONIC ,I2)
C
C   ENTER THE SPL AND 'PHASE' OF THE HARMONIC
C   IF YOU DONT KNOW THE PHASE, JUST ENTER 0
C   ***YOU MUST ENTER SOME VALUE FOR THE SPL OF HARM. 1.
C   *** SUGGEST: 50 DB.  OTHERWISE THE PROGRAM WILL BOMB.
C
C
C   THE DATA ENTRY LOOP MAY BE ESCAPED BY TYPING A HARM. NO. .GT. 32
C
         READ*,SPL,PHASE
         WRITE(6,404)IN,SPL,PHASE
  404    FORMAT(12H HARMONIC #=,I2,3X,4HSPL=,F5.1,3X,8HPHASE = ,F5.1)
```

162

```fortran
      PROGRAM PRPKRV2(INPUT,OUTPUT,KRUD,PLOT,PROPDAT
     *,TAPE4=PROPDAT,TAPE5=OUTPUT,TAPE6=KRUD)
C
CCCCCCCCCCCCCCCCCCCCCCCCCCCCCCCC
C
C     PROGRAM PRPKRV CALCULATES THE HARMONIC AMPLITUDES OF A SIGNAL AS
C     A FUNCTION OF DISTANCE . THE FIRST FIVE HARMONICS
C     ARE PLOTTED.
C
CCCCCCCCCCCCCCCCCCCCCCCCCCCCCCCCCCC
C
C
      COMPLEX VOUT,J,A,REF,SUM(32),ERROR,XCOMP,SNOLD(6)
      COMPLEX VO(5),VNOLD(6),V(32),VPRIME(32)
      COMMON A(32),J,IFFT,OMEGA,R2,VDC
      DIMENSION Y(64),IWK(64),WK(1200),VOUT(5),C(0:201,5),ISN(6)
      DIMENSION ZRAY(0:200),C1(0:201),C2(0:201)
      DIMENSION C3(0:201),C4(0:201),C5(0:201),DATX(6),DATY(6)
      INTEGER LABX(1),LABY(1)
      EQUIVALENCE (V(1),Y(1))
      EQUIVALENCE (C1(0),C(0,1)),(C2(0),C(0,2)),(C3(0),C(0,3))
      EQUIVALENCE (C4(0),C(0,4)),(C5(0),C(0,5))
      EXTERNAL FCN,FCNJ
C
C     INITIALIZATION LOOP
C
C
C
      J=CMPLX(0.,1.)
C
C     ENTER NUMBER OF HARMONICS TO BE RETAINED IN SOLUTION
C
C
    1 WRITE(5,420)
  432 FORMAT(20H NUMBER OF HARMONICS IN SOLUTION)
      READ*,N
      WRITE(6,401)N
  401 FORMAT(6H NMAX=,I2)
      N=2*N
      WRITE(5,421)
C
C     ENTER RESIST. COEFFS R1,R2 IN MKS UNITS. FUND FREQ. POROSITY@
C
  421 FORMAT(20H R1,R2,FREQ,POROSITY)
      READ*,R1,R2,FREQ,OMEGA
      R1=R1/7.61/OMEGA/FREQ
```

impedances has been observed to be less stable in PRPKRV3 than in its predecessor and, as a result, the algorithm may never converge and the solution may never be executed. The limits of the algorithm stability are discussed briefly in Appendix B.

The computer code contains a running commentary on its function which will, it is hoped, help the user understand the operation of this program.

## Appendix C

## COMPUTER PROGRAM

Computer program PRPKRV2 is a FORTRAN 5 program which solves Eq. (3.29) as an initial value problem. A resistivity function of the form $r = r_1 + r_2 u \, sgn(u)$ is assumed. The heart of the program is the IMSL routine DGEAR, which solves systems of differential equations using a 12th order Adams predictor-corrector method, also known as Gear's method. The routine is adaptable to a wide variety of problems and is particularly designed to solve stiff equations with unstable solutions. Fast Fourier transform and plotting routines which were written at Applied Research Laboratories, The University of Texas at Austin, were used extensively in this program.

The calculation retains up to 32 harmonics and accepts inputs of SPL and phase for as many. The user must also supply the values of $r_1$ and $r_2$, the fundamental frequency, and the porosity $\Omega$. Hardcopy output is provided which gives the dimensionless coefficients $R_1$ and $R_2$, the initial dimensionless impedance magnitudes for the first six harmonics, and the predicted SPL of the first five harmonics out to 20 cm beyond the effective origin in $\frac{1}{2}$ cm steps. A plot of the SPL predictions is also supplied, and the user has the option of overlaying measured data for comparison with predictions.

The program PRPKRV3, which uses the resistivity relation $r = r_1 + r_3 u^2$, differs from PRPKRV2 in only two places. These are marked in the code and the replacement lines are provided. The iterative approximation for the initial

Copy No.

Department of Physics and Astronomy
University of Mississippi
University, MS 38677
60     Attn:  Henry E. Bass

Department of Physics and Chemistry
Naval Postgraduate School
Monterey, CA 93940
61 - 62    Attn:  S. L. Garrett
          S. W. Yoon

Electrical Engineering Department
University of Minnesota
Minneapolis, MN 5455
63 - 64    Attn:  R. F.Lambert
          J. S. Tesar

School of Mechanical Engineering
Georgia Institute of Technology
Atlanta, GA 30332
65 - 67    Attn:  A. D.Pierce
          P. H. Rogers
          J. H. Ginsberg

Department of Physics
Kalamazoo College
Kalamazoo, MI 49007
68     Attn:  W. M. Wright

Manufacturing Systems Engineering Bldg.
University of Nevada
Reno, NV 89557
69     Attn:  N. D. Perreira

Department of Physics
University of Tennessee
Knoxville, TN 37916
70 - 71    Attn:  M. A. Breazeale
          G. Du

Department of Mechanical Engineering
Massachusetts Institute of Technology
Cambridge, MA 02139
72     Attn:  Mark A. Theobald

Department of Physics
Massachusetts Institute of Technology
Cambridge, MA 02139
73     Attn:  K. U. Ingard

101 Engineering A Bldg.
Pennsylvania State University
University Park, PA 16802
74     Attn:  J. Tichy

Physics Department
University of California
Los Angeles, CA 90024
75     Attn:  Isodore Rudnick

Yale University
P. O. Box 2159
New Haven, CT 06520
76     Attn:  R. E. Apfel

Aerospace Engineering Department
Texas A&M University
College Station, TX 77843
77     Attn:  Kenneth Corkan

Mathematics Institute
University of Bergen
Allegaten 53-55
N-5000 Bergen
NORWAY
78 - 79    Attn:  S. Tjøtta
          J. Naze Tjøtta

Department of Applied Math Studies
University of Leeds
Leeds L82 9JT
ENGLAND
80     Attn:  David G. Crighton

Copy No.

Department of Electrical Engineering
Nagoya University
Furo-Cho, Chikusa-Ku
Nagoya, 464
JAPAN
81     Attn:  T. Kamakura

Institute of Sound Vibration Research
The University
Southampton S09 5NH
ENGLAND
82 - 83    Attn:  C. L. Morfey
          P. E. Doak

School of Physics
University of Bath
Claverton Down
Bath BA2 7AY
ENGLAND
84     Attn:  H. O. Berktay

Industrial Acoustics Research Group
Technical University of Denmark
Building 352
DK-2800 Lyngby
DENMARK
85     Attn:  L. Bjørnø

The Institute of Scientific
  & Industrial Research
Osaka University
8-1 Mihogaoka, Ibaraki
Osaka
JAPAN 567
86     Attn:  Dr. Akira Nakamura

Instituto de Acustica
Centro de Fisica Aplicada
"Leonardo Torres Quevado"
Serrano, 144-Madrid-6
SPAIN
87     Attn:  J. A. Gallego-Juarez

Department of Electrical Engineering
The University of Texas at Austin
Austin, TX 78712
88     Attn:  E. L. Hixson

Department of Mechanical Engineering
The University of Texas at Austin
Austin, TX 78712
89     Attn:  J. R. Howell

Dept. of Aerosp. Engrg. and Engrg. Mech.
The University of Texas at Austin
Austin, TX 78712
90 - 91    Attn:  A. Bedford
          C. H. Yew

92 - 97    ARL:UT Groups

98     David T. Blackstock, ARL:UT

99     Yves Berthelot, ARL:UT

100    Ilene Busch-Vishniac, ARL:UT

101    F. D. Cotaras, ARL:UT

102    James M. Estes, ARL:UT

103    Mark F. Hamilton, ARL:UT

104    J. A. Hawkins, ARL:UT

105    T. G. Muir, ARL:UT

106    David A. Nelson, ARL:UT

107    James A. TenCate, ARL:UT

108    Library, ARL:UT

109 - 119  Reserve, ARL:UT

# END

# FILMED

8-85

# DTIC